Thèse

Université de Lille

Ecole doctorale Sciences de la Matière, du Rayonnement et de l'Environnement

Présentée par

Riccardo REALI

Pour obtenir le grade de

Docteur de l'Université

Spécialité: Physique et Sciences des Matériaux

Modeling creep of lower mantle minerals: bridgmanite and (Mg,Fe)O

Modélisation du fluage des minéraux du manteau inférieur: bridgmanite et (Mg,Fe)O

Thèse dirigée par Patrick Cordier et Philippe Carrez

Soutenue l'11 septembre 2018, devant le jury composé de

Dr. Luce Fleitout	École Normale Supérieure	Président
Prof. Hans–Peter Bunge	Ludwig–Maximilians–Universität München	Rapporteur
Dr. Olivier Castelnau	Arts et Métiers ParisTech	Rapporteur
Dr. Alexandre Dimanov	École Polytechnique	Examinateur
Dr. Laurent Dupuy	C.E.A. Saclay	Examinateur
Prof. Philippe Carrez	Université de Lille	Directeur de thése
Prof. Patrick Cordier	Université de Lille	Directeur de thése

PhD Thesis

Université de Lille

Ecole doctorale Sciences de la Matière, du Rayonnement et de l'Environnement

Presented by

Riccardo REALI

To obtain the degree of

Docteur de l'Université

in Physics and Materials Sciences

Modeling creep of lower mantle minerals: bridgmanite and (Mg,Fe)O

Thesis supervised by Patrick Cordier and Philippe Carrez

Scientific committee

Dr. Luce FLEITOUT	École Normale Supérieure	President
Prof. Hans–Peter BUNGE	Ludwig–Maximilians–Universität München	Reviewer
Dr. Olivier CASTELNAU	Arts et Métiers ParisTech	Reviewer
Dr. Alexandre DIMANOV	École Polytechnique	Examiner
Dr. Laurent DUPUY	C.E.A. Saclay	Examiner
Prof. Philippe CARREZ	Université de Lille	Supervisor
Prof. Patrick CORDIER	Université de Lille	Supervisor

Resumé

Cette thèse porte sur la déformation de deux phases minérales majeures du manteau inférieur de la Terre: la bridgmanite et (Mg,Fe)O. Ils représentent près de 90% du manteau inférieur, et leur rhéologie est de première importance en vue de mieux comprendre la convection mantellique.

La rhéologie de ces phases a été modélisée grâce à l'utilisation de techniques de calcul numériques et analytiques afin de déterminer leur réponse en fluage (c'est–à–dire l'écoulement stationnaire sous une charge constante).

Les agents pertinents de la déformation en fluage sont identifiés et leur comportement est modélisé à l'échelle du cristal. Les dislocations étant les porteurs principaux de la déformation plastique, le fluage a donc été modélisé comme résultant du glissement et/ou de la montée (contrôlée par la diffusion) des dislocations.

Le fluage de (Mg,Fe)O résulte d'une combinaison de glissement et de montée des dislocations. Afin de modéliser ce comportement à l'échelle mésoscopique, une technique de dynamique des dislocations 2.5D a été employée. Dans (Mg,Fe)O, le glissement des dislocations est responsable de la déformation plastique, mais la vitesse de fluage est contrôlée par la montée. Nos calculs de vitesses de fluage permettent d'estimer la viscosité de (Mg,Fe)O dans les conditions des couches profondes du manteau inférieur.

Pour la bridgmanite, nous proposons un fluage impliquant la montée pure des dislocations dont la vitesse de fluage est calculée sur la base d'un modèle analytique de la littérature. Nous en déduisons la vitesse de fluage de la bridgmanite le long d'un géotherme, valeurs que l'on peut comparer aux observables disponibles actuellement.

Abstract

This thesis work addresses the deformation behavior of two major mineral phases of the Earth's lower mantle: bridgmanite and (Mg,Fe)O. They constitute ~90% of the lower mantle and their rheology is of primary importance for a better understanding of mantle convection.

The rheological properties of these phases were modeled through the implementation of numerical and analytical techniques, in order to assess their creep behavior (*i.e.* steady–state deformation under a constant applied stress).

The relevant deformation agents driving creep are identified and then modeled at the single crystal scale. In this framework, dislocations are amongst the main carriers of crystal plasticity and the creep behavior of the considered minerals can therefore be assessed by considering dislocation glide and diffusion–driven dislocation climb.

(Mg,Fe)O creep is driven by the interplay between glide and climb and in order to model it, a 2.5–dimensional (2.5D) dislocation dynamics (DD) approach has been deployed. 2.5D–DD is a numerical technique which addresses the collective behavior of dislocations at the mesoscale. It is demonstrated that dislocation glide is responsible for the plastic deformation and climb is the rate–limiting mechanism. From the modeled creep strain rates it was possible to estimate viscosity of (Mg,Fe)O at lowermost mantle conditions.

As for bridgmanite a pure climb mechanism is proposed, and the creep strain rates were evaluated according to a physics–based analytical creep model. The viscosity of bridgmanite along a geotherm is retrieved and compared with the available observables.

Long as I remember
the rain's been coming down.
Clouds of mistery pouring
confusion on the ground.
Good men through the ages
trying to find the sun.
And I wonder,
still I wonder
who'll stop the rain.

Creedence Clearwater Revival

Acknowledgements

Firstly, I am thankful to Patrick Cordier, who designed this project and assigned it to me. Other than an incredibly brilliant guide accompanying me along this path, he has always been a constant source of honest, truthful and creative insight into any treated subject. For the immense trust he placed in me and for the joyful working atmosphere he created, I will always be grateful. He is also to be credited for establishing the contacs which became international collaborations with colleagues from other institutions.

Of these coworkers, Jennifer Jackson was the first to enter the project and her contribution meant a lot under many aspects. She found ways to build solid implications out of my work and transmitted her knowledge and enthusiasm also outside the laboratory. The continuous care she gave to our work in her visits in Lille as well as at conferences was simply incredible. Also Jim Van Orman and Jeff Pigott visited our lab and I much enjoyed the discussions we carried along, receiving countless suggestions and explanations of extraordinary competence and insight. Finally, Dan Bower contributed for more implications and I thank him for his work and for being always available for any clarification.

My deepest gratitude goes to my co–supervisor Philippe Carrez, for the constant help he gave while tackling every technical setback and for accompanying me through the formation in a field which, at the beginning, was out of my expertise. For having taught me a lot of things with extraordinary availability I am very thankful to Francesca Boioli. I also benefited of the exchange with the other members of the Rheoman Team and for this I am thankful to Karine Gouriet, Pierre Hirel, Antoine Kraych, Sebastian Ritterbex, Alexandre Mussi and Billy Nzogang. For sharing lots of free time a special thanks is for Alexandra Goryaeva and Srinivasan Mahendran.

Thank you to François, which shared my experience in Lille and introduced me to many friends (so many friends), to Eric and Clara for all the time spent together and to Ehsan.

To my friends of a lifetime, for having always made me feel like I had never left. To CS for being always there, at my side. The B side.

To my family, to which this work is dedicated.

Contents

A note for the reader

The present thesis work was carried on through several cooperations with colleagues from other institutions.
They are gratefully acknowldged for the significant contribution and improvement that they brought to this project with their diverse expertise, ideas and perspective.
Along this manuscript, the reader can distinguish a few footnotes denoting the sections containing major contributions from these coauthors.

Dr. **Daniel J. Bower**, Center for Space and Habitability, University of Bern, Switzerland.

Dr. **Benoit Devincre**, Laboratoire d'Etude des Microstructures (LEM), CNRS-ONERA UMR 104, Chatillon Cedex, France.

Prof. **Jennifer M. Jackson**, Seismological Laboratory, Division of Geological and Planetary Sciences, California Institute of Technology, Pasadena, California, U.S.A.

Dr. **Jeffrey S. Pigott**, Shock and Detonation Physics, Los Alamos National Laboratory, Los Alamos, New Mexico, U.S.A.

Prof. **James Van Orman**, Department of Earth, Environmental, and Planetary Sciences, Case Western Reserve University, Cleveland, Ohio, U.S.A.

Chapter 1

Introduction

The terrestrial lower mantle represents one of the most inaccessible and unresolved compartment of the Earth's interior, due to the difficulties of directly sampling its main constituents and constraining their deformation behavior.

Here, the main observables from seismic data and high pressure experiments are outlined in order to provide a coherent picture of the lower mantle, comprising its main structure, the seismic discontinuities characterizing its boundaries, the main mineral assemblages and heterogeneities.

During mantle convection, the lower mantle mineral aggregates deform continuously in order to transport the Earth's internal heat to the surface. This convective motion taking place at geological timescales results from the viscous behavior of the aggregates, which flow under extremely small strain rates in response to the deviatoric stresses typical of the lower mantle. A macroscopic parameter describing this deformation behavior is viscosity. Information about viscosity can be retrieved from surface observables like geoid anomalies or isostatic rebound data. Significant variability of this parameter is highlighted from a compilation of different sources from the literature. However, the historical value of 10^{21} Pa·s proposed by Haskell (1935) remains a good estimate.

Another approach that can be adopted to constrain the viscosity of the lower mantle is represented by the attempt of modeling the creep behavior of its minerals and aggregates. In fact, the large scale flow identified by viscosity is nothing but the result of creep deformation at the mesoscopic scale.

Therefore, the defects responsible for the intracrystalline plasticity of minerals are presented, along with a detailed description of the main phenomenological and analytical models so far employed to describe creep. Finally, the minerals addressed in this study are introduced.

Keywords: lower mantle; viscosity; crystal defects; creep; (Mg,Fe)O; bridgmanite.

1.1 The lower mantle

1.1.1 The Earth's interior: generalities

The knowledge on the structure and composition of the Earth's deep interiors mostly derives from analysis of seismic waves, which are generated during earthquakes. When an earthquake occurs, seismic body waves (most notably, P or primary waves and S or secondary/shear waves) are produced and spread out in all directions through the Earth's interior. Seismic stations located at increasing distances from the earthquake epicenter record seismic waves that have traveled through different paths in the Earth. Seismic wave velocities depend on the properties of the materials they pass through, such as composition, different mineral phases (characterized by their elastic properties and density), temperature and pressure. They travel at higher velocities through denser materials and therefore generally travel faster with depth (*i.e.*, with increasing pressure and, with it, density). Anomalously hot areas correspond to slower seismic waves, whereas they travel faster in colder regions. Consequently, seismic velocity anomalies are often interpreted as resulting from temperature anomalies in seismic tomography. Also, molten areas within the Earth slow down P waves and stop S waves because their shearing motion cannot be transmitted through a liquid. Partially molten areas may slow down the P waves and attenuate or weaken S waves.

When seismic waves cross layers with contrasting properties – that is, when they pass through media with distinctly differing seismic velocities V_P and V_S – reflections, refraction (bending), and production of new wave phases (*e.g.*, an S wave produced from a P wave) often take place. Sudden jumps in seismic velocities across a boundary are known as seismic discontinuities. The first geophysical observable bearing this information consists on the travel time of seismic waves. The interpretation of a wide set of seismic data collections revealed the layered structure of the Earth's interior. In particular, within the Earth's mantle, these discontinuities (sketched in Figure 1.1) are associated with major mineralogical phase transformations. To a first approximation, the main compartments of the planet interiors are a silicate–rich mantle which extends to a depth of ~2900 km, and an iron rich metallic core with a radius of ~3400 km.

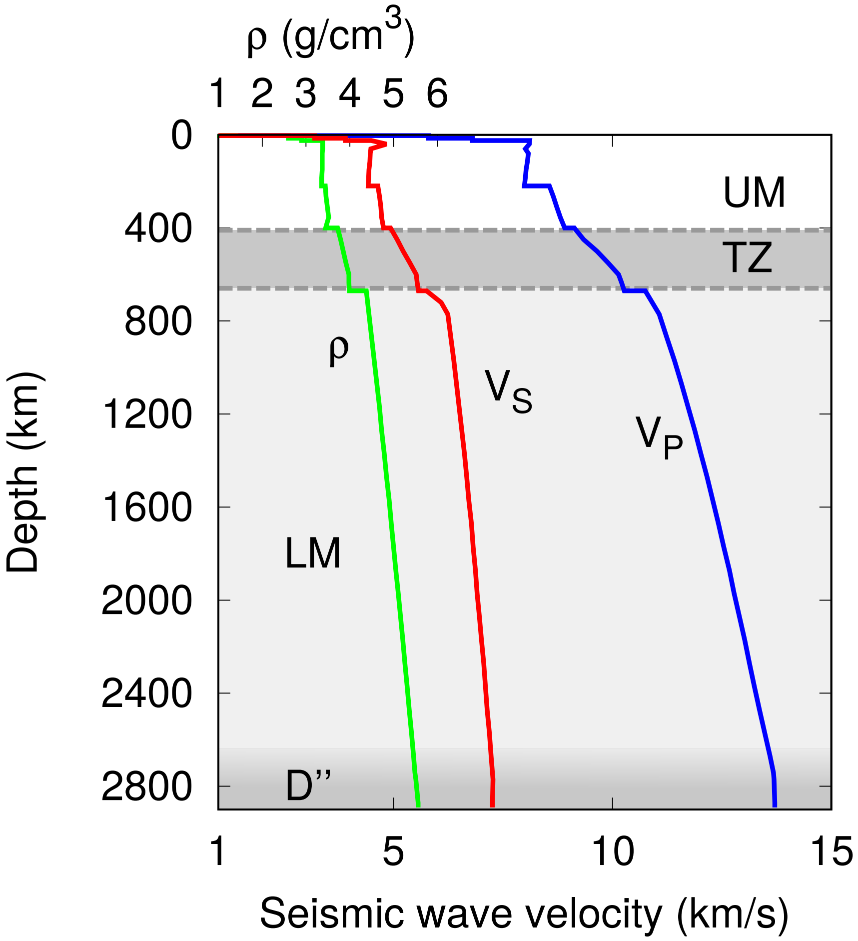

Figure 1.1: *sketch of the Earth's mantle. The seismic wave velocities (V_P and V_S) and the density profile (ρ) correspond to the PREM model by Dziewonski and Anderson (1981). Major seismic discontinuities mark the boundaries of the upper mantle (UM), transition zone (TZ) and lower mantle (LM). Modified from Cobden et al. (2015).*

The main subdivisions of the Earth's mantle are marked by significant seismic discontinuities. They separate the Earth's interiors in a transition zone (TZ) between the upper (UM) and the lower mantle (LM), together with a heterogeneous D'' layer at the interface between the mantle and the iron–rich metallic core. The latter is divided into a liquid outer core (characterized by absence of shear waves) and a solid inner core. Each of these layers is bounded by significant seismic discontinuities.

Seismic waves' velocities are also characterized by a dependence on direction or upon angle with respect to the medium they travel across. This phenomenon is known as seismic anisotropy and is closely tied to the shear wave splitting. In fact, when entering an anisotropic medium, shear waves split into two or more phase waves which propagate with different polarizations and velocities. Seismic anisotropy in the Earth's mantle may manifest in those domains characterized by lattice preferred orientation (LPO) of elastically anisotropic minerals. For this reason, seismic anisotropy is likely to provide indications on active deformation mechanisms.

It is also evident that the Earth's mantle is not homogeneous with depth. The upper mantle, that extends to a depth of about 410 km, mostly consists of olivine (60%), pyroxenes and garnets. A 410 km discontinuity is associated with transformation of olivine to wadsleyite, and the 660 km discontinuity is associated with transformation of ringwoodite to bridgmanite (*cf.* Figure 1.2). These major transformations are accompanied by pyroxene to garnet and garnet to perovskite phase transitions, which occur over broad depth intervals and modify the depth and sharpness of the discontinuities at 410 and 660 km. The lower mantle, on the other hand, extends between 660 km and 2900 km and is mostly made up of bridgmanite, ferropericlase and calcium perovskite (see the diagram on Figure 1.2). Representing more than 50% of Earth by volume, the lower mantle has a role of paramount importance in the thermochemical evolution of the Earth. The physical conditions in this region of the Earth are extreme: pressure ranges from 25 to 135 GPa, while temperature rises from 1600 up to almost 4000 K.

Besides these two major regions, there are two highly anisotropic boundary layers of ~200 km thickness each: the transition zone which separates the upper and the lower mantle, and the D'' layer, which is located right above the core–mantle boundary (CMB). This region of anomalous seismic gradients was first noted by Gutenberg (1914) and referred to as the D'' layer by Bullen (1950). Sharp seismic discontinuities in the transition zone are known to be associated with subsequent phase transitions of olivine into wadsleyite at ~410 km depth and ringwoodite at ~520 km depth, while the nature of the deep D'' layer, lying almost halfway to the Earth's center, is still a matter of ongoing debates. In fact, being located at the interface between the outer core and the lowermost mantle, where liquid iron alloy meets solid silicates, the D'' region represents one of the most complex boundary layers of the Earth. Here, for instance, the density contrast exceeds the one between the crust and the atmosphere.

The exact chemical composition and relative abundances of the minerals composing the Earth's mantle are impossible to be directly determined, therefore several models exist. A widely used model is the pyrolyte composition (Ringwood, 1966; 1975), which reproduces fairly well the main seismic features of the upper mantle and the transition zone. The volume fractions of the mantle phases along a geotherm (Brown and Shankland, 1981) according to this model are shown in Figure 1.2.

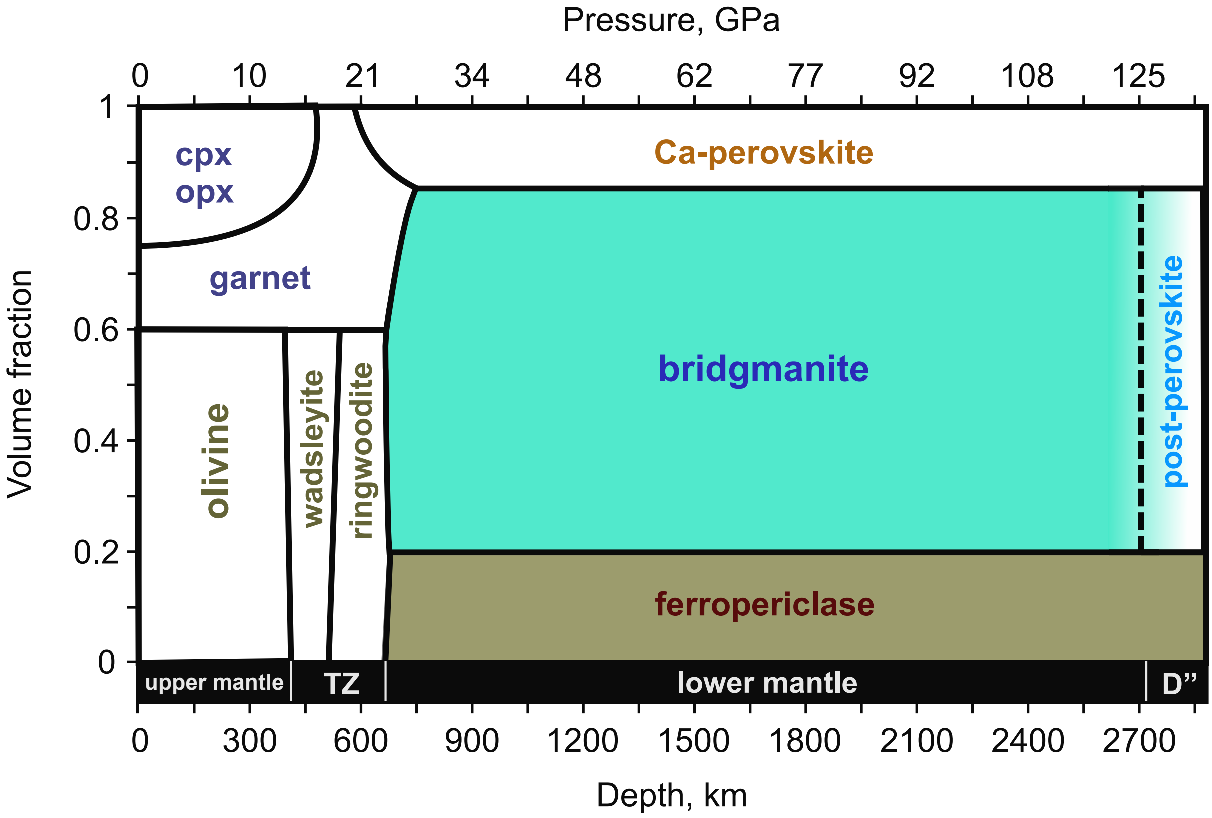

Figure 1.2: *mineralogy of the pyrolytic mantle as a function of depth, based on the geotherm by Brown and Shankland (1981). The colored sectors represent the minerals addressed in this study.*

The lower mantle's composition is generally modelled by comparing seismic observations with mineral physics data of possible lower mantle phases. Considering these evidences, the general consensus is that the lower mantle is composed of about 70% (Mg,Fe,Al)(Si,Fe,Al)O_3 bridgmanite, 20% (Mg,Fe)O ferropericlase and 10% $CaSiO_3$ perovskite.

In this thesis work, I will focus on the rheological behavior of the two main constituents of the lower mantle (*i.e.*, bridgmanite and ferropericlase) by modeling their deformation properties at varying temperatures and pressures, with a particular attention to the CMB region. Here, an iron–enriched (Mg,Fe)O phase (*i.e.*, magnesiowüstite) will also be considered.

1.1.2 Structure of the lower mantle

The bulk of the lower mantle does not show any significant evidence of major discontinuities or seismic anisotropy, although it represents a key compartment, underlying many processes observed at the Earth surface (*e.g.*, plate tectonics, earthquakes, hot spots, subducting slabs *etc.*). In fact, it mediates the heat transfer to the surface via a convective motion, characterized by the sinking of cold material coupled with the upwelling of the hotter one. The overall seismic homogeneity can be explained by the absence of abrupt changes of physical properties, which could result from sharp phase transitions or large chemical heterogeneities. Also, lower mantle minerals present strongly anisotropic elasticity characteristics. The seismic homogeneity, therefore, shall also indicate the absence of any texture, such as lattice preferred orientation (LPO).

On the other hand, there is a body of seismological observations (*e.g.* Thomas *et al.*, 2004; Lay, 2008; Hutko *et al.*, 2009; Long, 2009; Cobden and Thomas, 2013) that indicates a much more complex and heterogeneous landscape within the D'' region. Here, global, heterogeneous structures are detected, representing the domains of major heat exchange between the core and the convecting mantle. These zones are characterized by shear wave velocity anomalies of –2 to –5% and, due to this feature, are defined as large low shear–wave velocity provinces (LLSVPs). These domains cover around the 20% of the CMB, and are accepted to be thermal anomalies. Consequently, they are ascribed as the main source of mantle plumes (see Davies *et al.*, 2015; for a review). Hot plumes find evidence at the surface through hot–spot volcanism, and the location of LLSVPs is strongly correlated with location of the hot spots, confirming the connection between these phenomena.

Another kind of low velocity anomaly at the bottom of the mantle consists in restricted domains where a significant drop of V_P and V_S velocities by ~10% is observed (Garnero and Helmberger, 1995). For this reason these anomalies are commonly referred to as ultralow–velocity zones (ULVZ). In contrast to LLSVPs, ULVZs form compact, local structures having a few tens of km in height and a few hundreds of km of width at the base. These zones are generally observed at the edges of LLSVPs (Figure 1.3), where the vigorous stirring of the hot material at the base of LLSVPs is less powerful.

Other local anomalies, this time associated with lower temperatures, may be represented by the accumulation of the down–welling slabs, given their impossibility to pass through the major density contrast characterizing the CMB. The seismic evidence associated to these anomalies is an abrupt vertical change in speed of both P and S waves at the top of D'' region. A mapping of this feature clearly demonstrates that these slab pile–ups form some kind of lenses locally disposed in the colder regions elsewhere of LLSVPs. Within these colder domains, the post–perovskite phase (ppv) is expected to be stable at the expenses of bridgmanite.

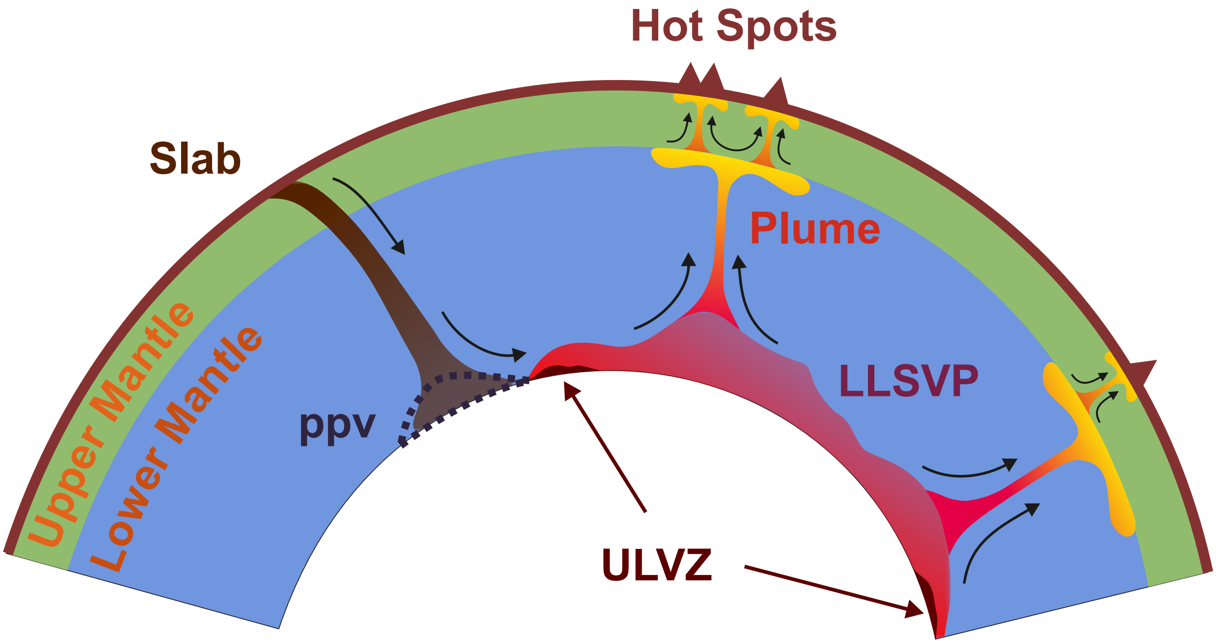

Figure 1.3: *schematic and simplified view of the different large scale structures characterizing the lower mantle. Their role in active convection is outlined by the black arrows. Mantle plumes may originate at the top of LLSVPs (large low shear–wave velocity provinces) and entrain some fractions of the matter from the deep interior towards the surface. ULVZ stands for the ultralow–velocity zones. The ppv zone corresponds to the lenses of post–perovskite, thought to be stable in relatively cold regions associated to the piling up of the subducted slabs. Modified from Deschamps et al. (2015) and after Goryaeva (2016).*

At the other, upper end of the lower mantle, at the interface with the transition zone, a first barrier for the subducting slabs takes place. At this interface, in fact, the different rheological properties of the slab couple with the density contrast of the ambient mantle phase assemblages. These are associated with the disproportionation reaction which decomposes ringwoodite and majorite garnet in ferropericlase and bridgmanite. These contrasts control whether slabs can penetrate into the lower mantle (and reach the CMB) or stagnate on top of the lower mantle. This directly affects the velocity of the plates attached to the slabs and determines the entity of chemical mixing between the upper and the lower mantle. Also, here, upwelling plumes can be truncated and diversify.

1.1.3 Rheological characteristics – convection, viscosity, creep

Although being solid, the mantle undergoes slow convection due to the temperature and density gradient between its different regions. Mantle convection is one of the most important features for the dynamics of the Earth since it drives most large–scale geological processes at the surface of our planet. It is however extremely difficult to study mantle convection since it occurs on timescales much longer than the human timescale. In principle, the Earth's interior consists of solid rocks that undergo convective motions through geological timescales and, in this framework, behave as viscous fluids. Therefore, a first approximation to describe this behavior consists in the attempt of characterizing a single parameter: viscosity. At high temperatures, in fact, many materials flow viscously, hence viscous behavior is extremely important.

Viscosity measures the resistance to flow of a fluid. Consequently, the vigour of convection taking place in the mantle is controlled by the viscosity of the different mineral aggregates composing its layered structure (Figures 1.1 and 1.2). This, in turn, strongly relates viscosity of the mantle with the mode of transport of the internal heat from the core towards the surface. Other than that, viscosity contrasts underlie many other relevant dynamic features of planet Earth, such as the formation and stability of mantle plumes, the opposite, downward, sinking motion of the subducted slabs and the physical coupling between the core and the mantle (with the related CMB topology). A better understanding of this parameter is hence of primary importance for a better constraining of the relevant mantle dynamics which, in turn, control the phenomena taking place at the Earth's surface.

From the observational point of view the first constraint on the rheology of the mantle has been placed by Haskell (1935) who, from the analysis of post–glacial uplift, proposed the viscosity of the upper mantle to be of the order of $10^{21} - 10^{22}$ Pa·s. This estimation has been proved to be very robust over the years, especially for the upper mantle. However, further studies based on modeling of convection (Bunge *et al.*, 1996), geoid (Hager and Richards, 1989; King, 1995; Bunge and Richards, 1996), plate velocity (Ricard *et al.*, 1993; Butterworth *et al.*, 2014), true polar wander (Phillips *et al.*, 2009) and length of day variations (Sabadini and Yuen, 1989) have consistently pointed out a significant increase of viscosity (originally placed at the 660 km discontinuity) in the range of 10–100 times between the transition zone and the lower mantle. Furthermore, most proposed profiles display a more or less broad viscosity hill in the middle of the mantle, at a depth roughly between 1200 km and 2000 km (Ricard and Wuming, 1991; Mitrovica and Forte, 2004; Morra *et al.*, 2010). Some recent studies, however, rather suggest a rheology contrast located around 1000 km depth (Ballmer *et al.*, 2017; Rudolph *et al.*, 2015). A compilation of viscosity values from different models is provided in Figure 1.4

Displaying these data from the literature, it appears evident that the viscosity values obtained from different models vary within several orders of magnitude. Despite this fact, an overall shared trend is identified, with a recognizable stiff domain in the uppermost mantle followed by an interval of weaker viscosity around the depth interval of the transition zone. Afterwards, viscosity rises again through the lower mantle, with several models peaking around its second half, before decreasing again in proximity of the core–mantle boundary.

1.1.4 Motivations

At the mesoscopic scale, the aforementioned viscous, convective motion of mantle's mineral aggregates takes place through creep. Creep is the tendency of a solid material to deform permanently – and eventually, flow – under the influence of a constant applied mechanical stress. In the case of a viscous fluid, an applied shear stress causes the flow of the fluid at a given rate. Stresses in the mantle are dependent on density, gravity, thermal

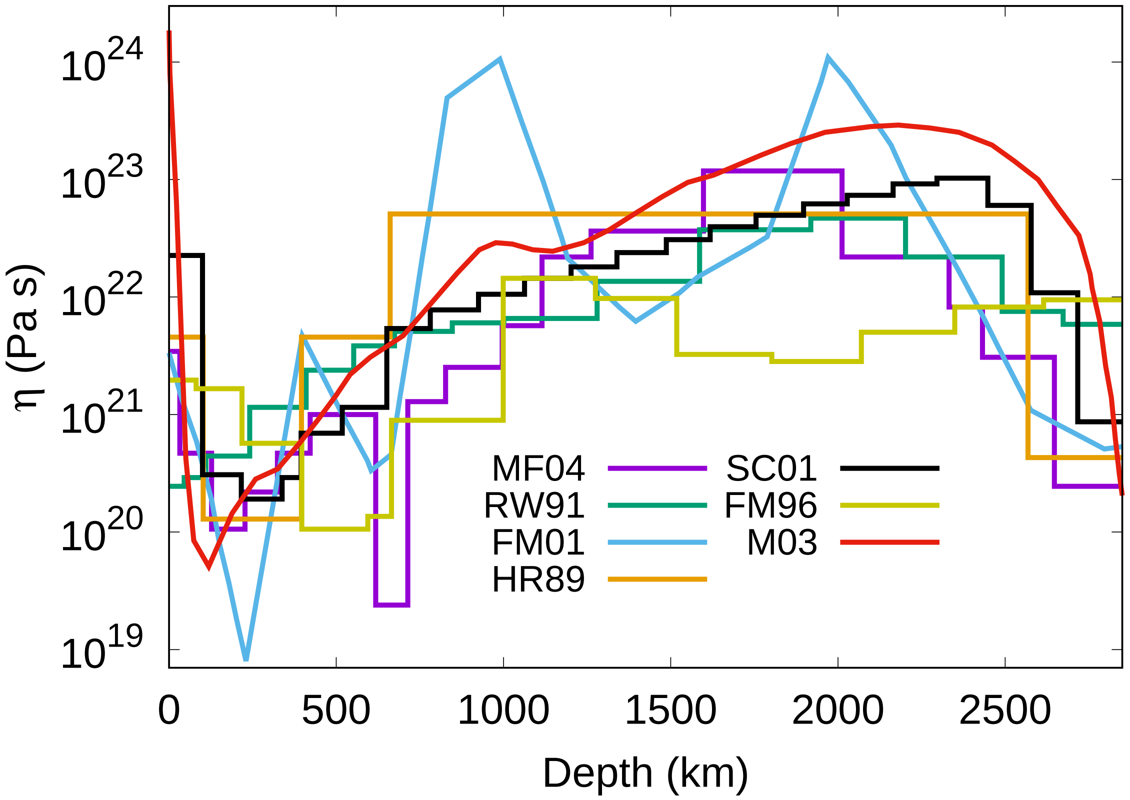

Figure 1.4: compilation of viscosity as a function of depth data obtained from different models. HR89: Hager and Richards (1989); RW91: Ricard and Wuming (1991); FM96: Forte and Mitrovica (1996); FM01: Forte and Mitrovica (2001); SC01: Steinberger and Calderwood (2001); M03: McNamara et al. (2003); MF04: Mitrovica and Forte (2004). Modified after Lawrence and Wysession (2006).

expansion coefficients and temperature heterogeneities (underlying convection). All these factors provide stresses available for creep deformation in the order of a few tens of MPa (Kaula, 1963; McKenzie, 1966). Being thermally activated, creep at a given pressure will occur as a function of the local temperature and of the deviatoric stress. The resulting creep rate, quantifying the vigor of the plastic flow, will be of the form $\dot{\varepsilon} = f(T, P, \sigma_{app})$. Knowing the rate of the flow and the entity of the deviatoric stress allows for the retrieval of viscosity.

Following this line of reasoning, in this thesis work I will identify the viable creep mechanisms driving deformation of lower mantle minerals. Then, I will evaluate the creep rates at high temperatures and pressures by employing both numerical and analytical models. In particular, here the focus will be on the contribution of dislocations to intracrystalline plasticity. The main goal consists in reproducing the lower mantle creep properties, which will result from the interplay between dislocation glide and climb mobilities, the latter being mediated by point defect diffusion. The obtained data allow the estimate of viscosity of lower mantle minerals, together with a comparison with existing models. An attempt to unify the laws obtained for single phases will also be presented, in order to give a rough estimate of the viscosities of different lower mantle aggregates.

In the next paragraph, therefore, it is presented a description of the main defects characterizing crystals, along with a first order definition of their mobilities. Afterwards, the principal models and laws describing the creep behavior of minerals are presented. Finally, the mineral phases addressed in this study are introduced.

1.2 Intracrystalline defects and relative mobilities

The perfect crystal is, in most cases, a theoretical concept which provides a good description for the variety of ordered atomic arrangements in solids. This structural description of a material is able to account for some intrinsic physical properties such as elasticity. However, plastic flow or brittle failure cannot be accurately described from the properties of perfect crystals and it is necessary to introduce the notion of defect. Furthermore, plastic flow is a transport phenomenon which results from the motion of defects in response to stress. Hence, the mobility of defects is of primary importance for modeling plastic deformation.

1.2.1 Point defects

The simplest defect is found at the atomic scale in the form of a vacant lattice site. Here the atom expected to be in its lattice position is missing: this defect is called a vacancy (Figure 1.5a). Vacancies, in fact, are intrinsically present in crystals, as they are created just by a matter of thermal activation. At each temperature above 0 K there is a thermodynamically stable vacancy concentration which minimizes the crystal's free energy. This intrinsic, equilibrium vacancy concentration c_0 reads:

$$c_0 = \exp\left(-\frac{\Delta G_f}{k_B T}\right) \tag{1.1}$$

where ΔG_f is the vacancy formation energy, T is temperature and k_B the Boltzmann constant.

An atom could also occupy a site which is not normally occupied (Figure 1.5b): this is an interstitial atom. The interstitial sites between atoms generally have volumes of less than one atomic volume, and the interstitial atoms therefore tend to produce large distortions among the surrounding atoms. For this reason, generally, interstitials have a formation energy several times higher than the one of vacancies and consequently tend to have a much lower equilibrium concentration in the bulk.

This simple sketch is sufficient to describe defects in monoatomic metals. Minerals are usually solids with an ionic character and are constituted of charged species: anions and cations. In this case, a point defect (vacancy or interstitial) cannot exist alone since it would unbalance charges. Because of these coupling effects needed to maintain charge equilibrium, the point defect chemistry can be affected by the introduction of aliovalent substitutional impurities. Impurity atoms in a crystal can be considered as extrinsic point defects and they play a very important role in the physical and mechanical properties of all materials. Impurities can take up two different types of site: substitutional, in which an atom of the parent lattice lying in a lattice site is replaced by the impurity atom (Figure 1.5c), and interstitial, in which the impurity atom is at a non–lattice site similar to the self–interstitial atoms referred to above.

Charge balance severely influences the nature of point defects created after the removal or addition of atoms in an ionic crystal. In the structure of magnesium oxide, for instance, each negatively charged oxygen ion is surrounded by six nearest neighbours of positively charged magnesium ions and vice versa. The removal of a magnesium or an oxygen ion produces two local negative or positive charges, as well as a vacant lattice site. These are called cation and anion vacancies, respectively. To conserve an overall neutral charge the vacancies must occur either in pairs of opposite sign, forming divacancies known as Schottky defects, or in association with interstitials of the same ion, forming the Frenkel

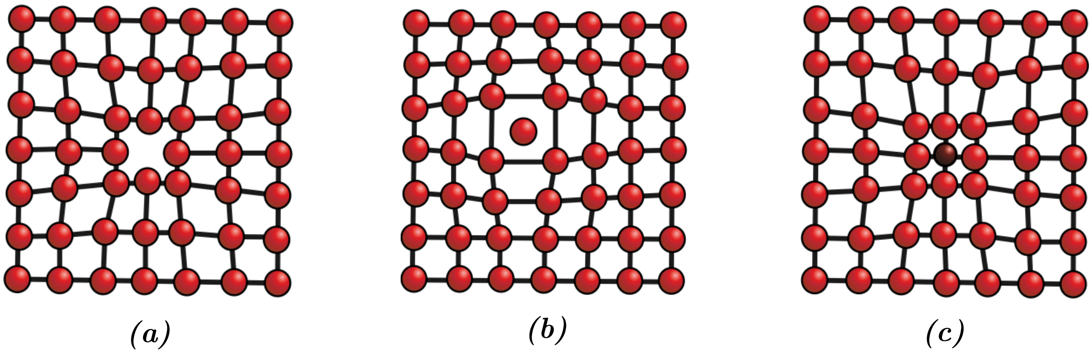

(a) (b) (c)

Figure 1.5: *point defects in a crystal: (a) vacancy; (b) interstitial and (c) substitutional atoms. Courtesy A. Goryaeva.*

defects (Hull and Bacon, 2001).

The presence of vacancies in a crystal enhances atomic mobility at high temperature. Under thermal vibrations, a neighboring atom can jump into a vacancy position. This is formally equivalent to the opposite jump of the vacancy, defining the vacancy diffusion coefficient D_v:

$$D_v = D_{0v} \exp\left(-\frac{\Delta H_m}{k_B T}\right) \tag{1.2}$$

where ΔH_m is the activation enthalpy for the migration of vacancies and D_{0v} is a prefactor containing entropic terms. The mobility of an atom by diffusion is thus bonded to the presence of a neighboring vacancy and the self–diffusion coefficient D^{sd} of the atomic species will be a function of the relevant vacancy concentration:

$$D^{sd} = c_0 D_v = D_0 \exp\left(-\frac{\Delta H_f + \Delta H_m}{k_B T}\right) \tag{1.3}$$

where D_0 is a prefactor and c_0 was described above.

This law describes self–diffusivity of intrinsic defects, as the formation enthalpy term takes part in the thermally activated barrier that the defect, in order to diffuse, has to overcome. In the case of extrinsic diffusion, substitutional impurities contents will drive the formation enthalpy of point defects ΔH_f. In this case, the diffusion barrier will depend only on the migration enthalpies of defects. The extrinsic vacancy self–diffusion coefficient can hence be defined as $D^{sd} \propto X_v D_v$ where X_v is the extrinsic vacancy concentration and D_v the vacancy diffusivity described in equation 1.2

1.2.2 Dislocations

Line defects were first theorized by Volterra (1907). He defined two types of lattice distortion, one due to translational defects and another to rotational ones. Translational defects are commonly denominated dislocations. Rotational defects are known as disclinations, and are tightly related to grain boundaries. Given that this study addresses the intracrystalline plasticity of minerals, hereafter only dislocations will be treated.

A dislocation is a linear defect that cannot end in a crystal. It must terminate on another defect, *e.g.*, on a grain boundary or on a surface, or on itself, forming a loop. In the context of plastic deformation, it delimitates the areas where slip has already taken place from the undistorted domains of a crystal. In other words, a sheared portion of a crystal is delimitated by a dislocation line and is translated with respect to the undistorted lattice by a slip vector b.

Strong evidence for linear defects arose from the attempts to reconcile the obtained theoretical and experimental values of the applied shear stress required to plastically deform a single crystal. In principle, deformation occurs by atomic planes sliding over each other. In a perfect crystal, *i.e.* in the absence of dislocations, the sliding of one plane over an adjacent plane would have to be a rigid cooperative movement of all the atoms from one position of perfect registry to another. The shear stresses required for this process are many orders of magnitude greater than the observed values of the resolved shear stress for slip measured in real, well–annealed crystals. This striking difference between prediction and experiment was accounted for by the presence of dislocations independently by Orowan (1934); Polanyi (1934) and Taylor (1934). These simultaneous works set the dislocation–based theory of crystal slip together with the definition of edge dislocation. The so–called screw dislocations were described later by Burgers (1939).

Locally, dislocations are characterized by a line vector L and by the Burgers vector b. The Burgers vector is quantized in the case of crystals and normally it corresponds to the shortest translation vectors of the crystal structure. This results from the elastic energy per unit length of dislocations, which scales with b^2. An edge dislocation corresponds to the case where L is perpendicular to b, whereas a screw dislocation corresponds to the case where L is parallel to b (Figure 1.6). In most cases, the dislocation lines are curved and the actual orientation of these two vectors is in between the edge and screw configurations, corresponding to a mixed character. Schematically, the edge dislocation is commonly represented by the insertion of an extra–half plane, while the screw dislocation is a pole around which the atomic planes are spiraling.

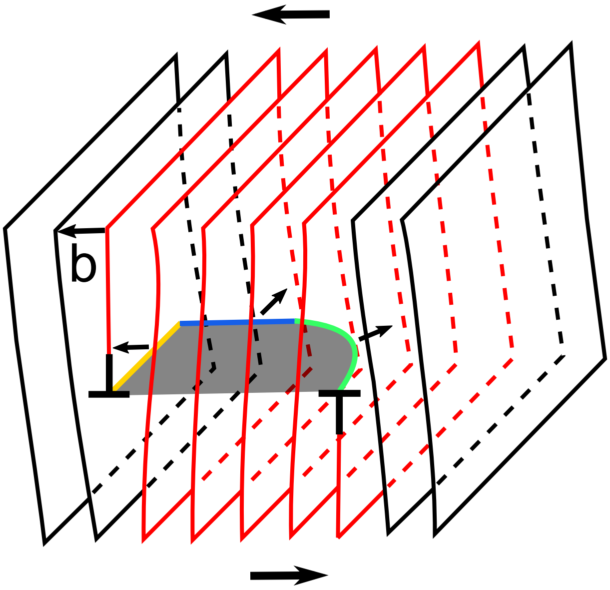

Figure 1.6: *schematization of a crystal, represented in crystallographic planes, containing half of a dislocation loop. The loop divides the sheared part of the crystal (marked in red) from the undistorted one (black planes). The slipped area (gray shading), lies in the glide plane. One edge dislocation line (yellow segment) is visible with the associated extra half plane, as well as the helicoid distortion of atomic planes revolving around the line with screw character (blue segment). Each turn of the screw corresponds to a displacement described by the Burgers vector b. Shear stress direction is also shown. Upon the action of stress, the dislocation loop expands. Normally, vast portions of dislocation loops present curved dislocation lines having mixed character (green segment). Modified from Poirier (1985).*

The presence of a dislocation in a crystal distorts the atomic planes and is responsible for a surrounding elastic displacement field, which in turn gives rise to a strain and a stress field. An important property of dislocations is that all the stress field components vary as:

$$\sigma \propto \frac{\mu b}{r} \tag{1.4}$$

where μ is the shear modulus and r the distance from the line. It can be seen that stress (this is also the case for strain) becomes infinite as r approaches zero. Linear elasticity used to derive this relation breaks down in the region near the dislocation line which is called the core. In this region, crystal lattice is highly distorted and involves specific configurations with large atomic displacements. Accurate description of this region at the atomic scale is reached through atomistic calculations. Based on numerous physical–based models, the characterization of dislocation mobility can be achieved through this technique. In this study, several results of atomic scale simulations will be plugged as input parameters into single crystal plasticity models of lower mantle minerals (*cf.* Chapters 2, 3 and 4).

Dislocation mobilities and interactions represent the key mechanisms underlying the models performed in the present work. While their detailed description and application is presented in the next chapter, here some hints are provided.

Under an applied stress, a dislocation may move in the plane containing both the dislocation line L and the Burgers vector b. This motion is called glide and it is conservative, since it does not involve exchange of matter. It just requires the breaking and reconstruction of atomic bonds. For any dislocation having an edge component, this motion is restricted to a unique glide plane (*cf.* Figures 1.6 and 1.7a), while a screw dislocation can, in principle, glide in any plane containing the Burgers vector.

In between two neighboring stable positions, the dislocation, in order to glide, must explore unstable configurations with higher energies, described by the so–called Peierls potential. The crystal lattice thus opposes a friction force, called lattice friction, to the dislocation motion. This force is maximum for a straight rigid dislocation moving without the assistance of thermal activation – *i.e.*, at 0 K. In this case, the material–dependent stress necessary to move the dislocation by glide is called the Peierls stress and quantifies the entity of lattice friction. At finite temperature, dislocations glide at stresses lower than the Peierls stress due specific thermally activated mechanisms. Generally, just a small portion of the line glides to the next plane, creating a step on the slip plane which is called kink.

Above a given athermal temperature T_a, thermal activation overcomes the lattice friction and dislocations are free to glide under the applied stress. In this regime, the dislocation velocity is proportional to the applied resolved shear stress and the flow stress is only controlled by dislocations–dislocations interactions in the microstructure. In fact, even if thermal activation is sufficient to displace dislocations, in this regime they generally cannot move freely through the crystal. Immobile dislocations crossing the slip plane of moving segments can act as obstacles and block the motion, generating a dislocation pile–up. At higher temperatures, atomic diffusion becomes non–negligible and other mechanisms like dislocation climb can operate. Climb allows for the slow, progressive escape of segments from the pile–up, through the migration to a parallel plane. At this stage, the rate of escape – strongly bonded to the climb rate – and not the average velocity of dislocation, is the factor controlling creep.

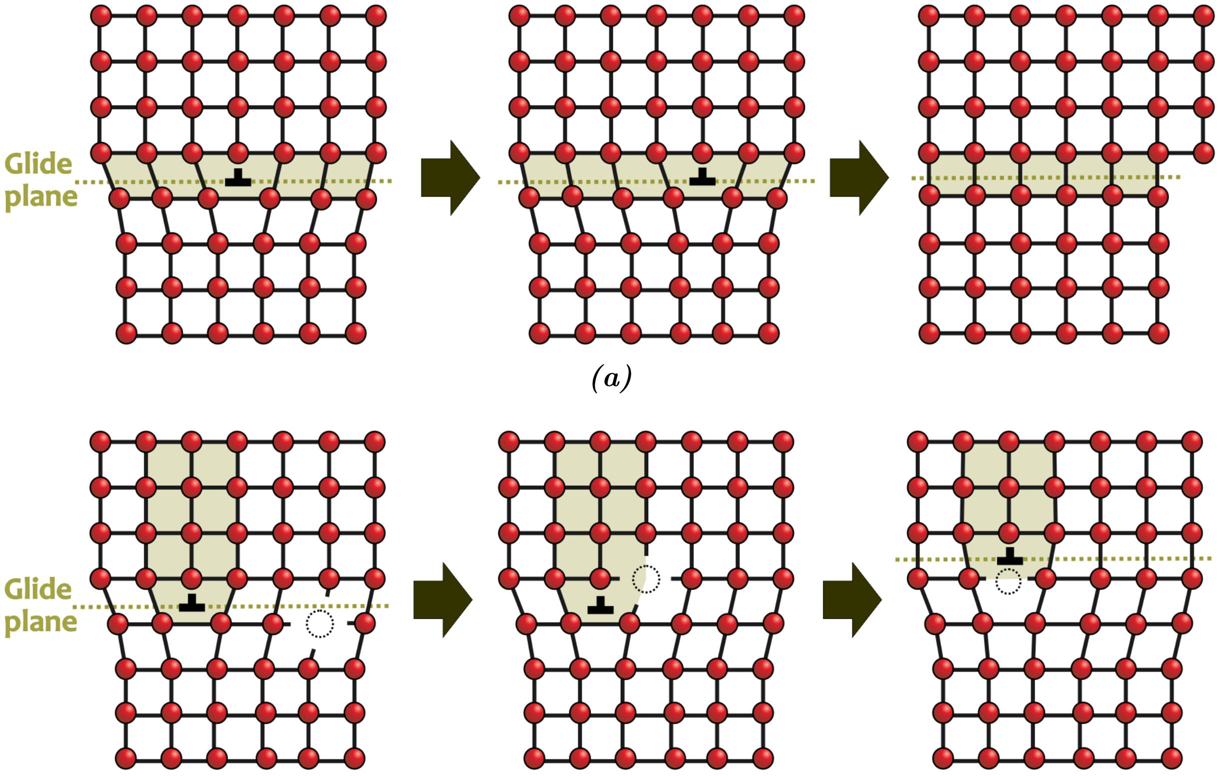

(a)

(b)

Figure 1.7: Schematization of the motion by glide (a) and climb (b) of an edge dislocation. While glide is a conservative motion, climb involves the exchange of matter from or to the dislocation line. Once the climb motion has taken place, the dislocation is free to glide in the new glide plane.

With high temperatures and efficient diffusion, in fact, dislocations can act as sources or sinks for vacancies. This exchange of matter from or to the dislocation line, mediated by diffusion of point defects, underlies the climb mechanism. This motion takes place through the adsorption or emission of matter to the line, which will then present several steps outside the glide plane in the climb direction, that is, perpendicularly to the glide plane. These features are named jogs and act as sources and sinks for vacancies. A sketch of a gliding and climbing edge dislocations is shown in Figure 1.7.

1.3 From crystal defects to creep

Creep consists in a macroscopic flow resulting from the motion of defects at the microscopic scale. One way to describe creep mechanisms is to analyze empirically the results obtained from a constant stress test on a sample or a computer simulation. On the other hand, at the microscopic scale, the identification of the relevant state variables (*i.e.*, dislocation density, grain size, *etc.*) describing the microphysical state of the material is a primary factor for a proper analysis from first principles. When a state variable is time– or strain–independent, it can be fully determined by external variables. In this case, the strain rate can be evaluated as a direct function of stress, temperature, pressure and other material parameters (*i.e.*, moduli, lattice parameters, diffusivity, *etc.*) and the creep regime is defined to be at the steady–state. The microscopic time–independence of state variables describing steady–state creep finds its macroscopic equivalent in a constant creep strain rate observed for crystals deforming under a constant applied stress. Here the constitutive equations relevant for this study will be outlined, starting from the phenomenological ones (*i.e.*, empirical relations coming from the observed creep behavior) and following with a description of the main analytical models obtained with a rigorous derivation of theoretical concepts. Given that my focus is mostly on dislocations and point defects, the coming description will be based on diffusion and dislocation creep laws.

1.3.1 Dislocation creep – phenomenological relations

Usually, in high–temperature creep, it is considered that several mechanisms (glide and climb) are operating simultaneously and thus, differently from diffusional creep, there exist no simple model capable of completely (and quantitatively) characterize dislocation creep.

The essential transport equation describing the plastic strain that results from dislocation motion is the Orowan equation. As stated above, the elementary deformation carried by dislocation is quantized in the case of crystals, by a quantum of displacement defined by the Burgers vector b. Knowing this entity, the concentration of mobile defects ρ and their velocity, in principle, a microscopic equation of state for steady–state creep (*i.e.*, the Orowan equation) can be obtained:

$$\dot{\varepsilon} = \rho b v \tag{1.5}$$

where v is the average velocity of the mobile dislocations. This equation is valid for dislocations moving either by glide or climb and therefore provides a useful tool to characterize a creep phenomenon. On the other hand, several issues may arise. First of all, in a dislocation microstructure many obstacles (including immobile dislocations) can impede the motion of mobile dislocation segments. This makes extremely difficult to precisely estimate the mobile dislocation density and even more to assign to those mobile segments an accurate value of average velocity.

Other than microstructural characteristics, a major point on the mechanisms controlling creep needs to be raised: creep may not be controlled exclusively by glide (or climb) motion. In the vast majority of cases, in fact, the process controlling the creep rate is not the same as the one that produces the strain. This is well explained in a more general expression characterizing steady–state creep, the Bailey–Orowan equation:

$$\dot{\varepsilon} = \frac{r}{h} \tag{1.6}$$

where r is the recovery rate and h is the hardening rate. It is easily demonstrated (Poirier, 1985) that if r and h are described in terms of dislocation mechanisms, this equation collapses into equation 1.5. Bailey–Orowan equation recalls the first Ohm's law of electric current. It shows that the creep rate at the steady–state is intimately related to the competition between hardening mechanisms that increase the dislocation density (*i.e.*, dislocation glide) and recovery mechanisms facilitating its decreasing (*i.e.*, dislocation climb).

As will be discussed in the next chapter, these different dislocation dynamics take place in very differing timescales. This, once again, renders extremely difficult an appropriate evaluation of an averaged value of velocity.

As discussed by Poirier (1985), macroscopic constitutive equations for dislocation creep result from a phenomenological analysis of quasi–steady state creep.

It was noticed since early works (Andrade, 1910) that the creep rate holds an exponential dependence with respect to temperature:

$$\dot{\varepsilon} \propto \exp\left(-\frac{Q}{k_B T}\right) \tag{1.7}$$

where Q is the creep activation enthalpy. Similarly, it was found that in most cases, given that the steady–state condition was reached, the creep rate manifested the dependence on stress by a power law, *i.e.* $\dot{\varepsilon} \propto \sigma^n$, where n is the stress exponent.

The thermal activation of the creep rate and its strong stress sensitivity has led to the definition of high–temperature creep–rate based on the empirical equation proposed by Dorn (1955):

$$\dot{\varepsilon} = \dot{\varepsilon_0} \sigma^n \exp\left(-\frac{Q}{k_B T}\right) \tag{1.8}$$

This equation can be found under several variants in the literature. Experimentalists have tried to develop the pre–exponential term $\dot{\varepsilon_0}$ to incorporate the influence of several parameters like the oxygen fugacity, water fugacity, chemistry, *etc.* On the other hand, the fact that the activation energy for creep Q is usually close to the activation energy for self–diffusion has led to propose models for recovery–controlled power law creep, such as Weertman creep (which will be discussed later on). The stress exponent n is equal to 1 if creep is fully due to diffusion processes (linear rheology), while the semi–quantitative interpretation of the afore–mentioned empirical models for dislocation creep gives a stress exponent which is typically in the range of 3–5.

A first–order explanation of this finding can be proposed in the case of climb–controlled recovery creep. Following the Orowan equation 1.5, in this case it is necessary to estimate the stress dependence of climb velocity and dislocation density. The first, for relatively small applied stresses, depends linearly on the stress (*i.e.*, $v_c \propto \sigma$, *cf.* Section 2.4.2, equation 2.9 and relative comments). Concerning dislocation density, it scales on a characteristic length l_c describing a general dislocation array:

$$\rho \propto \frac{1}{l_c^2} \tag{1.9}$$

This characteristic length will also be related to the arrangement of dislocation lines: the stress field that dislocations originate interacts with the one of surrounding segments, setting an equilibrium distance between dislocations. As previously discussed, this stress scales with the inverse of the distance between segments (*i.e.*, $\sigma \propto l_c^{-1}$, *cf.* equation 1.4). It follows that:

$$\rho \propto \sigma^2 \tag{1.10}$$

which gives a power 2 dependence of stress on dislocation density and a power 1 dependence on climb velocity, resulting in the typical stress exponent $n = 3$ commonly observed. Less efficient recovery due to low temperatures, high impurity content, high stress levels, *etc.*, results in a shift of n towards higher values.

Among the many models attempting to describe recovery–controlled creep, the early one of Weertman (1955; 1968) is worth to be discussed. Being the first one attempting to provide a theoretical basis explaining the results described by the power law equation, it acts as a source from which many other models can be derived.

The scenario reproduced in this model is one in which dislocations produced by sources are moving by glide and getting trapped in a minimum energy configuration due to dislocation–dislocation interactions. A diffusion–controlled recovery process (such as dislocation climb) is then advocated to promote the annihilation of the interacting segments. This allows other dislocations formerly trapped in the minimum energy configuration to move and further produce deformation by glide. In other words, this model reproduces the behavior described in the Bailey–Orowan equation 1.6, with dislocation multiplication promoting hardening and climb underlying recovery.

The vast applicability of this model is mostly owed to the stress exponents it can predict. Considering a stress–dependent density of dislocation sources, in fact, the withdrawn value of n is 4.5, often found in creep experiments. If, instead, the sources density is considered as stress–independent, n gets back to the expected value of 3 for recovery–

controlled dislocation creep (Poirier, 1985).

Finally, it should also be noted that the power–law equation can be found under different forms, including the one of Harper and Dorn (1957):

$$\dot{\varepsilon} = A_{HD}\frac{D\mu b}{k_B T}\left(\frac{\sigma}{\mu}\right)^n \tag{1.11}$$

where D is the self–diffusion coefficient and A_{HD} an empirical constant. With this formulation, they predicted a linear behavior ($n = 1$) at low stresses, while at higher stresses a normal power law stress behavior ($n = 4$) was envisaged. Despite an experimental basis backing up this observation (Yavari *et al.*, 1982), the mechanisms underlying this creep behavior are not fully comprehended and this equation shall still be considered as a semi–phenomenological relation.

1.3.2 Analytical creep models

The presence of point and line defects within a crystal makes possible the transfer of matter at accessible stresses. At temperatures high enough, these mechanisms may provide a significant contribution to plastic strain. If plastic deformation results exclusively from atomic diffusion, the process is usually called diffusion creep.

An elegant physical basis for this creep process has been proposed by Nabarro (1948), who was the first to point out that a non–hydrostatic stress field could give rise to different vacancy concentrations on different surfaces of a crystal. According to this description, the grain boundaries undergoing a normal compressive stress act as sinks of vacancies while the boundaries under normal tensile loading act as sources. This causes a flux of vacancies between surfaces, with an associate flux of ions in the opposite sense.

This kind of process can be of importance only if the flux of vacancies is large, *i.e.* if there are enough sources (grain boundaries), if the vacancy mobility is high enough and if diffusion distances are short enough. As a result, diffusion creep is expected to be efficient at very high temperatures and for very small grain sizes. This latter requirement also implies that dislocation sources cannot operate in small grains (unless the stress is quite high) rendering dislocation creep less efficient than diffusion creep.

The basic ingredient of this model is a cubic grain under a pure shear stress regime.

The latter is originated by non–hydrostatic stress fields on grain boundaries, which can give rise locally to different vacancy concentrations. In fact, surfaces undergoing a tensile stress will be enriched in vacancies, while a work against the compressive stress would be necessary to create vacancies on surfaces in compression. This disequilibrium of vacancy concentration results in a flux of point defects, from which the number of vacancies transported to a favorable surface of the cubic grain can be quantified (Figure 1.8a). Given that an opposite flux of atoms takes place simultaneously, an associated volume of diffusing matter can be estimated. If the total volume arriving per second at a surface is spread evenly, it creates a layer of given thickness at this surface. Therefore, the crystal elongates at a strain rate which can be quantified analytically, resulting in the physics–based constitutive equation of Nabarro (1948):

$$\dot{\varepsilon} = A_{NH} \frac{D\sigma\Omega}{d^2 k_B T} \tag{1.12}$$

where σ is the shear stress, Ω is the atomic volume and d is the grain size. A_{NH} is a numerical factor depending on the shape of the grain and the boundary conditions. Herring (1950; 1951) rigorously formalized the problem of creep by lattice diffusion in a polycrystal, finding an identical expression to the one of Nabarro. This earned the model the name Nabarro–Herring creep, in which A_{NH} has value 16 or 40 if grain boundary sliding is impossible or possible, respectively. If σ is instead considered as the engineering stress, A_{NH} shall be substituted by $A_{NH}/3$.

This creep mechanism has several important properties. First of all, it is linear viscous (Newtonian), *i.e.* $\dot{\varepsilon} \propto \sigma$. The creep rate is also strongly grain size dependent ($\dot{\varepsilon} \propto d^{-2}$). This explains why the diffusion creep mechanism is usually considered to be active in small–grained materials at high temperatures and low stresses.

The pure shear deformation mode characterizing this model is responsible for the redistribution of matter within the crystal under the work of the applied stress. As a consequence, no strong lattice preferred orientations are originated. Knowing this fact, the absence of significant anisotropy in the Earth's lower mantle was often advocated as proof for diffusion creep being the most relevant deformation mechanism (Karato and Li, 1992). On the other hand, a very reduced grain size is necessary for it to be true, and the lack of evidences backing this fact leaves the issue still unresolved.

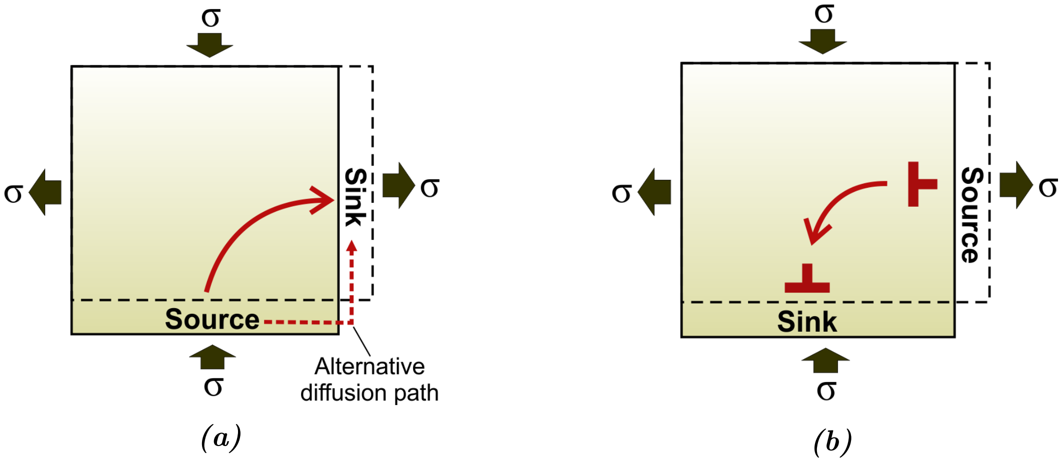

Figure 1.8: *schematic illustration of a vacancy path in diffusion creep (a) and pure climb (Nabarro, 1967) creep (b). The non–hydrostatic stress σ is applied to the crystal (represented here as a square), resulting in tensile and compressive components on different surfaces. In this configuration, the deformation mechanism is simple shear. In both cases, the arrows describe the motion of an atom within the lattice. Courtesy A. Goryaeva.*

Alternatively, diffusion could occur preferentially along grain boundaries (Coble, 1963). This mechanism, called Coble creep, is characterized by a slightly different rheological law which is still Newtonian viscous and grain–size dependent:

$$\dot{\varepsilon} = A_C \frac{D^{gb}\delta\Omega\sigma}{d^3 k_B T} \tag{1.13}$$

Where A_C is a constant, D^{gb} is the diffusion coefficient along grain boundaries and δ is a phenomenological parameter characterizing the thickness of the grain boundaries with respect to the diffusion process.

Nabarro–Herring and Coble creep mechanisms will dominate if grain boundaries are the effective sources and sinks for diffusing species. The crystals (grains) may however contain defects playing the same role. Nabarro (1967) has suggested that dislocations could serve as sources and sinks for diffusing species. These dislocations must have different Burgers vectors for sources and sinks and will move by climb.

This approach shifts the sources and sinks from the boundaries of a crystal to dislocations, which lie in its interiors. The characteristic length of diffusion, therefore, is smaller (favoring the creep efficiency) and is not anymore grain size–dependent (Figure 1.8b). In the treatment proposed by Nabarro (1967), this creep process follows a law of the type:

$$\dot{\varepsilon} = \frac{D^{sd}\mu b}{\pi k_B T}\left(\frac{\sigma}{\mu}\right)^3 \Big/ \ln\left(\frac{4\mu}{\pi\sigma}\right) \tag{1.14}$$

Given its importance for the present work, this model will be further described in Chapter 4, where it will be employed to model the creep behavior of bridgmanite under lower mantle conditions.

1.4 Mineral phases addressed in this study

In this thesis work the creep properties of mineral phases relevant for the Earth's lower mantle are addressed. First, a recently developed numerical modeling method is applied to pure MgO at ambient conditions for a proper benchmark (Chapter 2). Then, with a proper definition of the key inputs, it is here employed to model creep of (Mg,Fe)O at Core–Mantle Boundary (CMB) conditions (Chapter 3). Finally, the creep behavior of bridgmanite through the lower mantle is modeled analytically (Chapter 4). Here some insights are provided on these minerals, which together constitute up to 90% of lower mantle assemblages (*cf.* Figure 1.2).

1.4.1 Ferropericlase–magnesiowüstite

Ferropericlase (Mg,Fe)O alloying *ca.* 18 mol% of iron is the second most important phase of the lower mantle after bridgmanite (Irifune, 1994; Wood, 2000). A full solid solution (Mg_x,Fe_{1-x})O is compositionally available. This compound is ionic at the Mg–rich end–member while at high iron concentrations the nature of the bonding is shifted towards a mixed ionic–covalent character. According to the nomenclature, ferropericlase and magnesiowüstite are terms used for $x > 0.50$ and $x < 0.50$, respectively. MgO is called periclase, from the Greek $\pi\varepsilon\rho\iota\kappa\lambda\acute{\alpha}\omega$, to break around, in allusion to the cleavage. FeO goes under the name of wüstite.

This mineral is stable at ambient conditions and has been shown to remain stable at pressures up to 360 GPa (McWilliams *et al.*, 2012). (Mg,Fe)O exhibits a cubic, face–centered rock salt structure (space group $Fm\bar{3}m$, $Z = 4$). In this structure, Mg and O atoms form identical sublattices that represent a cubic stacking of close–packed planes parallel to $\{111\}$.

At ambient conditions, the easiest slip system in MgO is $1/2\langle 110\rangle\{110\}$, followed by $1/2\langle 110\rangle\{100\}$ (Haasen *et al.*, 1985; Foitzik *et al.*, 1989). Under high pressure conditions, only few experiments have been performed (Yamazaki and Karato, 2002; Heidelbach *et al.*, 2003; Li *et al.*, 2004). Pressures of the lower mantle were achieved by Merkel *et al.* (2002); Marquardt and Miyagi (2015) and Immoor *et al.* (2018) using a DAC at ambient temperature. The results of these studies show some discrepancies. While Merkel *et al.* (2002) conclude that $\{110\}$ are the only active planes, Yamazaki and Karato (2002); Heidelbach *et al.* (2003) as well as Li *et al.* (2004) suggest that glide in $\{100\}$ as well as in $\{111\}$, may contribute significantly to the total deformation. The Marquardt and Miyagi (2015) study finds that the strength of ferropericlase increases by a factor of three at pressures from 20 to 65 GPa, in excellent agreement with the theoretical prediction of Amodeo *et al.* (2012). In overall, from these experiments, it is difficult to conclude about the effect of temperature, pressure and strain rates on the deformation mechanisms of MgO under the lower mantle conditions.

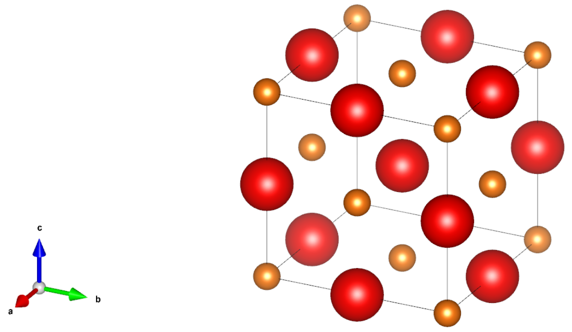

Figure 1.9: *Cubic cell of (Mg,Fe)O. Oxygen atoms are shown in red, magnesium or iron ones in orange. Ionic radii relative proportions between Mg and O are maintained.*

High pressure experiments (Badro *et al.*, 2003) on iron–bearing ferropericlase revealed that ferrous iron (Fe^{2+}) changes from a high spin state to a low spin state if pressure exceeds 60–70 GPa (around 1500 km of depth). While physical properties change across the transition, it has been found that the transition is very smooth (Sturhahn *et al.*, 2005;

Tsuchiya *et al.*, 2006) due to temperature effects which renders the transition essentially invisible to seismic waves.

Approaching the Core–Mantle Boundary region, thermal and thermochemical anomalies such as LLSVPs and ULVZs are detected due to seismic velocity reduction, and significant iron enrichments in the (Mg,Fe)O phase have been proposed as a reason for this evidence (Knittle and Jeanloz, 1986; Mao *et al.*, 2004b; Labrosse *et al.*, 2007; Sakai *et al.*, 2010; Wicks *et al.*, 2010; Fischer *et al.*, 2011; Ozawa *et al.*, 2011; Muir and Brodholt, 2015).

1.4.2 Bridgmanite

Bridgmanite (Mg,Fe,Al)(Si,Fe,Al)O_3, originally called magnesium silicate perovskite, is expected to compose 70–80% of the lower mantle (Irifune, 1994) and therefore it is likely the most abundant mineral in the Earth, making up for 38% of its volume. Bridgmanite has a wide range stability field from 24 GPa to *ca.* 125–135 GPa, corresponding to 670–2900 km depth. This phase was first discovered in nature in a heavily shocked Tenham meteorite (Tomioka and Fujino, 1997). In 2014, the mineral was named bridgmanite (Tschauner *et al.*, 2014) in honor of Percy Bridgman, the 1946 Nobel laureate in Physics, for his fundamental contributions to high–pressure research.

Bridgmanite has an orthorhombically distorted perovskite–type of crystal structure (space group $Pbnm$, $Z = 4$) with the unit cell parameters $a = 4.65$ Å, $b = 4.80$ Å and $c = 6.70$ Å at 30 GPa (Fiquet *et al.*, 1998). With increasing pressure, in fact, Si atoms change their typical tetrahedral coordination in favor of an octahedral configuration. Also, the site occupied by Mg increases to the 12–fold coordination structure. Orthorhombic distortion of bridgmanite (with respect to the cubic perovskite structure) results from rotation and tilting of the SiO_6 octahedra (Figure 1.10) and the offset in the position of Mg atoms. These structural distortions increase with pressure (Fiquet *et al.*, 2000).

High pressure deformation of bridgmanite is challenging to perform. Some recent experiments suggest indications of slip after transformation from San Carlos olivine in DAC (Wenk *et al.*, 2004) and from multianvil deformation experiments (Cordier *et al.*, 2004; Miyajima *et al.*, 2009). Recently, the first shear deformation experiments at lower mantle

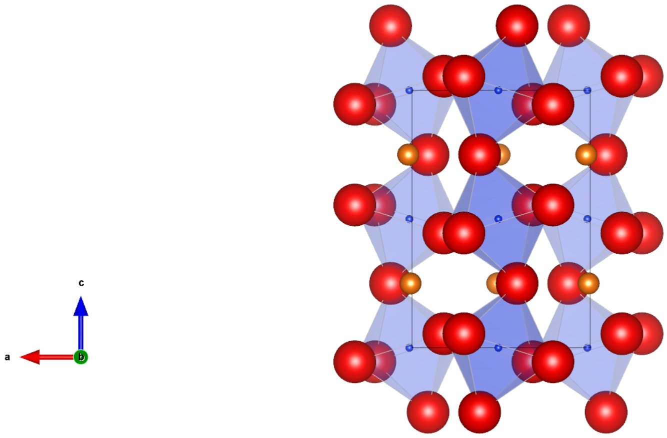

Figure 1.10: *Orthorhombic cell and crystal structure of bridgmanite seen along the* [010] *direction, with an emphasis on the tilting of the octahedral perovskitic structure. Oxygen atoms at the edges of the octahedra are displayed in red. Silicon atoms at the center of octahedral sites are shown in blue and interstitial magnesium atoms in orange. Ionic radii relative proportions are maintained.*

conditions of bridgmanite and magnesiowüstite aggregates were reported by Girard *et al.* (2015). Moreover, informations on deformation mechanisms and texture development were recently obtained by Nzogang *et al.* (2018).

Chapter 2

Modeling the plasticity of periclase by 2.5D dislocation dynamics

In this chapter[1], we present the 2.5–dimensional (2.5D) dislocation dynamics (DD) simulation approach that we have used and adapted to model the plasticity of MgO (periclase). This formulation incorporates dislocation climb in DD simulations, providing an instrument to model creep at high temperatures. Climb is a non–conservative process, since it involves an exchange of matter between the dislocation lines and the surrounding bulk of the material. For this reason, as described above (Section 1.2.2, Figure 1.7), dislocation climb strongly depends on self–diffusion, which will be evaluated through an analysis of the literature.

Recently, substantial developments have been achieved to model plasticity based on multiscale numerical modeling, however, most efforts were devoted to metallic systems. In non–metallic solids, developments have been made on MgO because of the general interest for its properties and the abundant experimental data that are available for benchmarking. Starting from the atomic scale, the individual properties of gliding dislocations have been modeled, leading to a satisfactory description of lattice friction and of the critical resolved shear stresses of single crystal MgO as a function of temperature (Amodeo *et al.*, 2011) and pressure (Amodeo *et al.*, 2012). Furthermore, this approach has been extended to the plastic behavior of aggregates under pressure (Amodeo *et al.*, 2016). So far, these models could only take into account dislocation glide. Since the relevance of MgO is

---

[1] The present chapter is based on the following journal article: Reali, R., Boioli, F., Gouriet, K., Carrez, P., Devincre, B., and Cordier, P. Modeling plasticity of MgO by 2.5D dislocation dynamics simulations. *Materials Science and Engineering: A*, 690:52–61, 2017. doi: 10.1016/j.msea.2017.02.092.

mostly related to high–temperature applications or to its creep behavior in the Earth's mantle, a further effort was needed to model creep in MgO at high temperatures. In fact, under these conditions, dislocation climb is expected to play a significant role during creep deformation and needs to be included in the model.

The influence of climb on MgO plasticity is addressed here by using 2.5D–DD simulations. Within this method a simplified 2D framework is defined and local rules are included, in order to take into account the relevant 3D mechanisms driving deformation. This allows for the adoption of a simple model that can capture the most important 3D dislocation features and readily include the interplay between glide and climb in the high temperature regime.

The 2.5D–DD method is first used to describe the plasticity of MgO in the low ($T \leqslant 600$ K) and intermediate ($T = 1000$ K) temperature regimes, where only dislocation glide is active. This benchmarks the 2.5D approach against 3D–DD simulations. Furthermore, comparisons with experimental data are also made, to show that the 2.5D–DD simulations are able to reproduce the key features of deformation in these two temperature regimes. Then, dislocation climb is introduced to model creep in the high temperature regime ($1500 \leqslant T \leqslant 1800$ K). The obtained results are compared with data from MgO creep experiments.

It is shown that, taking into account the range of oxygen self–diffusion coefficients available in the literature, the performed simulations describe properly the high–temperature creep behavior of MgO. This validates the model implemented in this chapter and allows for further investigation at lower mantle conditions.

Keywords: MgO; high–temperature plasticity; creep; 2.5D dislocation dynamics

2.1 2.5D dislocation dynamics

2.1.1 Model description

Dislocation dynamics simulation is a modeling tool which describes the collective motion and interactions of dislocations at the mesoscale. This technique is based on continuum elasticity theory, which provides the description of the elastic field induced by dislocations in a crystal, their interactions with each other and with respect to the stress field resulting from external loading (Hirth and Lothe, 1982).

Although several DD codes have been designed to model different processes and materials, they all share a few key features. First, they rely on the discretization of space and time. Dislocations, also, are discretized into a finite ensemble of line segments, such as in the present case, or nodes. Then, forces acting on each segment are calculated from elasticity theory and, subsequently, the velocity of each segment is evaluated according to a material–dependent equation of motion. The displacements of segments are obtained by integrating velocity with a simple Euler algorithm. Furthermore, DD codes can account for the relevant atomistic processes controlling dislocation mobility and interactions by introducing local rules (Kubin *et al.*, 1992; Arsenlis *et al.*, 2007). The treatment of these local rules constitutes the main difference between DD codes. More insight on this procedure is provided in the next paragraph.

3D codes (including the DD formulations) can describe dislocation lines of edge, screw and mixed characters in a three–dimensional space, accounting for their curvature, topology and interactions. This approach naturally captures the evolution and organization of dislocation lines but it can be computationally demanding and remains impracticable for simulations aiming to reach large deformations.

A 2D formulation, where dislocation lines are treated as straight infinite lines, is sometimes sufficient to address some fundamental questions in plasticity. This method reduces the number of degrees of freedom with respect to 3D simulations but makes possible to reach potentially larger amounts of plastic deformation and to take into account dislocation properties which are difficult to model in 3D. On the other hand, the 2D modeling of dislocation dynamics fails to catch important dislocation properties such as dislocation line tension which controls, for instance, multiplication processes. The latter limitations may be overcome by adopting the so–called 2.5D–DD approach, where additional local rules are introduced in the 2D simulation plane in order to mimic as closely as possible important 3D mechanisms, such as dislocation sources or multiplication (Gómez-García *et al.*, 1999; 2006). This type of simulations has been successfully employed, for example, to investigate dislocation patterning (Gómez-García *et al.*, 2006) or to reproduce the transition between stage I and stage II in fcc metals (Benzerga *et al.*, 2003). In this work, dislocation climb is incorporated by adopting a 2.5D–DD approach, similarly to Davoudi *et al.* (2012), Keralavarma *et al.* (2012) and Boioli *et al.* (2015a). In order to characterize the dislocation behavior of periclase in a wide range of temperatures, different controlling mechanisms need to be encompassed in the model.

2.1.2 Force calculation, boundary conditions and time integration

In the 2.5D–DD method, dislocations are assumed to be perfect straight segments perpendicular to the reference plane and parallel to each other. All the dislocations are assumed to be of edge character and, as such, their Burgers vector lies in the reference plane.

Once a stress tensor σ is applied to a crystal, a force acts on every dislocation segment. This force is described by the Peach–Koehler formula, which reads:

$$F_{PK} = (\sigma \cdot b) \times L \tag{2.1}$$

where L is the dislocation line vector and b the Burgers vector. Its computation is a general and basic feature of all DD simulations and also the most computationally–expensive part.

The total force that is calculated at each dislocation segment in the simulation frame is the result of two main stress components: the applied stress field component σ_{app} which drives the dislocation motion and the non–local stress field σ_{int}, arising from the whole dislocation microstructure except the considered segment. In other words, $\sigma = \sigma_{app} + \sigma_{int}$. The total interaction resulting on each segment, calculated according to equation 2.1, is resolved along the glide and the climb directions, providing the component which is effective for the motion of the segment. This stress quantity (*i.e.*, the resolved shear stress) is henceforward defined as τ for the case of glide and τ_c for the case of climb – that involves a motion taking place perpendicularly to the glide plane.

The applied stress component σ_{app} is homogeneous within the whole simulation domain. The variation with respect to time of this component defines the mode of solicitation adopted in each simulation: constant stress (*i.e.*, creep) or constant strain rate (variable applied stress in order to maintain a constant deformation rate) simulations can be run separately. In this study, the constant stress mode was used for simulations where glide and climb are acting simultaneously, while in glide–only simulations, characterized by the absence of a recovery mechanism, the constant strain–rate mode was used.

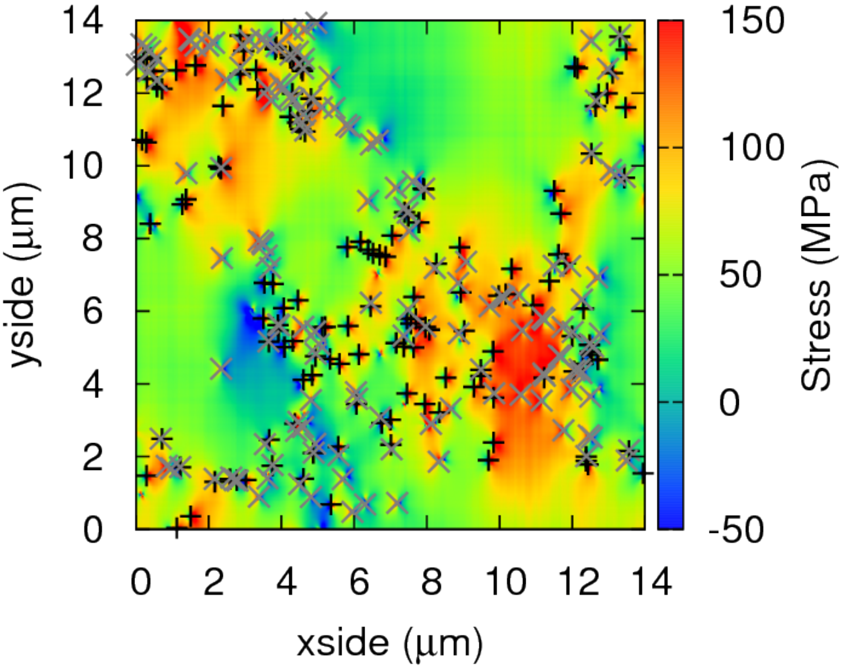

Figure 2.1: *an example of a microstructure obtained with the present code at 1600 K and 60 MPa of applied stress. In the domains of the box where dislocations are not present (and therefore the σ_{int} component is not significant) the total stress is comparable to the constant, homogeneous applied stress σ_{app} (identified by a greenish color). Dislocations are marked by the + and × symbols, in case they are characterized by a positive or negative Burgers vector, respectively. Dislocations interact with each other, perturbing the applied stress field and originating the interaction stresses that characterize each step of the calculation.*

The calculation of the internal stress component σ_{int} is the important part of the simulation and the main reason for the increase of computation time. It is in fact necessary to calculate the interaction of every segment with all the others and the computation time rises with the square of the dislocation segments' number. For this reason, numerical algorithms were developed in the past years in order to accelerate force computations.

The so–called "box method" (Shin *et al.*, 2006) is employed in this case, providing an efficient solution which decomposes the box in sub–domains for the long–range interactions calculation. Here the box is divided in nine domains and the internal stress on each segment is calculated by accounting for all the segments present in the same sub–domain together with single interaction values resulting from the segments belonging to each of the other sub–domains. Both the internal stress calculation and segment intersection treatment are computed by this domain decomposition method. The code has also been parallelized by using the standard message passing interface (MPI), resulting in a much improved efficiency.

Furthermore, periodic boundary conditions are used and the evaluation of long–range fields arising from outside the elementary simulation box is obtained from this last algorithm by summing the periodic contribution of the replicas. In fact, mirror images of the box surround it and each time a simulation segment moves outside the box, it is reintroduced at the same height but on the opposite side. This last point may cause some issues in case the glide planes are included horizontally in the box, since the reintroduced segment would fall on the same glide plane, strongly interacting with the dislocations already lying on it and creating an unwanted artifact. In the present study the directions of the box are chosen in order to obtain an oblique pattern of the glide planes belonging to the different glide systems, avoiding any possible artifact. This is described in the next paragraph.

Once the effective stress is known for the i segment, the velocity v_i is defined with the help of a mobility law. Practically, the glide velocity is locally determined by a balance between the elastic Peach–Koehler forces per unit length and a resistive dissipative force, which may arise from the thermally activated motion against the lattice resistance (known as the Peierls barrier) or phonon drag, in case glide takes place in an athermal regime. As v_i is character–dependent in many materials, more than one mobility law is usually defined. Here these two situations will be considered, in 2.2 and 2.3, respectively, depending on the thermal regime.

In this work we consider both glide and climb and these two mechanisms, when coupled, occur on very differing timescales. This difficulty is accounted for in the code by considering two different time steps, with a scheme close to the one proposed by Keralavarma *et al.* (2012). First, the creep stress is applied to the structure and all the glide events are resolved using the small glide time step. Once the configuration in the microstructure gets to a quasi–equilibrium or "jammed" state, dislocations do not glide anymore and the strain saturates. The threshold is set by calculating a floating average of the strain along the last 400 steps of the calculation. The difference between the average strain obtained in the first and second 200 steps of this interval is called $\Delta\varepsilon$. Once this difference is smaller than a specific value, here set at 10^{-23}, the "jammed" state is reached. At this point, climb motion is allowed by applying to dislocations a different mobility law and by integrating it through the longer climb time step. Once a displacement of a full Burgers vector is reached by climb, the mobility is switched back to glide again and the procedure is repeated iteratively throughout all the simulation.

Once a mobility law $v_i(t)$ is assigned and evaluated for each i segment, the displacements $r_i(t)$ are calculated at every step by integrating the velocity through the considered time step Δt. This is exemplified by a simple integration scheme:

$$r_i(t + \Delta t) = r_i(t) + v_i(t) \cdot \Delta t \tag{2.2}$$

In quasi–static deformation conditions, the explicit Euler forward (EEF) algorithm is the standard method of integration used in DD simulations (Devincre *et al.*, 2011) because it is computationally inexpensive.

In conclusion, in the present code, dislocation glide is coupled with climb in order to investigate plasticity at high temperatures. On the other hand, at low and intermediate temperatures, which are considered for benchmarking, climb is expected to play a minor role, and only glide is considered. Therefore, the key simulation inputs are the parameters chosen to characterize glide and climb mobility laws, a procedure which will be adequately described in the next sections of this chapter. The first step for the benchmark of the model is the definition of a proper simulation cell, accounting for the easiest slip systems and proper settings to couple dislocation glide and climb within the same spatial frame.

2.1.3 Simulation cell set–up

Periclase is an ionic, face–centered cubic oxide, which exhibits a rock–salt structure of space group $Fm\bar{3}m$ with a lattice parameter $a = 4.22$ Å. At ambient conditions, the easiest slip systems are $1/2\langle 110\rangle\{110\}$ followed by $1/2\langle 110\rangle\{100\}$ (Routbort, 1979; Carrez *et al.*, 2005), both having Burgers vector magnitude $b = 2.99$ Å. In this study, the focus is on dislocations of the easiest slip family – *i.e.* $1/2\langle 110\rangle\{110\}$ – and two slip systems belonging to it are introduced in the code. The simulation box is a square of size $L_x = L_y$ and dislocation lines are introduced as straight segments of constant length $L = 1$ μm, perpendicular to the reference plane. This 2D reference plane in our simulations is (111), where both the considered glide and climb directions lie, as sketched in Figure 2.2.

The considered slip systems are identified by the Burgers vectors $b_1 = 1/2[01\bar{1}]$ and $b_2 = 1/2[\bar{1}01]$. Hence, the dislocation lines are all of edge character and glide in planes (011) and (101), respectively. The dislocation climb direction is perpendicular to the glide direction. The reference system chosen for the simulation box has directions $\widehat{x} = [11\bar{2}]$ and $\widehat{y} = [\bar{1}10]$. The applied stress σ_{app} is applied along the $\widehat{y}$ direction in order to symmetrically load the two slip systems, resulting in a Schmid factor equal to 0.433 for both of them.

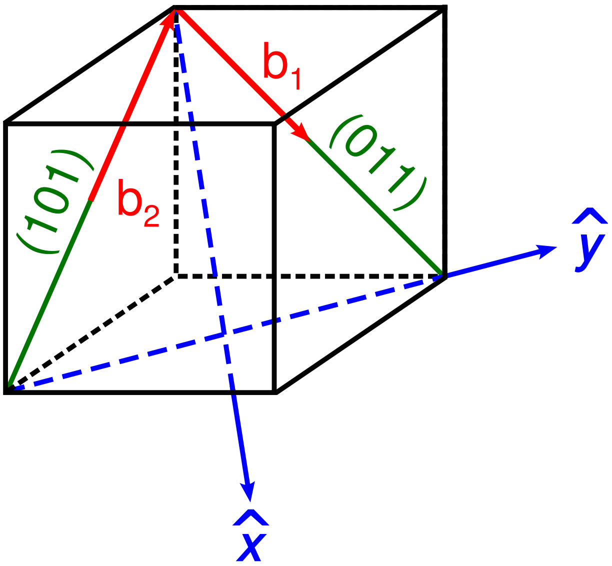

Figure 2.2: *representation of the cubic cell of MgO (in black) with the chosen burgers vectors b_1 and b_2 (red arrows), to which are associated the respective slip planes (green lines). The reference system axes $\widehat{x}$ and $\widehat{y}$ are identified by the blue arrows.*

Dislocations gliding in different planes may cross each other and form junctions which are oriented along the direction of intersection between the two planes. Planes of the $1/2\langle 110\rangle\{110\}$ family can intersect each other at 90 or 120 degrees and only in the latter case the sum of the two Burgers vectors is energetically favorable in order to create a junction (Carrez *et al.*, 2005). The resulting segment has an edge character and can potentially glide in $\{112\}$ planes, which are not among the reported easy slip planes of periclase. Here are considered two glide systems having the respective slip planes that form an angle of 120 degrees, allowing for the formation of junctions with Burgers vector $bj = b_1 + b_2 = 1/2[\bar{1}10]$, having the same orientation as $\widehat{y}$ (as it is shown in Figure 2.3).

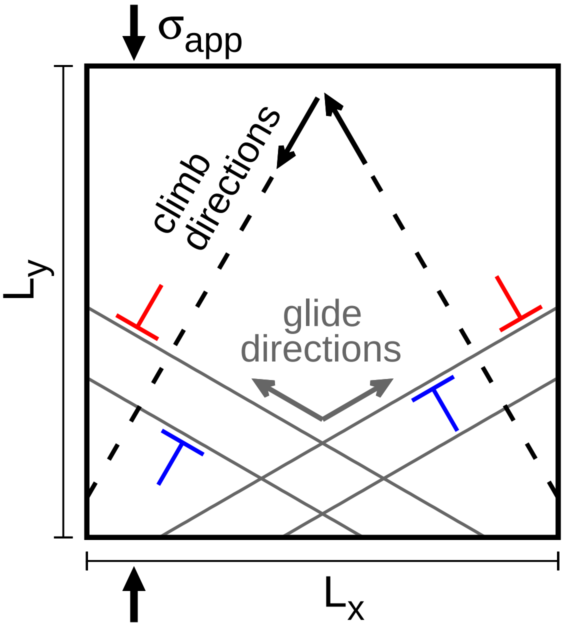

Figure 2.3: *sketch of the simulation box lying in the* (111) *plane, where dislocations belonging to the two slip systems glide on the respective planes (gray lines) accordingly to the directions of the two Burgers vectors* b_1 *and* b_2 *(gray arrows). Junction Burgers vector* b_j *is also shown. Black arrows and dashed lines show the two climb directions which are perpendicular to the glide planes. Stress* σ_{app} *is applied along* $\widehat{y}$ *direction. For the sake of simplicity, from now on* σ_{app} *will be referred to simply as* σ

2.1.4 Local rules overview

Concerning the choice of the elastic parameters, isotropic elastic constants for MgO are used. It is provided as an input a temperature–dependent shear modulus $\mu(T) = 140$ GPa $-0.0255T$ (Karki *et al.*, 2000) together with a Poisson ratio $\nu = 0.18$ (Amodeo *et al.*, 2014). Where not otherwise specified, an initial dislocation density $\rho = 10^{12}$ m^{-2} is set in the simulations, with a linear simulation frame size $L_x = L_y$ equal to 10 μm.

The major resistive factor against the motion of dislocation lines arises from the line tension, which acts on segments that bow out between intersecting dislocations obstacles. Hence, in a 2–dimensional formulation, line tension needs to be taken into account. A calculation of the sum of applied and interaction stresses in 3D and 2D shows that, on average, the effective stress must be scaled down by a factor of about five in the latter in order to appropriately incorporate line tension effects (Gómez-García *et al.*, 2006). However, depending on the thermal conditions at which dislocation move, the bowing of lines may be different, and this cutoff of stress shall not be identical for every regime. Consequently, in the present study, line tension was incorporated with a slightly different scaling, which could also allow to maintain the maximum stresses under control in the microstructure. Practically, if the resolved stress on a segment is more than six times the applied stress, this value is considered as a singularity and a new value of stress is assigned. In particular, the value of the applied stress resolved along the glide direction is assigned.

Laws governing dislocation multiplication and annihilation are included in the 2.5D–DD code to reproduce these fundamental 3D mechanisms, as proposed by Benzerga *et al.* (2003) and Gómez-García *et al.* (2006). First, a law reproducing the experimental observation that the dislocation density increases linearly with the plastic strain $d\rho/d\varepsilon = m$ is used. Here m is the rate at which the dislocation density increases with the plastic strain, assuming annihilation events not to occur or to be rare. This law describes the expansion of dislocation loops in a 3D volume under the influence of a stress field. In the present work, the constant m is 10^{15} m^{-2} according to the results of 3D simulations in duplex slip. Furthermore, an annihilation rule is used to reproduce the fact that dislocations forming a dipole (*i.e.*, two dislocations having the same Burgers vector but of opposite sign) can mutually annihilate when they approach each other. The annihilation rule consists in allowing the dislocations that form a dipole to annihilate when the height of the dipole (*i.e.*, their distance) is smaller than a critical value given as an input parameter.

These two rules are applied in all three temperature regimes. Nevertheless at low and intermediate temperatures, while multiplication is constantly operating through the motion of dislocation lines, the annihilation events take place less frequently. This is due to the absence of recovery processes, such as climb or cross–slip, that allow dislocations to move from one slip plane to another one, hence promoting dislocation–dislocation annihilation. In fact, these mechanisms are effective only at significant temperatures. As a consequence, in the first two regimes, annihilation events are quite rare, since dislocations cannot move out of their glide planes and the distance between two dislocations forming a dipole is given by the distance between their two slip planes. Thus, the evolution of dislocation density is mostly governed by the multiplication rule and it increases with the applied stress.

On the contrary, when at high temperatures climb is active, dislocations can change their glide plane by climb. Dislocations in a dipole configuration may consequently approach each other till they reach the given critical distance and annihilate. The dislocation density in the third regime is then controlled by the interplay between dislocation multiplication and dislocation annihilation promoted by climb. This leads to a steady–state condition where, with respect to time, the dislocation density fluctuates around an equilibrium value and the deformation increases linearly. These equilibrium values depend on the different stresses applied to the simulation box. Therefore, at ambient pressure, plastic deformation in MgO is expected to be controlled by several mechanisms depending on the temperature range investigated. These features and the respective modeling approaches will now be presented for the low ($T \leqslant 600$ K), intermediate ($T = 1000$ K) and high ($1500 \leqslant T \leqslant 1800$ K) temperature regimes.

2.2 Low temperature regime

2.2.1 Mobility description

At low temperatures ($T \leqslant 600$ K), dislocation glide dominates and plastic flow is controlled by the relatively low mobility of dislocations. The plastic strain limiting mechanism is then lattice friction, which involves a thermally activated kink–pair nucleation process (Amodeo *et al.*, 2011). In this thermally activated regime, the velocity v_g of a dislocation of length L can be described by the mobility law proposed by Kocks *et al.*

(1975):

$$v_g = b\frac{L}{l_c}\nu_D\frac{b}{l_c}\exp\left(-\frac{\Delta H(\tau)}{k_B T}\right) \tag{2.3}$$

where b is the magnitude of the Burgers vector, l_c is the critical width of kink pairs, ν_D is the Debye frequency, and $\Delta H(\tau)$ is the critical activation enthalpy of kink–pair nucleation as a function of the effective resolved shear stress τ acting on the considered dislocation. T is the temperature.

The kink pair activation enthalpy $\Delta H(\tau)$ in equation 2.3 is formalized in the present study accordingly to Kocks *et al.* (1975):

$$\Delta H(\tau) = \Delta H_0\left[1-\left(\frac{\tau}{\tau_P}\right)^p\right]^q \tag{2.4}$$

where ΔH_0 is the critical activation enthalpy at zero stress, p and q are empirical parameters. τ_P is the Peierls stress, *i.e.* the stress necessary to activate dislocation glide at 0 K: at this condition, in fact, dislocations can move under the influence of stress alone. This physical quantity provides an estimate of the lattice friction, the resistance opposed by the material to the movement of dislocation by glide. At finite temperatures, both the temperature and the stress contribute to overcome lattice friction. The parameters used for the glide mobility in this regime are provided by Amodeo *et al.* (2011) and reported in Table 2.1. Here it must be noted that the dislocation character considered in the 2.5D–DD simulation frame are of edge type, but the glide mobility law of equation 2.3, which is identified for screw dislocations, is applied to all dislocation characters for simplicity reason.

	$1/2\langle 110\rangle\{110\}$
τ_P (MPa)	150
ΔH_0 (eV)	1.14
p	0.5
q	2.0
l_c (nm)	33.8

Table 2.1: *parameters inserted in the glide velocity law (equation 2.3) for dislocation mobility in the thermally activated regime (from Amodeo et al., 2011)*

2.2.2 Numerical modeling

In order to model plastic deformation under these conditions, single slip simulations were run at constant laboratory strain rates (10^{-4} s^{-1}). The present model is validated through the comparison of the critical resolved shear stresses from these 2.5D–DD simulations with experimental (Hulse and Pask, 1960; Srinivasan and Stoebe, 1974; Sato and Sumino, 1980; Barthel, 1984; Appel and Wielke, 1985) and 3D–DD (Amodeo *et al.*, 2011) data obtained for MgO in the same range of temperatures and applied strain rates (that is, from 1 to $4.4 \cdot 10^{-4}$ s^{-1} for all the experimental data displayed).

Under a constant strain rate, initially, materials react elastically, up to the point where a threshold stress is reached and plastic flow takes place. Similarly, the simulated single crystals undergo to plastic deformation after an initial transient. The threshold stress is commonly denominated critical resolved shear stress (CRSS) and it is possible to evaluate it from the curves representing the resolved shear stress as a function of strain. In Figure 2.4 the stress–strain curves from our model are shown: dislocation motion in this regime is thermally activated and therefore it is strongly strain rate–dependent.

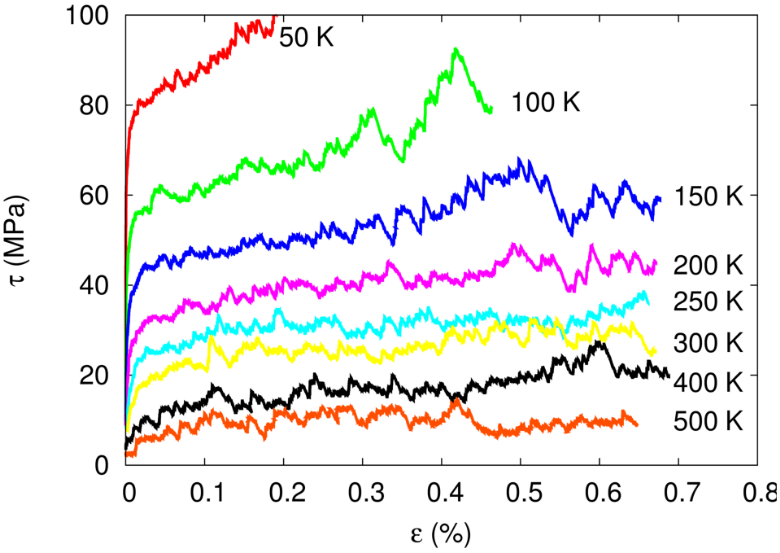

Figure 2.4: *resolved shear stress τ as a function of strain ε obtained at different temperatures in the thermally activated regime. The threshold value of stress at which plastic flow begins is the critical resolved shear stress (CRSS).*

Within practical computation time, plastic yield can be observed at lower stresses only if the temperature is raised. Furthermore, a relation between stress and strain after the yield point could be inferred from the obtained curves, but the relatively small values of hardening coefficient observed for this phase – less than 10^3 MPa as measured by Srinivasan and Stoebe (1974) – are difficult to reach without explicitly fitting some input parameters and significantly reducing the initial dislocation density. The evaluation of this feature is thus left to other studies. It is evident from this plot the importance of temperature: thermal activation, in fact, can drastically reduce the CRSS at the same applied strain rate. This is shown in Figure 2.5, where the CRSSs at different temperatures obtained in the present work are compared with other data obtained from numerical and experimental studies on MgO.

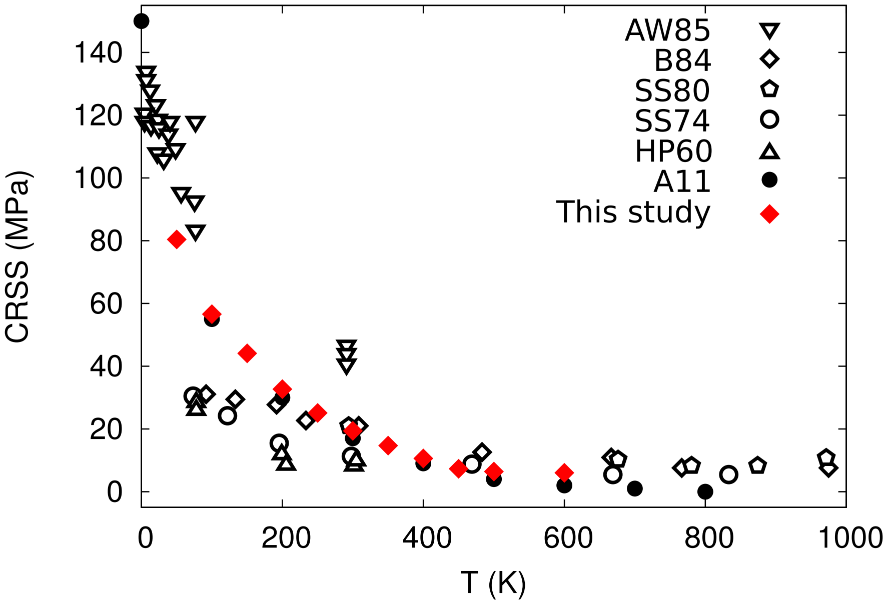

Figure 2.5: *CRSSs obtained in this study are compared with results from 3D–DD modeling of Amodeo et al. (2011) (A11) and other experimental data at different temperatures. HP60: Hulse and Pask (1960); SS74: Srinivasan and Stoebe (1974); SS80: Sato and Sumino (1980); B84: Barthel (1984); AW85: Appel and Wielke (1985)*

In the thermally activated regime, the agreement between the CRSS values obtained from our model and previous data is remarkable (Figure 2.5), especially with the 3D–DD outputs of Amodeo *et al.* (2011). The comparison with experiments is somehow more complex, since trivalent impurities can interfere with the gliding dislocations, while the modeled motion relies on the overcoming of lattice friction alone. Therefore, for a better comparison, were selected the experimental data obtained from samples having low impurity contents or being heat treated before analysis, in order to avoid the impurity–related strengthening effect.

2.3 Intermediate temperature regime

2.3.1 Mobility description and junction reproduction

At 600 K the athermal threshold temperature T_a is reached for the $1/2\langle 110\rangle\{110\}$ slip family (Amodeo *et al.*, 2011). Above T_a, lattice friction vanishes and the CRSS does not evolve with temperature anymore (*cf.* numerical and experimental data of Figure 2.5). In this athermal regime dislocations move by glide at the free–flight velocity v_{ath} commonly described by a viscous drag equation:

$$v_{ath} = \frac{b\tau}{B_v} \tag{2.5}$$

where b and τ were already defined and B_v is a viscous drag coefficient which varies linearly with temperature (Hirth and Lothe, 1982) and describes the complex interactions between the electric field of a moving dislocation and various elementary excitations, such as conduction electrons and phonons (Kubin, 2013). An experimental measurement of B_v for MgO is lacking, therefore values obtained at 300 K for other fcc oxides (Singh *et al.*, 2008) were assigned for our calculations, and were then scaled to the considered temperatures. In fact, the free–flight mobility law is not expected to play a relevant role in simulations describing plasticity in this regime (Amodeo *et al.*, 2014). This is because the average velocity of dislocations in the microstructure is limited by their interactions. For this reason, the forest density controls the plastic flow.

Dislocation junction and dipole formation are thought to be the main mechanisms driving strain hardening in fcc crystals. Cross–slip is a possible recovery process but is not included in our 2.5D–DD formulation and the evaluation of its role is left to other studies. However, an earlier numerical experiment on fcc crystals demonstrates that, while cross–slip favors the ordering of dislocation microstructures, it does not substantially influence the dislocation density and the stress–strain curves at low strain or low dislocation density

(Madec *et al.*, 2002).

Dislocation interactions and reactions are essentially athermal processes, which can conveniently be treated by elasticity theory. Dipole formation is constitutively taken into account in the code and dislocations forming a dipole are allowed to mutually annihilate when the dipole height is smaller than a critical distance $r_a = 25b$. The latter distance is a fitted value accounting for all possible annihilation reactions that may exist in 3D dislocation dynamics.

Reproducing junction formation and destruction in 2.5D is a delicate task since this reaction heavily affects the macroscopic average behavior of the structure. A junction is formed when two attractive dislocations gliding in different planes come to a distance smaller than the average length of junctions under stress, which is estimated from 3D simulations (Devincre *et al.*, 2006). When this happens, dislocations positions are blocked and the interaction stress between them is set to zero. Once a junction is created, the stress acting on it will be evaluated at each step in the same way described for single dislocations in Section 2.1.2. The junction will remain stable as long as the stress on each dislocation composing it is lower than a critical value τ_j. If this value is exceeded, the dislocations composing the junction will be unblocked and made free to move. In other words, τ_j represents the critical stress needed to break a junction. The local rule used in the DD code to break a junction is the following: when the resolved shear stress τ at the junction position reaches the critical value τ_j, the junction is broken. This value has been formalized by Gómez-García *et al.* (2006):

$$\tau_j = \beta \frac{\mu b}{\rho_l^{-1/2}} \ln\left(\frac{\rho_l^{-1/2}}{b}\right) \tag{2.6}$$

where ρ_l is the local density, that accounts for the local spatial heterogeneities in the dislocation density, and β is a constant that is set as an input parameter to recover reasonable values of the strength necessary to destruct the junctions, which in turn affects the flow stress. ρ_l is used here to estimate the length of the junction arm which drives the formation (destruction) of the junction through a zipping (unzipping) mechanism (Gómez-García *et al.*, 2006). A value of $\beta = 0.035$ is usually assigned for fcc metals. In this study, the influence of β on the mesoscopic plastic flow was investigated, running different sets of simulations having the same initial configuration and β values of 0.02, 0.05 and 0.1.

In the athermal regime, forest interactions are expected to control the plastic flow, leading to the commonly observed dislocation strengthening in fcc crystals. To characterize this type of behavior, the relation between flow stress and dislocation density must be investigated. A dislocation strengthening relation, having the form of the Taylor equation, is usually considered to estimate the macroscopic strength resulting from all possible local configurations in the microstructure:

$$\tau_f = \alpha \mu b \sqrt{\rho} \tag{2.7}$$

where α is a strengthening coefficient, ρ is taken as the total dislocation density, μ the shear modulus and τ_f is the effective average critical stress for all type of obstacles – *i.e.* the athermal stress required to overcome the forest dislocation network (Amodeo *et al.*, 2014). τ_f can be extracted from our DD simulations and it represents the stress acting on the microstructure in order to maintain constant the applied strain rate. This stress depends on the dislocation density: the higher the latter, the higher will be the stress applied to achieve the same deformation rate. In fact, as we mentioned above, in this regime the recovery mechanisms are not efficient, therefore a high dislocation density raises the number of forest obstacles which in turn prevent the mobile dislocation segments from further displacements.

Therefore, τ_f and the corresponding value of the dislocation density ρ are extracted from each simulation and plotted in order to estimate α, which in turn will provide an evaluation of the strength of the microstructure.

2.3.2 Numerical modeling

Simulations in this regime were run at $T = 1000$ K, in the duplex slip mode, and under a constant strain rate of 10^{-1} s^{-1}. Different initial dislocation densities were set equal to 10^{11}, 10^{12}, $5 \cdot 10^{12}$ and 10^{13} m^{-2}, in order to encompass a broad range of values for the estimation of α, which was then compared with results from experiments on fcc crystals and 3D–DD data obtained for MgO. In fact, without including recovery mechanisms, these simulations do not reach large plastic strain amounts, not allowing large increases in dislocation density either. Therefore, simulations starting with different initial dislocation densities are run to test forest strengthening at different virtual levels of strain (Madec *et al.*, 2002). No specific rules are provided for the estimation of the average strength and corresponding dislocation density (Kubin, 2013), therefore in this study the protocol defined by Amodeo *et al.* (2014) was employed, in order to better compare the data obtained: stress and dislocation density measurements are done after yield point, at relatively low plastic strains, as soon as the imposed strain rate is reached.

At 1000 K (around 0.3 T_m) the junction formation and destruction mechanisms drive the deformation behavior of MgO. These mechanisms require very high energies, which cannot be provided by thermal fluctuations, and therefore are considered to be essentially elastic and athermal processes (Kubin, 2013). Junction unzipping is the main softening mechanism considered in this regime, since it allows dislocations previously locked in a sessile junction to move and induce further plastic deformation. This process is introduced in the code through the scaling law showed in equation 2.6, where β is a dimensionless measure of the strength of a specific junction configuration. Varying the value of β will change the effective stress necessary to destroy junctions (*i.e.* τ_j), influencing the average stress acting on the microstructure (*i.e.* τ_f) in order to maintain the constant applied strain rate. Therefore, α and, consequently, τ_f depend on the choice of β.

Here we test different values for β in our 2.5D–DD simulations to verify for which values we recover the flow stress and the α values obtained by both full 3D–DD simulations results and experimental data. This can be seen in Figure 2.6a, where simulations run in the same initial configuration with distinct values of parameter β result in different stress–strain curves. The initial dislocation density is 10^{13} m^{-2} for each simulation displayed. The value of junction strength influences the average stress levels of plastic flow in the microstructure, while the dislocation density, due to the multiplication rule described above, remains comparable for all the three curves. In fact, in equation 2.7, ρ is taken as the total density, that is, twice the density of intersecting obstacles seen by each slip system during duplex slip. This process drives the evolution of stress as function of dislocation density, leading to the different α values obtained from the strengthening relation, which are shown in Figure 2.6b,c,d. For the three values of β which were tested – *i.e.* 0.02, 0.05

and 0.1 – the recovered values of α are 0.21(2), 0.26(2) and 0.37(3), respectively.

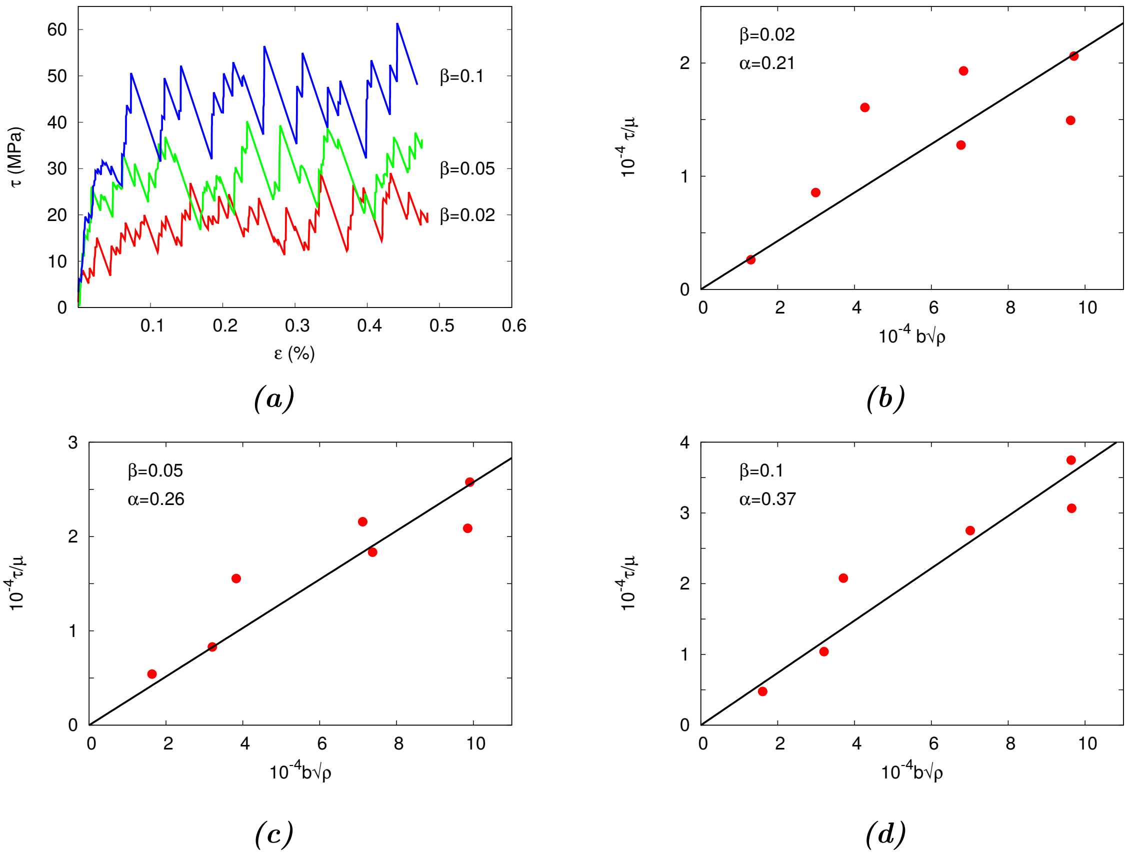

Figure 2.6: *resolved shear stress τ as a function of strain ε for three simulations having same initial settings and different values of junctions' strength β (a). Here, the initial dislocation density ρ is 10^{13} m^{-2}. (b), (c), (d): evolution of different flow stresses as a function of dislocation density obtained assigning to the junctions' strength parameter β values of 0.02 (b), 0.05 (c) and 0.1 (d). The retrieved α coefficients are shown in each graph.*

2.3.3 Discussion

The strengthening coefficients α obtained in this study from simulations at 1000 K are then compared with available experimental and numerical data. In the adopted 2.5D–DD framework, according to Gómez-García *et al.* (2006), $\alpha \approxeq 0.25$. This is close to the intermediate value obtained here (*i.e.*, for $\beta = 0.05$) and it is also in fair agreement with the result of $\alpha = 0.24$ obtained by Amodeo *et al.* (2014) from 3D–DD simulations on MgO for the $1/2\langle 110\rangle\{110\}$ slip family. For this reason, $\beta = 0.05$ was chosen for the main body of simulations run in the athermal regime.

The most reliable estimate from DD simulations on fcc crystals, on the other hand, yields $\alpha \approxeq 0.35$ for a reference forest density of 10^{12} m^{-2} (Madec *et al.*, 2002). Basinski and Basinski (1980) show that in fcc crystals α varies from 0.5 at lowest densities to about 0.2 for the highest ones, with the densities varying from 10^{10} to 10^{14} m^{-2}. Amodeo *et al.* (2014) explain this difference between values of α for MgO and other fcc crystals by either a lack of collinear annihilations, an important ingredient in fcc metals' forest strengthening, or to be due to the higher number of slip systems per family in fcc (12 instead of 6 in MgO). Despite small deviation from the α value found in 3D–DD simulations (Amodeo *et al.*, 2014), an overall agreement between the recovered α values and the data available in literature is found. In the athermal regime, plasticity of MgO is controlled by a forest mechanism, as it is commonly observed in fcc metals. It is noticed that this behavior is significantly different from other mantle phases, for which a significantly larger lattice friction is envisaged at comparable temperatures, resulting in considerably higher stresses to obtain plastic deformation (Durinck *et al.*, 2007; Girard *et al.*, 2015; Ritterbex *et al.*, 2015; Kraych *et al.*, 2016b).

The results obtained in the low and intermediate temperature regimes prove that the 2.5D–DD approach is suitable to model plasticity of MgO. This allows to do a step further and model creep conditions by including the dislocation climb mechanism in the same simulation framework.

2.4 High temperature regime

The forest mechanism described above leads to a progressive increase of the resistance offered by the microstructure to dislocation motion, due to the increase of dislocation–dislocation interactions and dislocation density with the plastic strain. In the absence of a recovery mechanism, this process leads to the afore–mentioned work hardening behavior under constant strain rate loading or to a saturation of strain under constant load (creep mode). At temperatures high enough – *i.e.* around half of the melting temperature T_m, which for MgO is about 3100 K at ambient pressure – diffusion becomes an important phenomenon for MgO plasticity. In fact, it favors dislocation climb, a dislocation motion which involves the exchange of matter through the adsorption or emission of point defects to or from dislocation lines. Segments having edge character are here the limiting factor. Dislocation climb outside its initial glide plane helps a dislocation to bypass obstacles and possibly promote dislocation annihilation, making climb an efficient recovery mechanism. Eventually, the combination of glide and climb motions leads to a steady–state regime, where dislocation multiplication and annihilation compensate each other and dislocation density does not increase anymore with strain. In this study climb is coupled with glide in order to model creep of MgO, by evaluating the steady–state creep strain rates. Our results are compared with experimental data, given the absence of numerical results reaching large strains in this regime. Creep simulations were performed in double slip conditions, at temperatures from 1500 to 1800 K and constant applied stresses from 30 to 80 MPa.

Dislocation climb has been implemented in the code by Boioli *et al.* (2015a). Since climb motion is limited by diffusion, some insights on this process in MgO are required, in order to consider the proper input parameters for the proposed mobility law.

2.4.1 Self–diffusion coefficient evaluation

During the past decades, diffusion in periclase has been addressed both experimentally and theoretically. The latter approach suggests that interstitial magnesium and oxygen in periclase are energetically unfavorable: Hirsch and Shankland (1991a) and references therein suggest enthalpies of 12.4 and 15.2 eV for Frenkel defect formation, for Mg and O respectively. These enthalpies being rather high, interstitials concentrations in periclase are expected to be very low at equilibrium. Alfe and Gillan (2005), through Monte Carlo calculations, find values of formation enthalpy for Schottky defect in periclase around 6.7 eV, almost half of the required energy to create a Frenkel defect. Vacancy mechanism is thus expected to be dominant in periclase diffusion. Diffusion of oxygen may also be assisted by the divacancy defect, which consists in the pairing of a cationic vacancy with an oxygen vacancy (Ando *et al.*, 1983). Therefore, while defining the defect volume for diffusion, the formation of both anionic and cationic vacancies will be considered.

Van Orman and Crispin (2010) calculated the equilibrium concentration of intrinsic vacancies having a formation energy of 6.7 eV (the Schottky pair free energy of formation) and found out that the equilibrium concentration would be a few ppm at any temperature up to the melting point. It is thus likely that vacancy formation is controlled by extrinsic impurities, most notably the aliovalent, positively–charged, solutes like Fe^{3+}, Al^{3+} and Cr^{3+}. These trivalent species are contained also in ultra–high purity MgO crystals and tend to be present at higher concentrations than monovalent substitutional cations in normal crystals. Extrinsic vacancies will thus mainly have cationic character, with the concentration of extrinsic anion vacancies depending on the inverse of cationic impurities concentration. Therefore, in periclase, while it can be stated that extrinsic cationic vacancies control the Mg self–diffusion at any temperature (also in high–purity crystals) up to the melting point, the same phenomenon is not likely to happen for oxygen vacancies with respect to oxygen self–diffusion. For this reason and also due to the larger ionic radius of oxygen compared to magnesium, oxygen self–diffusion coefficients D^{sd}_{Ox} are 2 or 3 orders of magnitude smaller than those of magnesium at any investigated temperature (Van Orman and Crispin, 2010; and references therein). This implies that absorption or emission of a full MgO unit by a dislocation line is limited by the oxygen vacancy migration and formation processes, since the enthalpy required to form and migrate an oxygen vacancy is much higher than the one required for magnesium. Oxygen self–diffusion is thus the rate–limiting mechanism of diffusion in periclase and will be considered in the following as the controlling factor on dislocation climb as well.

Thus, for the implementation of diffusion in the climb mobility, the value of the self–diffusion coefficient D^{sd} is taken equal to the oxygen self–diffusion coefficient D^{sd}_{Ox}. This coefficient is expressed with the Arrhenius–type formula:

$$D^{sd} = D^{sd}_{Ox} = D_0 \exp\left(-\frac{\Delta H^{sd}}{k_B T}\right) \tag{2.8}$$

where D_0 is a pre–exponential factor and ΔH^{sd} is the activation enthalpy for oxygen self–diffusion. Here the two parameters D_0 and ΔH^{sd} are taken from experimental data. As mentioned, diffusion is a thermally activated process: this explains why the motion by climb, which is directly linked to the diffusion of point defects, plays an important role in the high temperature regime. At the same time, this process is negligible at low temperatures, where diffusion is extremely slow, and therefore does not contribute significantly to the deformation behavior. The diffusion coefficient of oxygen has been measured experimentally in a wide range of temperatures and sample compositions. Van Orman and Crispin (2010) provide a plot which summarizes most of the experimental data on oxygen diffusion in periclase at ambient pressure. Experimental values of the diffusion coefficients display an important variability: in fact, they embrace up to five orders of magnitude in the temperature range investigated experimentally, which spans from 1100 to 2500 K.

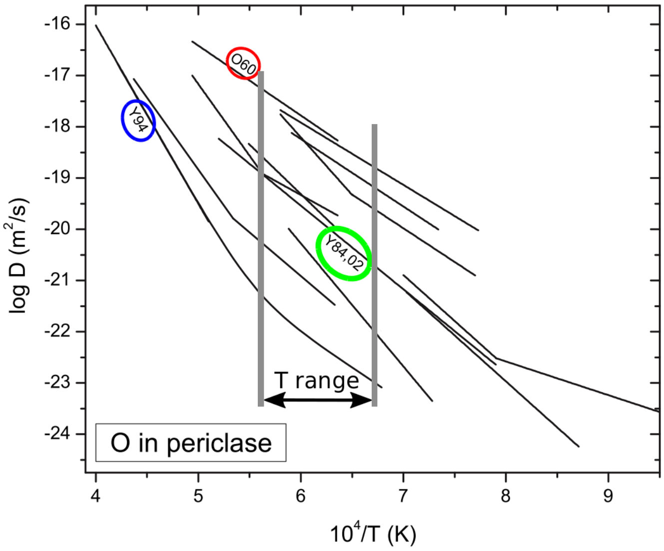

Figure 2.7: *a reproposition of Figure 1a from Van Orman and Crispin (2010), showing a compilation of oxygen self–diffusion data of MgO (black lines). It is possible to notice that, in the temperature interval considered here (marked by the grey lines),* D^{sd}_{Ox} *varies over 5 orders of magnitude. The three experimental studies considered here are: Yoo et al. (2002) (Y02), Oishi and Kingery (1960) (OK60), Yang and Flynn (1994) (YF94).*

For the present study it was chosen to run the main body of creep simulations using the oxygen self–diffusion coefficient measured by Yoo *et al.* (2002), which provides a single linear fit for a wide range of temperatures. Also, their values fall roughly in the middle of the variability range of experimental measurements. To evaluate the influence of D^{sd}_{Ox} on the simulated creep strain rates, tests were made using also the extreme experimental values measured so far. The parameters and temperature ranges at which they were obtained are shown in Table 2.2.

Oishi and Kingery (1960) provide the upper bound value, using samples containing impurities. The inferred mechanism driving oxygen diffusion was assumed to be impurity–

D_0 (m^2/s)	ΔH^{sd} (m^2/s)	T range (K)	D_{Ox}^{sd} (m^2/s) at 1700 K	Reference
$2.5 \cdot 10^{-10}$	2.71	1570–2020	$2.7 \cdot 10^{-18}$	OK60
$1.8 \cdot 10^{-10}$	3.24	1270–1920	$5.2 \cdot 10^{-20}$	Y02
$1.0 \cdot 10^{-14}$	2.66	1450–1700	$1.5 \cdot 10^{-22}$	YF94
$7.6 \cdot 10^{-3}$	6.91	1700–2400		

Table 2.2: *experimental values of self–diffusion pre–exponential factor D_0 and activation enthalpy ΔH^{sd} to compute oxygen self–diffusion coefficient D_{Ox}^{sd}. The main body of simulations was run using the value provided by Yoo et al. (2002) (Y02) while a test was made using also the other extreme values at 1700 K, from Oishi and Kingery (1960) (OK60) and Yang and Flynn (1994) (YF94). The calculated numerical values of D_{Ox}^{sd} are also shown. Data from Yang and Flynn (1994) are shown for both the high and low temperature regimes and only the latter values are employed in the model.*

controlled or a structure–sensitive process, with the activation energy corresponding to ion mobility. On the other end, Yang and Flynn (1994) measured diffusion coefficients on MgO crystals having an ultra–high degree of purity and obtained the smallest values of oxygen self–diffusion coefficients ever observed experimentally (Figure 2.7). At high temperatures they find an activation energy of 6.9 eV for oxygen diffusion, a value consistent with the activation enthalpy for intrinsic diffusion. However, at lower temperatures, diffusion becomes less activated with a slope resembling that of other studies, with an activation energy of 2.66 eV. This latter value has been chosen, since the range of temperatures investigated in this study falls within this deviation from intrinsic behavior. The temperature at which the data gathered from these studies overlap is around 1700 K, therefore this value was set for simulations addressing the variability of creep strain rates with respect to the chosen oxygen self–diffusion coefficient, D_{Ox}^{sd}. These variations on the creep strain rates are here displayed and the obtained results are put in perspective with respect to creep data obtained in experiments.

2.4.2 Climb mobility law

Assuming steady–state conditions, the flux of vacancies from and to the dislocation line is calculated by solving the diffusion equation showed in equation 2.8, allowing for the analytical expression of climb velocity (Hirth and Lothe, 1982; Caillard and Martin, 2003):

$$v_c = \kappa \frac{D_{Ox}^{sd}}{b} \left[\exp\left(\frac{\tau_c \Omega}{k_B T} \right) - \frac{c_\infty}{c_0} \right] \tag{2.9}$$

where D_{Ox}^{sd} is the oxygen self–diffusion coefficient described above and κ is a geometrical factor which depends on the geometry of the flux field. $\Omega = 18.7$ Å^3 is the vacancy formation volume for self–diffusion, which is here considered to be equal to the formation volume of Mg and O vacancies and is calculated from the unit cell volume of periclase – *i.e.* $\Omega = a^3/Z$, where $Z = 4$ is the number of formula units per unit cell. τ_c is the effective stress resolved in the climb direction, that is, perpendicular to the glide directions of the two simulated slip systems and is taken positive (negative) if it favors vacancy emission (adsorption). c_∞ is the vacancy concentration far from the dislocation lines (*i.e.* far from the sources and sinks of vacancies) and c_0 is the intrinsic equilibrium vacancy concentration at a given temperature. In particular, $c_0 = \exp(\Delta G_f / k_B T)$, where ΔG_f is the intrinsic vacancy formation energy (*cf.* equation 1.1). We assume that far from the dislocations, the vacancy concentration is constant and equal to the intrinsic equilibrium concentration – *i.e.* $c_\infty = c_0$ (Boioli *et al.*, 2015a;b). Ω is extremely small (being expressed in cubic Å) therefore the term $[\exp(\tau_c \Omega / k_B T) - 1] \simeq \tau_c \Omega / k_B T$. Thus, for this case, $v_c \propto \tau_c$ (*cf.* the explanation below equation 1.8). It is also assumed that the dislocation line is saturated with jogs. This means that point defects are instantaneously adsorbed or emitted by dislocation lines. This latter assumption implies a cylindrical flux around the dislocation, identified by $\kappa = 2\pi / \ln(R/r_c)$ where R and r_c represent the two radii of the cylindrical surfaces through which the vacancy flux is calculated. r_c is the core radius and R is taken as a fraction of the average dislocation distance. Being within the logarithmic term, the R/r_c ratio does not significantly affect the climb velocity values and here is taken constant and equal to 100 (Boioli *et al.*, 2015a;b).

2.4.3 Results

Creep simulations were run to model plasticity of MgO at high temperatures (over 0.5 T_m), where motion by climb is included. Creep results at 1600 K are shown in Figure 2.8a, which displays the curves of strain as a function of time obtained from simulations run with (red curve), and without (green curve), including climb motion. After the initial transient stage, glide alone is not capable of producing further deformation: in fact, once the quasi–equilibrium condition is reached, dislocations are trapped into local minimum energy configurations and do not glide anymore under the applied stress (which is constant in creep mode). The introduction of climb renders possible for the dislocation lines to move outside their glide planes and further interact, releasing the microstructure and leading to a dynamical equilibrium condition.

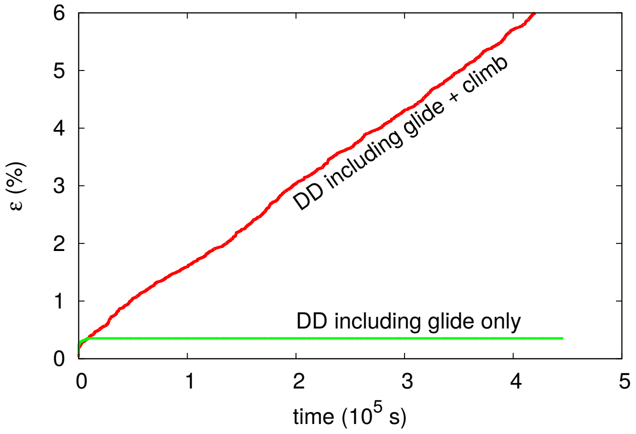

(a)

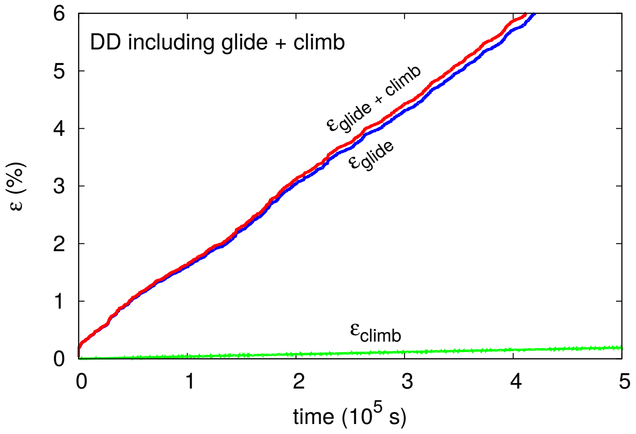

(b)

Figure 2.8: *strain ε as a function of time for two simulations run at 1600 K with constant applied load σ of 60 MPa with (red curve) and without (green curve) including dislocation climb mechanism (a). (b): strain ε as a function of time for a simulation run at 1600 K with constant applied load σ of 60 MPa including dislocation climb mechanism. Red curve: total strain as a function of time, where both glide and climb are included. $\varepsilon_{glide+climb}$ is compared with its components due to dislocation glide (ε_{glide}, blue curve) and climb (ε_{climb}, green curve).*

In Figure 2.8b are shown the different contributions to strain in a creep simulation where both glide and climb are included. The strain produced by dislocations moving in their glide plane (blue curve) is significantly larger than the strain produced by dislocations moving outside their glide plane (green curve). The total strain as a function of time is also shown (red curve, same as the one in Figure 2.8a). It is noted, therefore, that even if climb is included, strain is mostly due to dislocations moving by glide.

In principle, climb allows dislocations to escape from their glide planes and to be released from “jammed” configurations to eventually bypass obstacles or annihilate. The dislocation microstructure is therefore relaxed and other dislocations are free to move by glide until a new “jammed” state is reached. The repetition of this process leads to the steady–state creep regime, characterized by a constant deformation rate for a given load. This is verified by the linear increase of strain with time that can be observed from the red curves of Figures 2.8a and 2.8b.

Figure 2.9a demonstrates that the steady–state condition is observed for different values of applied stress, with the strain varying linearly with respect to time for all the curves obtained. The steady–state condition is confirmed also from the evolution of the dislocation density with time, shown in Figure 2.9b, where, after the initial transient, the density fluctuates around a constant value for all the considered cases. At a given temperature, the equilibrium density values increase with increasing stress, since the higher the latter, the easier it is to unzip the junctions and let more dislocations to glide, produce strain and multiply. These observations confirm that multiplication and annihilation are acting simultaneously during simulations, counterbalancing each other. The former mechanism is related to strain production, which in turn results to be originated by glide motion (Figure 2.8b); while the latter is triggered by dislocations getting untangled through climb to other planes, in order to further interact and eventually annihilate, decreasing the dislocation density.

This study shows that the interplay between glide and climb mechanisms leads to the steady–state creep behavior observed in experiments. The steady–state creep strain rates depend exponentially on the temperature, therefore the following Arrhenius–type

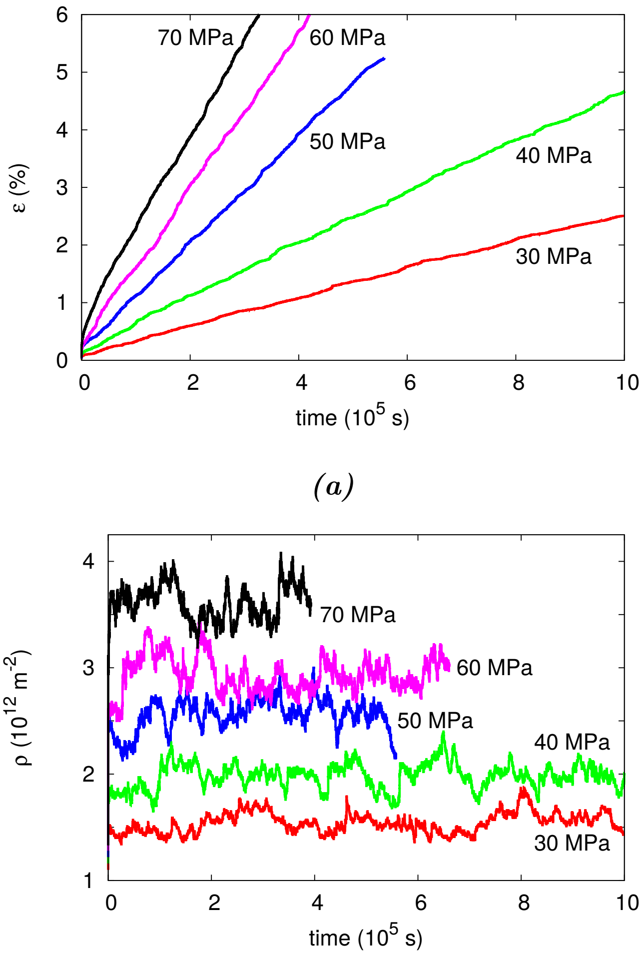

(a)

(b)

Figure 2.9: *(a) strain ε as a function of time for simulations run at 1600 K with applied loads σ from 30 to 70 MPa. Steady-state condition is reached. (b): Dislocation density ρ as a function of time for the same curves of (a). The steady–state condition is highlighted by the fact the all ρ curves oscillate around a constant value.*

equation is commonly used to describe high temperature deformation:

$$\dot{\varepsilon} = \dot{\varepsilon_0}\sigma^n \exp\left(-\frac{Q}{k_B T}\right) \tag{1.8}$$

where Q, n and $\dot{\varepsilon_0}$ are generally assumed to be constant and to depend on the mechanism controlling the plastic creep behavior. σ here and from now on is the constant applied stress. Variables like substitutional iron content and oxygen partial pressure could be exotic mechanisms that influence the power law creep but this does not appear to be the case for MgO (Wolfenstine and Kohlstedt, 1988).

Our creep results are presented in Figure 2.10.

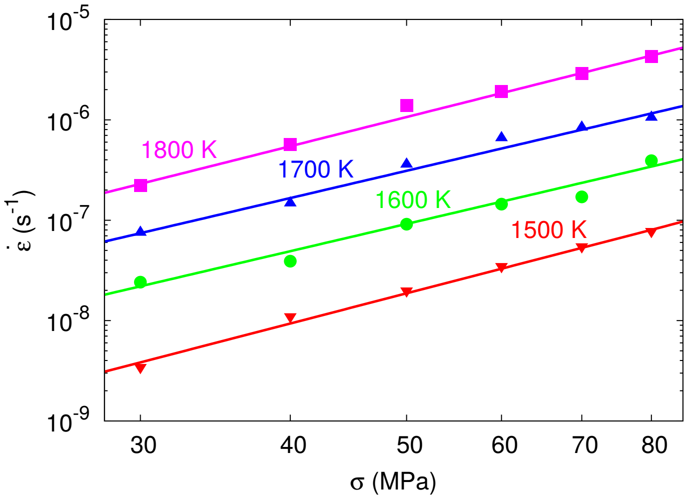

(a)

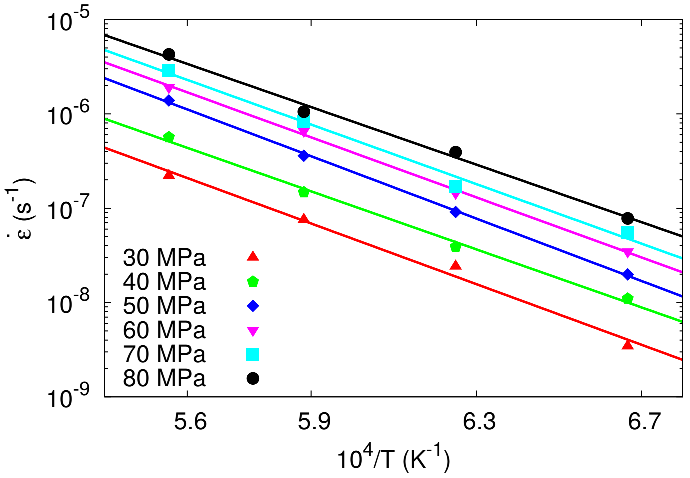

(b)

Figure 2.10: *(a) creep strain rates $\dot{\varepsilon}$ as a function of the applied creep stress σ for the different tested temperatures. Color lines represent the fitting of the data. (b): Variation of the creep strain rates $\dot{\varepsilon}$ as a function of the reciprocal temperature for all the applied stresses. Color lines represent the fitting of the data.*

The investigated temperatures span from 1500 to 1800 K and the applied creep stresses σ from 30 to 80 MPa. Figure 2.10a shows the creep strain rates obtained from the 2.5D–DD simulations as a function of the creep stress, for all tested temperatures. A constant slope is found for these strain rate–stress curves at any temperature. The derivative of the logarithm of creep strain rate with respect to the logarithm of creep stress gives the value of the power law stress exponent, n. All the measurements of n fall within the respective errors with an overall average value of 2.9(2).

Figure 2.10b shows the creep strain rates as a function of the reciprocal temperature, for all the tested creep stresses. The activation enthalpy for creep Q can be obtained from the slope of the derivative of strain rate logarithm with respect to the reciprocal temperature. It is obtained a constant value of 3.1(2) eV for Q.

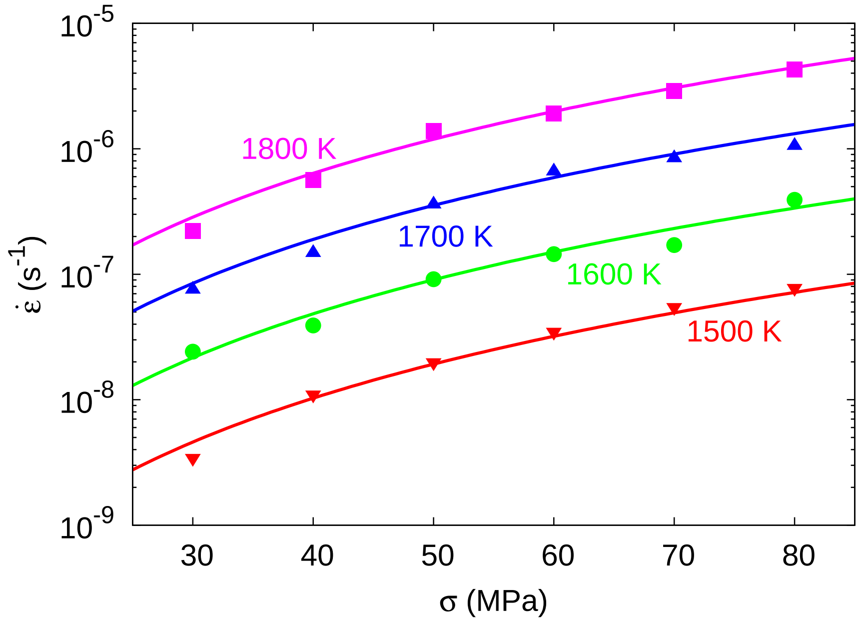

Figure 2.11: *Creep strain rates $\dot{\varepsilon}$ as a function of applied stress σ. Color lines represent the power law curves plotted for the different temperatures using the power law parameters obtained from previous fitting procedures.*

Knowing the values of n and Q it is possible to fit also the third parameter of the power law, $\dot{\varepsilon_0}$. In Figure 2.11 the here obtained data are presented together with the respective power law equations, which are plotted using the three averaged parameters n, Q and $\dot{\varepsilon_0}$ at different temperatures.

2.4.4 Discussion

Creep results are discussed starting from the retrieved power law parameters. The stress exponent is often considered as an indicator of the controlling mechanisms acting during creep deformation. In fact, diffusion creep results in a linear dependence between stress and strain rates, while dislocation creep is commonly identified by a stress exponent between 3 and 5. In this study, we find a constant stress exponent close to 3 for the considered temperature and applied stress range. Several theoretical models predict the same exponent (*cf.* Section 1.3.1).

The value of creep activation enthalpy Q obtained from these calculations is 3.1(2) eV, close to the oxygen self–diffusion enthalpy from Yoo *et al.* (2002) – *i.e.* 3.24 eV – that was used as input parameter in equation 2.9 for all the simulations displayed in Figures 2.10a,b and 2.11. Experimentally, it is recognized that for metals the activation energies of creep agree with the ones of self–diffusion of the slowest species (Langdon and Pask, 1970), while for oxides and silicates such a correlation is not completely clear. Here it is found the same agreement, demonstrating that climb is the limiting mechanism in high temperature creep of MgO. This is not surprising, since the climb mobility is several orders of magnitude (10 to 13 depending on the considered creep stresses and temperatures) slower than the glide one.

A compilation of experimental values for n and Q is provided in Table 2.3.

Type of test	Sample	T range (K)	n	Q (eV)	Reference
3–pt bend	SC	1723–1973	4.0–7.0	3.5–7.0	Cummerow (1963)
3–pt bend	SC	1573–1903	3.0	5.8	Rothwell and Neiman (1965)
Compression	SC	1333–1773		4.8	Atkins and Tabor (1967)
Tension	SC	1473–1773	3.8–4.5	4.1	Clauer and Wilcox (1976)
Compression	PC	1573–1733	3.2	3.3	Bilde-Sörensen (1972)
Compression	PC	1473–1773	2.6	4.6, 4.8	Hensler and Cullen (1968)
Compression	PC	1473	3.3	2.2	Langdon and Pask (1970)
Compression	SC	1573–1773	3.4	4.6	Wolfenstine and Kohlstedt (1988)
Compression	SC	1950–2000	3.0, 1.3		Ramesh *et al.* (1986)
Compression	SC	1673–2073	4.2–8.5	3.6–4.4	Routbort (1979)

Table 2.3: *high temperature creep power law parameters obtained from experiments on MgO. SC and PC refer to single crystal and polycrystalline samples respectively.*

First, it is worth pointing out that experimental conditions may vary substantially, making the comparison more difficult. Nevertheless, concerning the power law exponent, the values found in experiments generally agree with the ones proposed by predictive models. A deviation of n towards higher values is observed at lower temperatures by Cummerow (1963) and Routbort (1979). In the latter case, this may be due to the presence of precipitates in some MgO samples, which would influence the creep behavior, while in the former case the deviation could be due to the fact that other extrinsic processes may become more important at lower temperatures, widening the variability range of n. These impurity–related interactions are not taken into account in the present formulation, since it reproduces deformation in MgO single crystals where the role of impurities appears only through the point defect concentration introduced in the pre–exponential factor of the diffusion equation. Thus, in this study, the value of the power law exponent represents a lower limit of the predicted variability.

The activation enthalpy of creep gathered from experiments, on the other hand, often mirrors the one of oxygen self–diffusion in MgO. This is in agreement with our study. A slightly higher activation enthalpy in some cases is found and an interpretation of this difference is provided by Wolfenstine and Kohlstedt (1988). They propose that this energy difference could be due to jog formation enthalpy, which in climb–controlled creep may be an important factor, estimated at 1.2 eV. The remaining portion of creep activation enthalpy equals the one of oxygen self–diffusion, which agrees with the results reported in this chapter. In our formulation the jog formation energy is not included, since it is assumed that the dislocation lines are saturated with jogs. This provides an explanation of the difference we observe between our data and some experimental creep activation enthalpy values.

The influence of oxygen self–diffusion coefficients on strain rates at 1700 K is displayed in Figure 2.12a. The variability of four orders of magnitude between the extreme values of the diffusion coefficients (cf. Table 2.2) is reduced to three orders of magnitude of difference for the resulting creep strain rates.

To better compare the here obtained results with the experimental data on creep in MgO, another point of discussion must be addressed. The lowermost self–diffusion values obtained by Yang and Flynn (1994) result from diffusion measurements performed on crystals having an exceptional degree of purity. These crystals do not show any significant impurity content and the surface damage contribution to diffusion is dramatically reduced. Such features contribute to lower the active impurity level during diffusion by a factor of ten below the one of high–quality commercial MgO Yang and Flynn (1996). Moreover, there is no evidence in the bibliography cited in Table 2.3 that the samples used in creep experiments were somehow resembling the ones of Yang and Flynn (1994) in terms of crystal growing technique, impurity content and surface damage extent. Therefore, the latter samples are not considered representative with respect to the diffusion mechanism acting in the ones subjected to creep experiments. The input parameters for self–diffusion from those experimental results controlled by extrinsic oxygen diffusion – i.e. Oishi and Kingery (1960) and Yoo *et al.* (2002) – better resemble the quality and conditions of experimental crystals being subjected to creep. Considering these last values, it is possible to focus on the upper half of the graph of Figure 2.12a to draw a better comparison with experimental data. This is shown in Figure 2.12b, where, at these conditions, the strain rates obtained in this study bracket the experimental results for MgO.

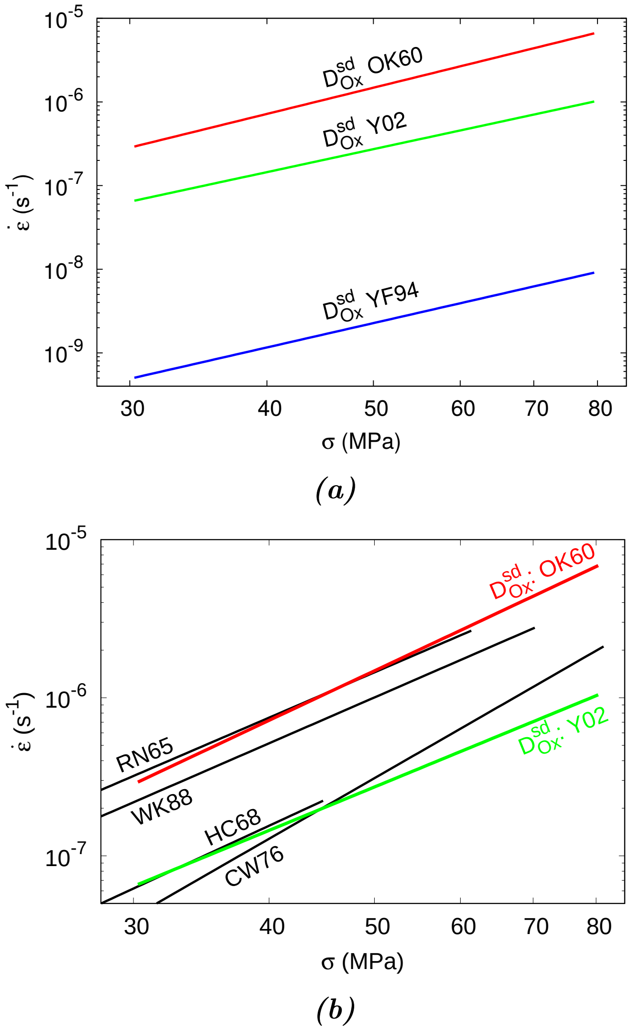

(a)

(b)

Figure 2.12: *(a) creep strain rates $\dot{\varepsilon}$ as a function of stress σ (color lines) at 1700 K using different oxygen self–diffusion coefficients as input parameters for the 2.5D–DD code. OK60: Oishi and Kingery (1960), Y02: Yoo et al. (2002), YF94: Yang and Flynn (1994). Numerical values for D_{Ox}^{sd} at 1700 K are provided in Table 2.2. (b): Creep strain rates $\dot{\varepsilon}$ as a function of stress σ (color lines) compared with experimental data (black lines). RN65: Rothwell and Neiman (1965), HC68: Hensler and Cullen (1968), CW76: Clauer and Wilcox (1976), WF88: Wolfenstine and Kohlstedt (1988).*

In conclusion: in the present chapter we developed a specific 2.5D–DD approach to MgO for the first time, in order to reproduce its deformation under three different temperature regimes. At low and intermediate temperatures, the obtained results agree with previous numerical (3D–DD) and experimental evidences, providing a benchmark of the presented formulation. This permitted to do a step further and introduce dislocation climb at high temperatures, where this mechanism has a relevant role on creep of MgO crystals. Results in this regime mirror the available experimental data on high temperature creep of MgO, confirming that the present numerical tool is capable of reproducing the plastic behavior of this phase and capturing the relevant mechanisms driving its deformation under varying conditions.

In the next chapter, the present technique is developed and adapted to lowermost mantle conditions.

Chapter 3

Modeling viscosity of (Mg,Fe)O at lowermost mantle conditions

In this chapter[1] we focus on the creep behavior of (Mg,Fe)O at the bottom of the lower mantle, where the presence of thermo–chemical anomalies such as ultralow–velocity zones (ULVZ) may significantly alter the viscosity contrast characterizing this region. Two different iron concentrations of $(\mathrm{Mg}_{1-x}\mathrm{Fe}_x)\mathrm{O}$ are considered: one mirroring the average composition of ferropericlase throughout most of the lower mantle ($x = 0.20$) and another representing a candidate magnesiowüstite component of ULVZs near the base of the mantle ($x = 0.84$). The investigated pressure–temperature conditions span from 120 GPa and 2800 K, corresponding to the average geotherm at this depth, to core–mantle boundary conditions of 135 GPa and 3800 K.

In this chapter, dislocation creep of (Mg,Fe)O is investigated by dislocation dynamics (DD) simulations, a modeling tool which considers the collective motion and interactions of dislocations. To model their behavior, a 2.5 dimensional dislocation dynamics approach is employed. Within this method, both glide and climb mechanisms can be taken into account, and the interplay of these features results in a steady–state condition. This allows the retrieval of the creep strain rates at different temperatures, pressures, applied stresses and iron concentrations across the (Mg,Fe)O solid solution, providing information on the viscosity for these materials.

A particularly low viscosity is obtained for magnesiowüstite with respect to ferroper-

---

[1] The present chapter is based on the following manuscript: Reali, R., Jackson, J.M., Van Orman, J., Bower, D.J., Carrez, P., and Cordier, P. Modeling viscosity of (Mg,Fe)O at lowermost mantle conditions. *Physics of the Earth and Planetary Interiors*, 2018 (*submitted*).

iclase, the difference being around 10 orders of magnitude. Thus, the final section of this chapter is devoted to the assessment of the dynamic implications of such a weak phase within ULVZs, in terms of the viscosity contrast with respect to the surrounding lowermost mantle.

Keywords: (Mg,Fe)O; 2.5D dislocation dynamics; viscosity; core–mantle boundary; ultralow–velocity zones

3.1 The core–mantle boundary

The Earth's core–mantle boundary (CMB) is a major thermochemical boundary layer within the Earth, exerting a primary influence on the evolution of the planet. Seismic observations indicate a significant complexity in this boundary region, including structures of varying length scales and velocity perturbations. In particular, patches near the CMB have been identified, ranging from a few to tens of km thick and ~100 km across, in which the seismic wave velocities are reduced by about 5 to 30% (*e.g.* Garnero and Helmberger, 1995; Revenaugh and Meyer, 1997; Rost *et al.*, 2006; Hutko *et al.*, 2009; Rost, 2013; Sun *et al.*, 2013; Thorne *et al.*, 2013; Gassner *et al.*, 2015; Frost *et al.*, 2018; Zhang *et al.*, 2018; Yu and Garnero, 2018; for a recent review). These ultralow–velocity zones (ULVZs) have been interpreted as aggregates of partially molten material or as solid, iron–enriched assemblages, typically based on proposed sources of velocity reduction (Knittle and Jeanloz, 1991; Williams and Garnero, 1996; Mao *et al.*, 2004a; Labrosse *et al.*, 2007; Sakai *et al.*, 2010; Wicks *et al.*, 2010; Dorfman and Duffy, 2014; Muir and Brodholt, 2015; Liu *et al.*, 2017).

It is suggested that more extreme chemical heterogeneity, such as Fe–rich (Mg,Fe)O or magnesiowüstite residuum from large–scale melting events in Earth's history (Labrosse *et al.*, 2007) may be at least partially responsible for explaining ULVZs (Wicks *et al.*, 2010; Bower *et al.*, 2011; Muir and Brodholt, 2015; Wicks *et al.*, 2017). Interpretation of these features and the dynamic processes that shape them requires knowledge of their rheological properties. In particular, Bower *et al.* (2011) presented a geodynamic and mineral physics model of a solid–state ULVZ by exploring the steady–state morphology of a magnesiowüstite–bearing layer at the base of the mantle. Implemented as a chemical density anomaly defined by variable proportions of magnesiowüstite co–existing with bridgmanite, the layer was relatively well constrained in terms of its equation of state. However, one of the least constrained variables in dynamic modeling is the viscosity of the system. In Bower *et al.* (2011), the viscosity of the system was prescribed only as a function of temperature. While recent progress has been made in estimating the rheological properties of MgO and magnesium–rich (Mg,Fe)O under lower mantle conditions (*e.g.* Yamazaki and Karato, 2001; Van Orman *et al.*, 2003; Lin *et al.*, 2009; Cordier *et al.*, 2012; Marquardt and Miyagi, 2015; Deng and Lee, 2017; Immoor *et al.*, 2018), no such studies exist for magnesiowüstite.

In this chapter, we apply the recent development of numerical modeling of dislocation creep based on 2.5D dislocation dynamics to the rheology of iron–rich (Mg,Fe)O magnesiowüstite at the PT conditions of the CMB. Since high–temperature creep significantly depends on diffusion, we first present a critical assessment and evaluation of this parameter for (Mg,Fe)O under the conditions of the CMB. Then dislocation dynamics simulations of creep are performed. Using our results of strain rates as a function of the applied stresses, we obtain the effective viscosity of magnesiowüstite. For comparison, we also perform these simulations for ferropericlase. Our results point to very low values of viscosity for magnesiowüstite. These findings motivate the final section of this paper, where we assess the influence of low viscosity magnesiowüstite on the dynamics of the lowermost mantle by re–visiting the framework presented in Bower *et al.* (2011).

3.2 Method

For this study, it is going to be employed the same approach described in Chapter 2, where the 2.5D–DD simulation technique was benchmarked for MgO at ambient conditions with respect to experimental and other numerical data, demonstrating its validity in a variety of thermal regimes. In fact, being first developed to model creep in aluminum (Keralavarma *et al.*, 2012) and then applied to olivine (Boioli *et al.*, 2015a;b) and MgO (Reali *et al.*, 2017), it represents a viable instrument to model creep of (Mg,Fe)O at high pressures and temperatures.

Here we focus on the high temperature regime (*i.e.*, from approximately half of the melting temperature of (Mg,Fe)O, *cf.* Section 2.4) at lowermost mantle conditions. In this regime, temperatures are high enough to favor diffusion and consequently render dislocation climb, which is diffusion–dependent, a viable recovery mechanism, instaurating the interplay between glide and climb mobility which underlies high temperature, high pressure creep.

3.2.1 Material properties

Throughout most of the lower mantle, the magnesium–iron oxide in equilibrium with calcium silicate perovskite and bridgmanite is thought to be magnesium–rich (Mg,Fe)O ferropericlase, which exhibits the B1 rock–salt structure with space group $Fm\bar{3}m$. Ferrous iron in ferropericlase undergoes a gradual spin pairing transition, which is completed by the PT conditions of the base of the mantle (Sturhahn *et al.*, 2005; Tsuchiya *et al.*, 2006). In addition to the temperature dependence, the pressure of the spin pairing transition, as well as the width (pressure range), increases with increasing iron concentration (*e.g.* Solomatova *et al.*, 2016). Although studies indicate that the iron cations in iron–rich (Mg,Fe)O begin to pair at pressures of around 120 GPa and 300 K (*e.g.* Speziale *et al.*, 2005; Wicks *et al.*, 2010; Fischer *et al.*, 2011; Ozawa *et al.*, 2011), the presence of magnesium widens the pressure–temperature stability field of the B1 structure compared to FeO (Wicks *et al.*, 2015). Thus, thermal effects and the presence of a small amount of magnesium would likely prohibit a spin crossover in iron–rich (Mg,Fe)O at CMB conditions. Therefore, in this study, we consider high–spin magnesiowüstite $(\mathrm{Mg_{0.16}Fe_{0.84}})\mathrm{O}$ and low–spin ferropericlase $(\mathrm{Mg_{0.80}Fe_{0.20}})\mathrm{O}$ to represent possible end–member cases of (Mg,Fe)O at lowermost mantle conditions. For these compositions, and for a sake of comparison, we consider two PT conditions: one resembling the geotherm at 120 GPa and 2800 K and the other representing CMB conditions suitable for solid–state ULVZs, at 135 GPa and 3800 K. Additionally, in order to have a first estimate of the creep activation enthalpy for magnesiowüstite at CMB conditions, another set of calculations was run at 135 GPa and 3200 K.

The elastic properties for high–spin magnesiowüstite are taken from experimental results of Wicks *et al.* (2015; 2017), which constrained the thermal equation of state and shear elastic properties for this phase under lowermost mantle conditions using powder X–ray diffraction and inelastic X–ray scattering techniques. The elastic properties for low–spin ferropericlase are taken from a theoretical study that investigated the thermoelastic effects related to the spin crossover up to pressures of 130 GPa and 4000 K (Wu and Wentzcovitch, 2014). We provide the elastic properties used for these two end–member cases along with their lattice constant and burgers vector magnitude in Table 3.1[2].

	$(Mg_{0.16}Fe_{0.84})O^a$			$(Mg_{0.80}Fe_{0.20})O^b$	
	120 GPa 2800 K	135 GPa 3200 K	135 GPa 3800 K	120 GPa 2800 K	135 GPa 3800 K
Lattice constant a (Å)	3.83	3.81	3.82	3.86	3.87
Burgers vector b (Å)	2.71	2.69	2.70	2.73	2.74
Density (g/cm^3)	7.90	8.03	7.97	5.38	5.36
V_S (km/s)	3.50	3.52	3.47	7.16	7.09
V_P (km/s)	8.20	8.19	8.14	13.58	13.79
Poisson ratio ν	0.39	0.39	0.39	0.31	0.32
Shear modulus μ (GPa)	97	100	96	276	270
Bulk modulus (GPa)	402	406	401	625	660
Liquidus^c (K)	4300	4440	4440	7220	7410

Table 3.1: *lattice constant, $1/2\langle 110\rangle$ Burgers vector magnitude, elastic properties and estimated liquidus temperatures for $(Mg_{0.16}Fe_{0.84})O$ magnesiowüstite and $(Mg_{0.80}Fe_{0.20})O$ ferropericlase at the pressure and temperature conditions of interest. ^{a}Wicks et al. (2015; 2017), ^{b}Wu and Wentzcovitch (2014) extrapolated to 135 GPa, ^{c}Values are taken as a linear interpolation between the melting points of MgO and FeO (Cohen and Weitz, 1998; Fat'yanov and Asimow, 2014; Fischer and Campbell, 2010). See text for details.*

3.2.2 2.5D–DD set–up

In our simulations, 200 to 400 dislocations having Burgers vectors $b = 1/2\langle 110\rangle$ are introduced in a simulation cell having edges of ~10–60 μm. These dislocations are allowed to glide in two slip systems belonging to the $1/2\langle 110\rangle\{110\}$ slip family. It has been shown (Amodeo *et al.*, 2012) that around 30 GPa $1/2\langle 110\rangle\{100\}$ becomes an easier slip family. However, at temperatures high enough (2600–2800 K), the athermal regime is reached even at CMB conditions and glide does not depend anymore on lattice friction. This renders negligible the difference in CRSS observed for the two slip families and therefore,

---

[2] The evaluation of the lattice constant and elastic parameters of the considered phases was performed by J.M. Jackson

consistently with Chapter 2, slip systems belonging to $1/2\langle 110\rangle\{110\}$ are here considered.

The simulation cell is a square of size $L_x = L_y$ and dislocation lines are introduced as straight segments of constant length $L = 1$ μm perpendicular to the reference plane, where both glide and climb directions lie (*cf.* Figure 2.3). All dislocation lines have edge character, which is the limiting feature concerning dislocation climb.

For all the tested PT conditions, a constant creep stress σ ranging from 10 to 50 MPa was applied to the simulated system. Furthermore, in the case of $(\mathrm{Mg}_{0.8}\mathrm{Fe}_{0.2})\mathrm{O}$ ferropericlase, some tests were run also at higher stresses, up to 500 MPa, in order to better anchor the fit for the strain rate as a function of stress. In fact, since climb in $(\mathrm{Mg}_{0.8}\mathrm{Fe}_{0.2})\mathrm{O}$ ferropericlase is very slow for many of the considered PT conditions, it was possible to achieve a minimum acceptable strain of around ~1% in practical times only by raising the applied stress. At steady–state, the equilibrium dislocation density, equal to the number of dislocations in the system divided by its area, rises with the applied, constant creep stress. Therefore, the cell size was adjusted in order to have a representative and comparable number of dislocations at the equilibrium for all the tested stresses. Equilibrium dislocation densities, here, vary between 10^{11} and 10^{13} m^{-2}, requiring cell dimensions $L_x = L_y$ from 8 to 60 μm.

The glide and climb mobilities are the same described in equations 2.5 and 2.9, respectively. In the case of climb velocity, the formation volume for vacancies Ω will change accordingly to the considered PT conditions (*cf.* Table 3.1). Also, the self–diffusion coefficient needs to be evaluated at CMB conditions and the next section is devoted to this estimate. Finally, the junction formation as well as dislocation multiplication and annihilation mechanisms bear the same parametrisation.

3.3 Evaluation of HP and HT self–diffusion coefficients

Self–diffusion of MgO has been extensively studied over the past decades, for both the cation and anion sublattices. However, a full description of this phenomenon as a function of pressure, temperature and composition for lowermost mantle conditions is lacking. Therefore, it is necessary to develop a method to conveniently estimate diffusion coefficients to be introduced into the 2.5D dislocation dynamics model.

Concerning the magnesium sublattice in periclase, it can be stated that extrinsic cation vacancies control Mg self–diffusion at any temperature up to the melting point. This is because aliovalent positively charged solutes like Fe^{3+}, Al^{3+} and Cr^{3+} tend to be present at concentrations much higher than the intrinsic vacancy concentrations, even in nominally pure synthetic crystals. The presence of aliovalent solutes leads to the formation of cation vacancies, to maintain charge balance, and hinders the formation of oxygen vacancies, which also have a net positive charge. For this reason, oxygen self–diffusion coefficients are at least 2 to 3 orders of magnitude smaller than those of magnesium at any investigated temperature (Van Orman and Crispin, 2010; and references therein). Oxygen self–diffusion D^{sd}_{Ox} is thus considered as the rate–limiting mechanism for dislocation climb (cf. Section 2.4.1).

3.3.1 The homologous temperature relation

A review of the literature on oxygen self–diffusion coefficients in MgO at ambient conditions (Van Orman and Crispin, 2010) shows that at high temperatures an activation energy resembling that of the intrinsic regime is observed in some cases, while a phenomenon with smaller temperature dependence is often observed at lower temperatures. Self–diffusion in the latter case appears to be strongly influenced by structural defects, but not by chemical impurities (*e.g.* Yang and Flynn, 1994; 1996), and is consistent with fast transport along dislocation cores (Van Orman and Crispin, 2010).

Although fast transport via dislocations may have an important role in the bulk diffusivity of oxygen in both experimental and natural samples, this process is not the controlling factor of dislocation climb in the present formulation. The latter refers to the net flux of vacancies from and to the dislocation line across a cylindrical surface, which excludes the core–related effects and therefore does not consider the aforementioned, structure–sensitive factors affecting diffusion (*cf.* the definition of the geometrical parameter κ in the climb velocity law, equation 2.9). Therefore, the starting point for the evaluation of diffusion at lower mantle conditions is the assumption that oxygen diffusion is intrinsic.

Experimental measurements indicate that oxygen diffusion coefficients are insensitive to the concentration of aliovalent dopants, either in the intrinsic regime (Yang and Flynn, 1994; 1996) or in the extrinsic regime controlled by structural defects (Ando *et al.*, 1983).

At high temperatures, as mentioned before, higher activation enthalpies for diffusion are generally observed (Oishi *et al.*, 1983; Yang and Flynn, 1994; 1996). In particular, Yang and Flynn (1994) found an activation enthalpy in good agreement with the theoretical value for intrinsic oxygen diffusion. Furthermore, the absolute values of the diffusion coefficients determined experimentally by these authors were found to be in good agreement with the theoretical values. As it provides strong experimental evidence for intrinsic diffusion, Yang and Flynn (1994) will be considered as a benchmark at ambient conditions for the calculated high pressure, high temperature diffusion coefficients.

Intrinsic diffusion in MgO under lower mantle conditions was calculated by Ita and Cohen (1997), who used molecular dynamics simulations and found that oxygen–magnesium vacancy pairs would predominate over isolated oxygen vacancies (Schottky defects) at low temperatures, while the opposite was found for temperatures exceeding 1000 K. Nevertheless, we expect small differences between the cases where oxygen diffusion occurs through isolated oxygen vacancies or vacancy pairs, as discussed by Yang and Flynn (1994). In fact, values yielded by Ita and Cohen (1997) are in close agreement with the ones of Yang and Flynn (1994).

Ita and Cohen (1997) also found that the homologous temperature relation works well to describe intrinsic diffusion in MgO:

$$D_{Ox}^{sd} = D_0 \exp\left(-\frac{gT_m}{T}\right) \tag{3.1}$$

where T_m is the melting temperature and D_0 and g are empirical constants. This relation also describes the pressure dependence of diffusivity in crystalline metals, as Reaman *et al.* (2012) showed using diamond anvil cell experiments at pressures up to about 70 GPa. As shown below, the homologous temperature relation also provides a remarkably good description of intrinsic anion diffusion in ionic crystals, with anion diffusion data for a wide range of crystals having the rock salt structure all following a common homologous temperature scaling.

As noted above, aliovalent impurities, including trace levels of iron, have no influence on oxygen diffusion in MgO. However, iron in (Mg,Fe)O has a strong influence on the bond strength, influencing dramatically the melting temperature and, according to the homologous temperature relation, the oxygen diffusion coefficient. Here, we use the homologous temperature relation to fit anion diffusion data for MgO and other rock–salt structured ionic crystals. This is done in order to calculate the oxygen diffusion coefficients of (Mg,Fe)O as a function of composition, pressure and temperature. To use this relation for (Mg,Fe)O, it is necessary to estimate reasonable values of T_m for magnesiowüstite and ferropericlase (*cf.* Table 3.1). For a solid solution there is no single value of T_m at a given pressure, and in particular there is a wide gap between the solidus and liquidus curves for (Mg,Fe)O (Wu *et al.*, 1993; Zhang and Fei, 2008). Our estimates for the values of T_m to be used in the homologous temperature relation were calculated as follows.

3.3.2 Melting and homologous temperature scaling

First, we use the melting curve of MgO computed by Cohen and Weitz (1998) up to 100 GPa, because it was determined self–consistently with the diffusion model implemented here (Ita and Cohen, 1997). We constrain the MgO melting curve at higher pressures using recent shock measurements that place a lower bound melting temperature of 9000 K at 240 GPa (Fat'yanov and Asimow, 2014). Second, we use the FeO end–member melting curve defined by the combined ex situ determinations by Fischer and Campbell (2010) to 77 GPa and Kato *et al.* (2016) to 131 GPa. Third, we assume that the effective T_m values for magnesiowüstite and ferropericlase vary linearly between these two end–members. This assumption is reasonable, given the large spread in reported high pressure melting temperatures of FeO (Fischer and Campbell, 2010; Komabayashi, 2014; Kato *et al.*, 2016) and MgO (see Fat'yanov and Asimow, 2014; for a review), as well as the spread in the pressure dependence of the solidus and liquidus curves for the (Mg,Fe)O solid solution (Zerr and Boehler, 1994; Zhang and Fei, 2008; Du and Lee, 2014; Deng and Lee, 2017). The data of melting temperatures for MgO and FeO as a function of pressure are shown in Figure 3.1[3].

---

[3] The bibliographical research on (Mg,Fe)O melting experiments and relative estimate of the melting temperatures was performed by J.M. Jackson

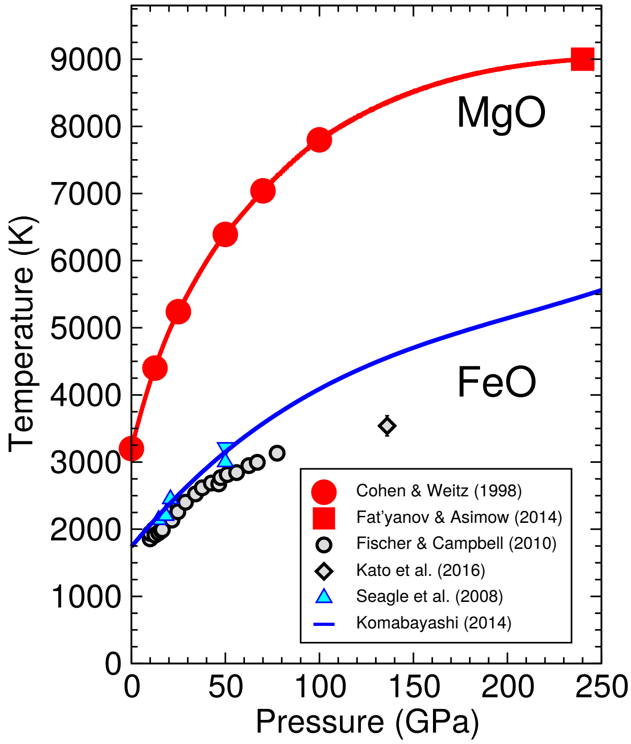

Figure 3.1: *melting temperatures of MgO and FeO as a function of pressure: experimental data.*

The self–diffusion coefficients to be implemented in the 2.5D–DD code for this study were evaluated starting from the results of Ita and Cohen (1997), which provide an empirical equation expressing the self–diffusion coefficients of Mg and O as a function of pressure and temperature:

$$\ln D^{sd}_{Ox}(P,T) = \ln(a^2\nu_a) + \frac{S_0 + PS'_0}{k_B} - \frac{E_0 + PV_0 + P^2V'_0}{k_BT} \tag{3.2}$$

where P is pressure in GPa and T is temperature in K. The other parameters are taken from oxygen self–diffusion data since the anion diffusion represent the slowest mechanism in MgO, and are listed in Table 3.2.

Starting from this equation it is possible to calculate the oxygen self–diffusion coefficient as a function of temperature for a fixed pressure. This was made for pressures ranging from 100 to 140 GPa and temperatures between 1500 and 4000 K. Each curve was sampled every 100 K and the retrieved values were plotted as a function of the homologous temperature in order to obtain a dataset to be fit with the homologous temperature

Equation parameter	Symbol	Value
Lattice constant	a	4.0 Å
Attempt frequency	ν_a	5.4 THz
Activation entropy $P = 0$	S_0	$4k_B$
S_0 pressure derivative	S_0'	$0.02k_B$/GPa
Activation energy	E_0	$9.4 \cdot 10^{-19}$ J
Activation volume $P = 0$	V_0	16.7 Å^3
V_0 pressure derivative	V_0'	-0.038 Å^3/GPa

Table 3.2: *oxygen self–diffusion parameters for MgO global fit as a function of pressure and temperature (from Ita and Cohen, 1997).*

relation highlighted in equation 3.1.

The obtained dataset along with the relative fit using the homologous temperature relation is showed in Figure 3.2[4], together with other experimental data on intrinsic anion self–diffusion for oxides and halides from the literature.

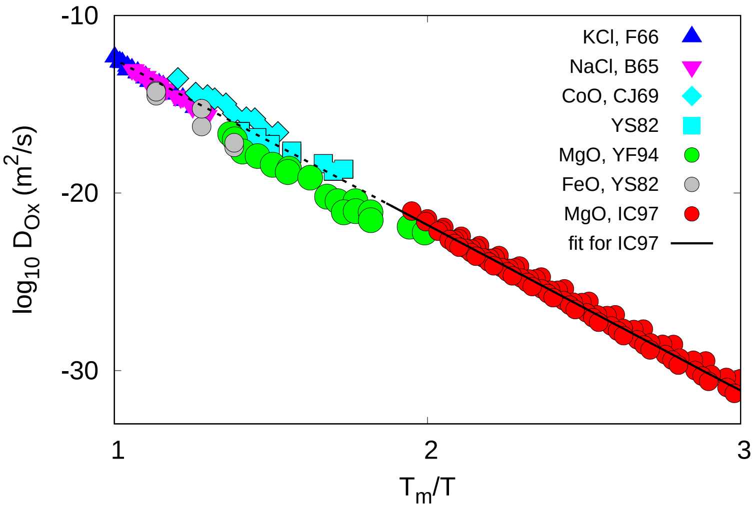

Figure 3.2: *oxygen self–diffusion coefficients D^{sd}_{Ox} as a function of the homologous temperature for different oxides and halides. The high pressure, high temperature numerical data on MgO obtained by Ita and Cohen (1997) (red dots) are fit using the homologous temperature relation described in equation 3.1 (black line), which is in good agreement also with other intrinsic, oxygen self–diffusion experimental data of oxides and halides retrieved from literature. F66: Fuller (1966), B65: Barr et al. (1965), CJ69: Chen and Jackson (1969), YS82: Yamaguchi and Someno (1982), YF94: Yang and Flynn (1994), IC97: Ita and Cohen (1997)*

The agreement between the scaling law adopted in this study and the ambient condi-

---

[4] The experimental data displayed in this figure were retrieved form the literature and analysed as a function of T/T_m by J. Van Orman

tion points is remarkable, and indicates that ionic crystals with the rock–salt structure all follow a common homologous temperature relationship with respect to intrinsic diffusion on the anion sublattice. The retrieved values for g and D_0 are -21.5 and $7.2 \cdot 10^{-4}$ m^2/s, respectively.

Substituting T_m of MgO with values for $(Mg_{0.80}Fe_{0.20})O$ and $(Mg_{0.16}Fe_{0.84})O$ at 120 and 135 GPa allows to calculate the intrinsic oxygen self–diffusion coefficient at a given temperature for the two different compositions. The diffusion coefficients are then evaluated in terms of the more canonical Arrhenius type of relation described in equation 2.8. Thus, the self–diffusion activation enthalpy is equal to:

$$\Delta H^{sd} = -gT_m k_B \tag{3.3}$$

while the pre–exponential factor D_0 is the same for equations 2.8 and 3.1.

The values obtained from this approach and employed in the present study are shown in Table 3.3.

	$(Mg_{0.16}Fe_{0.84})O$			$(Mg_{0.80}Fe_{0.20})O$	
	120 GPa	135 GPa	135 GPa	120 GPa	135 GPa
	2800 K	3200 K	3800 K	2800 K	3800 K
D_{Ox}^{sd} (m^2/s)	$3.4 \cdot 10^{-18}$	$8.2 \cdot 10^{-17}$	$9.1 \cdot 10^{-15}$	$6.2 \cdot 10^{-28}$	$4.6 \cdot 10^{-22}$
ΔH^{sd} (eV)	8.0	8.2	8.2	13.4	13.7
T_m (K)	4300	4440	4440	7224	7414
T/T_m	0.7	0.7	0.9	0.4	0.5

Table 3.3: *numerical values for D_{Ox}^{sd}, ΔH^{sd} and T_m employed in this study for (Mg,Fe)O.*

3.4 Dislocation dynamics creep simulations

3.4.1 Results

The strain evolution as a function of time for magnesiowüstite at the three tested PT conditions is shown in Figure 3.3 for all of the considered applied stresses. All the curves correspond to a linear behavior that allows for the determination of the creep strain rate as a function of stress.

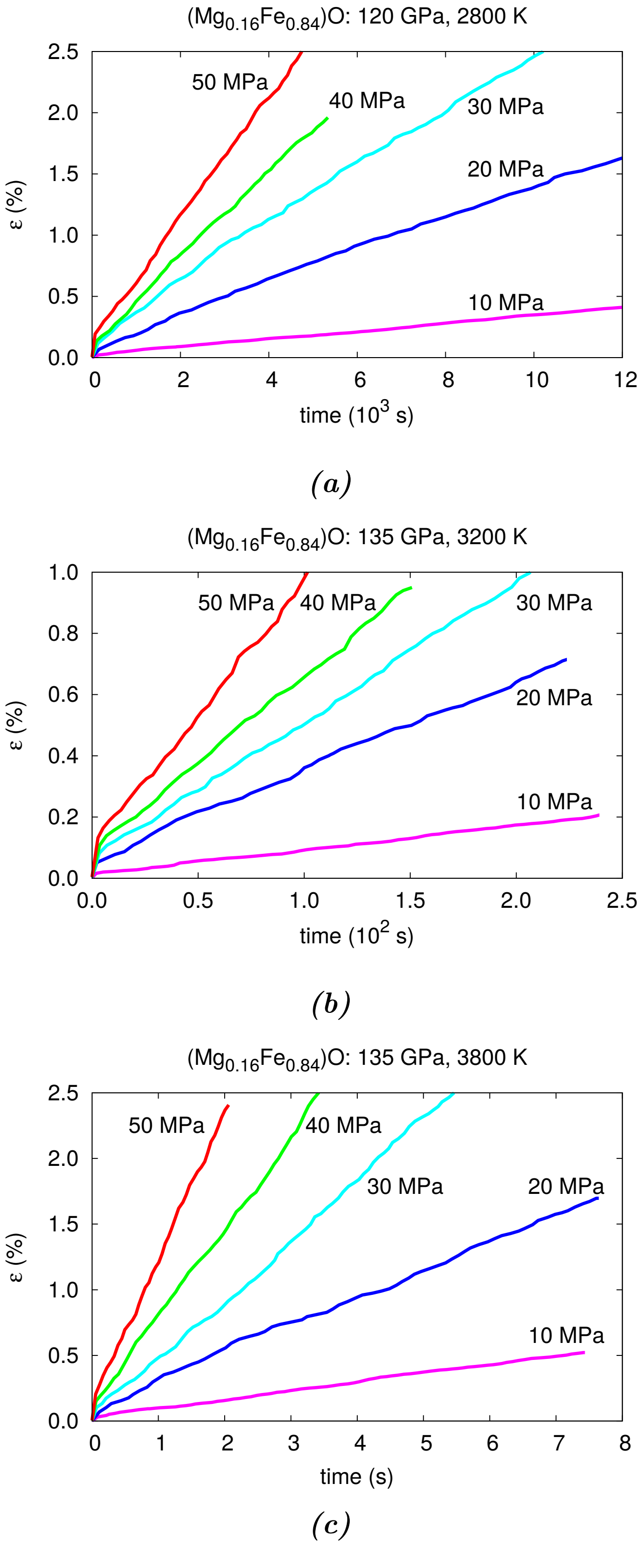

Figure 3.3: *$(Mg_{0.16}Fe_{0.84})O$ magnesiowüstite: plastic strain ε as a function of time at 2800 K and 120 GPa (a), 3200 K and 135 GPa (b) and 3800 K and 135 GPa (c). The values of the applied, deviatoric stress σ are also shown for each simulation.*

To further verify that the steady state condition is achieved, we plot the dislocation density as a function of time. This is done in Figure 3.4a where the results obtained at 135 GPa and 3800 K are shown. The dislocation densities oscillate around a constant value, demonstrating that dislocation annihilation and multiplication are counterbalancing each other. This means that the coupling of the two mechanisms introduced in the code – *i.e.* dislocation glide and climb – leads to a steady state equilibrium condition and therefore reproduces well the process of creep. Figure 3.4b displays the individual contributions of these two mechanisms to the resulting creep strain rate: it is evident that the vast majority of deformation is due to dislocation glide (ε_{glide}), which is a very efficient strain–producing mechanism. Climb, on the other hand, is diffusion–dependent, and therefore has a major control on the evolution of strain with time – *i.e.* it defines the timescale at which the deformation is taking place.

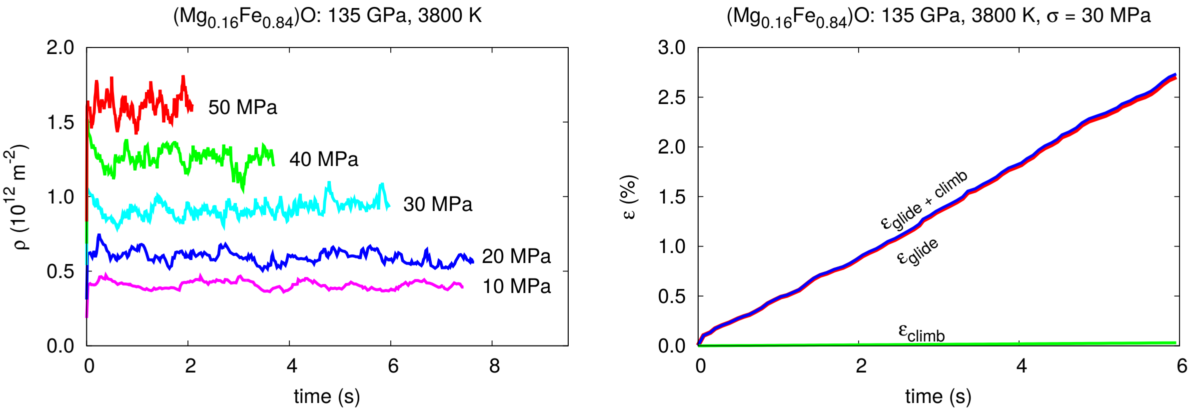

(a) ***(b)***

Figure 3.4: *($Mg_{0.16}Fe_{0.84}$)O magnesiowüstite: evolution of the dislocation density ρ as a function of time in the case at 3800 K and 135 GPa (a) and contribution of glide (ε_{glide}) and climb (ε_{climb}) to the total achieved strain ($\varepsilon_{glide+climb}$) (b). In this case the applied stress σ is 30 MPa.*

In Figure 3.3a,b,c this is evident from the different orders of magnitude on the time axes. Given that in this regime dislocation glide is athermal and therefore is not affected by temperature variations, a comparable deformation of 1–2% is achieved for every *PT* condition. On the other hand, the different temperatures affect the diffusion coefficient, on which the climb velocity is directly dependent (*cf.* equation 2.9), changing the time control of the dynamics and therefore the rate of deformation (*cf.* Section 2.4.3, Figure

2.8).

The results found in this study confirm that this kind of interplay works well to describe creep of (Mg,Fe)O after other studies had confirmed its validity by applying the same method at ambient conditions to olivine (Boioli *et al.*, 2015a) and MgO (Reali *et al.*, 2017).

The obtained strain as a function of time curves for ferropericlase ($(Mg_{0.80}Fe_{0.20})O$) are shown in Figure 3.5. As stated above, in this case several tests were run at higher applied stresses – up to 500 MPa – in order to obtain reliable deformations in practical simulation times. Nonetheless, a steady–state condition at the usual stresses from 10 to 50 MPa was verified also for each tested PT condition for ferropericlase.

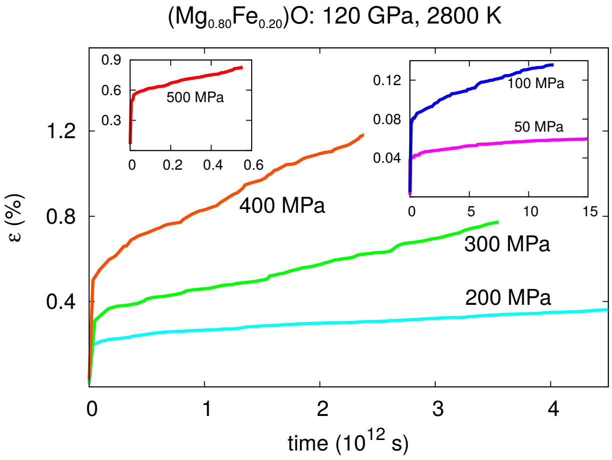

(a)

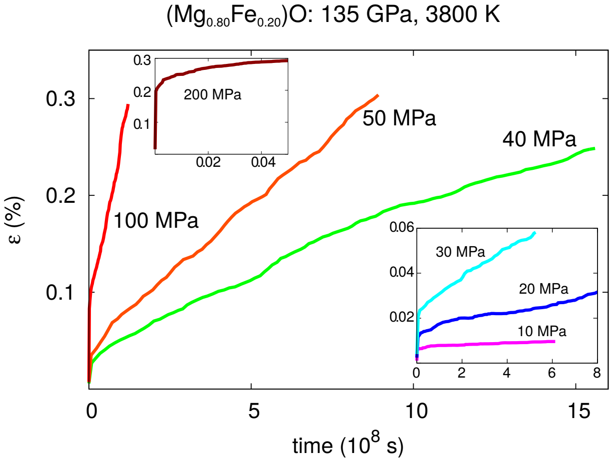

(b)

Figure 3.5: *$(Mg_{0.80}Fe_{0.20})O$ ferropericlase: plastic strain as a function of time at 2800 K and 120 GPa (a) and at 3800 K and 135 GPa (b). For each graph, the unities of the axes are the same for the main graph and the respective insets.*

It is therefore possible to evaluate the creep strain rates from the obtained curves and characterize them using the well established power law type of equation:

$$\dot{\varepsilon} = \dot{\varepsilon}_0 \sigma^n \exp\left(-\frac{Q}{k_B T}\right) \tag{1.8}$$

The strain rates as a function of stress for magnesiowüstite and ferropericlase are shown in Figure 3.6.

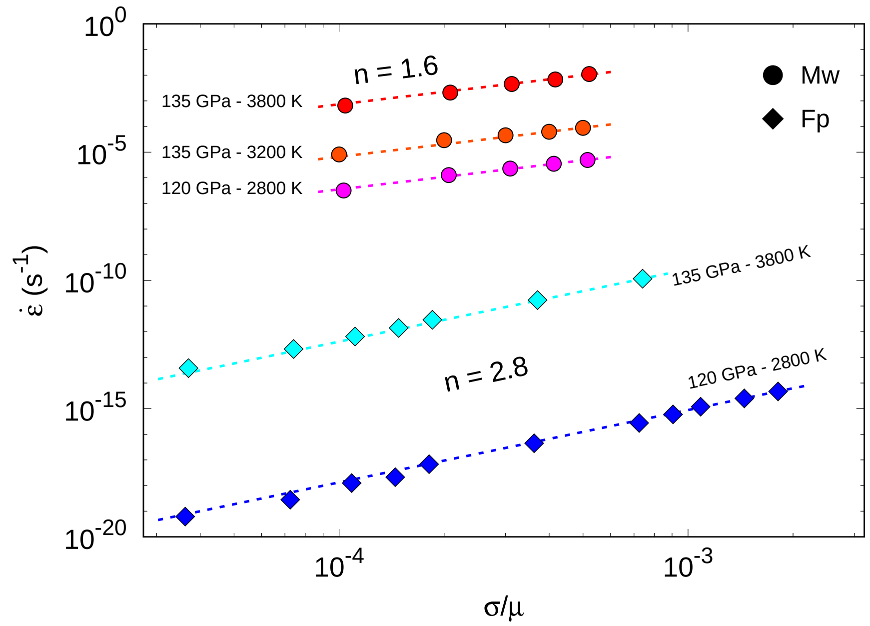

Figure 3.6: *creep strain rates $\dot{\varepsilon}$ as a function of stress σ (over the shear modulus μ) of ($Mg_{0.16}Fe_{0.84}$)O magnesiowüstite (Mw) and ($Mg_{0.80}Fe_{0.20}$)O ferropericlase (Fp). The average power law stress exponents n are also displayed for the two phases.*

The retrieved average stress exponents n are 1.6 for magnesiowüstite and 2.8 for ferropericlase. Regarding the evaluation of the creep activation enthalpy Q only a first attempt could be done for the case of magnesiowüstite at 135 GPa. This is the only case, in fact, where the strain rates could be compared at the same pressure and different temperatures. The obtained average value for Q in this case was 8.0 eV, in fair agreement with the oxygen self–diffusion activation enthalpy ΔH^{sd} previously evaluated for this pressure (that is, 8.2 eV, *cf.* Table 3.3). A similar result was also found by Reali *et al.* (2017) for MgO. Therefore, this finding further confirms how dislocation climb, which is diffusion–dependent, is the mechanism controlling the rate of deformation and therefore creep.

Knowing the strain rates it is possible to deduce the viscosity of (Mg,Fe)O. This is done by considering the effective viscosity η:

$$\eta = \frac{\sigma}{\dot{\varepsilon}} \tag{3.4}$$

The obtained viscosities for magnesiowüstite and ferropericlase at CMB conditions are shown in Figure 3.7.

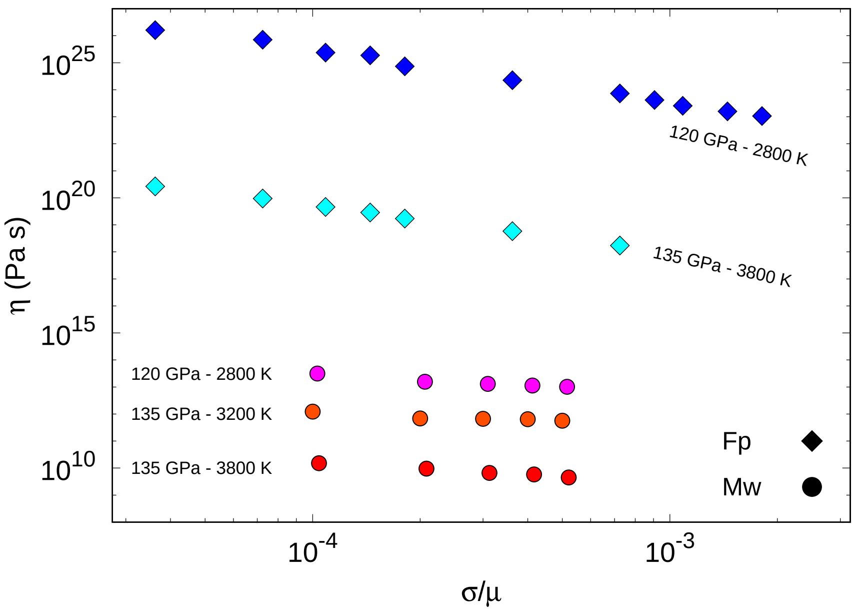

Figure 3.7: *viscosities η as a function of stress σ (over the shear modulus μ) for ($Mg_{0.16}Fe_{0.84}$)O magnesiowüstite (Mw) and ($Mg_{0.80}Fe_{0.20}$)O ferropericlase (Fp) at core–mantle boundary conditions.*

3.4.2 Discussion of uncertainties

The major result is the prediction that magnesiowüstite has a viscosity that is reduced by about 10 orders of magnitude relative to ferropericlase at CMB conditions. In support of these general conclusion, we consider some of the uncertainties involved in the methods presented here. One source of uncertainty is the estimate for T_m. A recent study on recovered samples from laser–heated diamond–anvil cell experiments up to 80 GPa suggests significantly low liquidus and solidus temperatures for ferropericlase (Deng and Lee, 2017). If this phenomena occurs at CMB conditions, this could explain why at the upper D'' conditions simulated here (120 GPa and 2800 K), ferropericlase exhibits smaller strain rates (10^{-19} s^{-1}, resulting in higher viscosities) than the expected values for this region (*i.e.* 10^{-16}–10^{-14} s^{-1}). Nonetheless, the value we obtain for ferropericlase at lowermost mantle conditions of 135 GPa and 3800 K is comparable (10^{-14} s^{-1}).

Other sources of uncertainty are the elastic properties of (Mg,Fe)O at CMB conditions. In the case of magnesiowüstite, we investigate the influence of increasing the shear modulus by 10% on our results at 135 GPa, as shown in Figure 3.8.

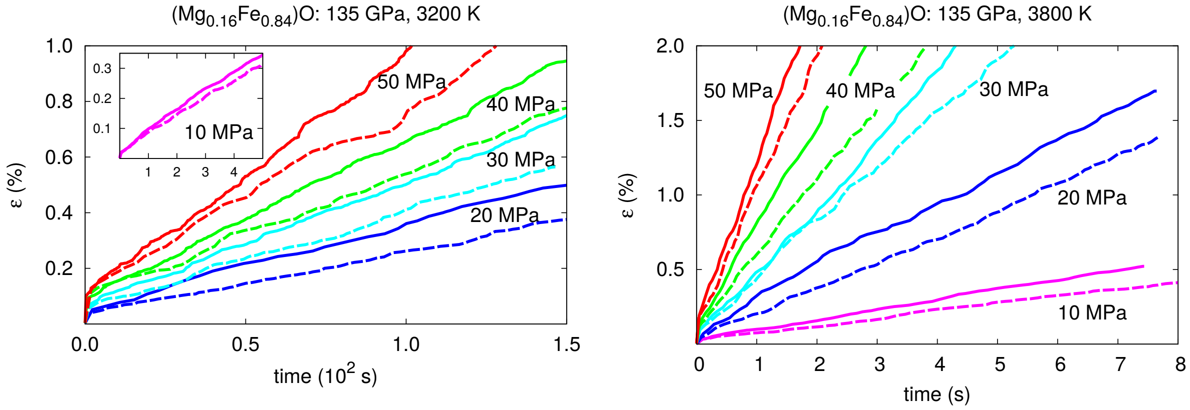

(a) *(b)*

Figure 3.8: *Strain as a function of time for ($Mg_{0.16}Fe_{0.84}$)O magnesiowüstite at 135 GPa and 3200 K (a) and at 3800 K (b); from 10 to 50 MPa of applied stress. The solid lines in (a) and (b) represent the same curves displayed in Figure 3.3b and 3.3c, respectively. The dashed lines represent the results obtained by raising the shear modulus of 10% for the same simulations. In (a), the inset shows the two cases for an applied stress of 10 MPa.*

By evaluating a stiffer material, we indirectly address two effects: a relatively cooler CMB and the uncertainty of the T_m value for Mw. By simulating a stiffer material (cooler CMB), for example, the conditions remain below the solidus of Mw. We find smaller strain rates for the stiffer Mw, varying rather uniformly between 20–30%, thus within the same order of magnitude. The numerical values of the different strain rates are displayed in Table 3.4.

It is becoming more likely that some ULVZs may represent chemically dense solid–state assemblages and others may indicate the presence of partial melts (*e.g.* Hernlund and Tackley, 2007; Hernlund and Jellinek, 2010; Li *et al.*, 2017). The stable phase assemblage

	3200 K			3800 K		
	$\dot{\varepsilon}$ (s^{-1})			$\dot{\varepsilon}$ s($^{-1}$)		
σ (MPa)	μ^a	μ + 10%^{b}	Ratio (%)	μ^a	μ + 10%^{b}	Ratio (%)
10	$8.2 \cdot 10^{-6}$	$5.9 \cdot 10^{-6}$	28	$6.6 \cdot 10^{-4}$	$4.9 \cdot 10^{-4}$	26
20	$2.9 \cdot 10^{-5}$	$2.3 \cdot 10^{-5}$	21	$2.1 \cdot 10^{-3}$	$1.5 \cdot 10^{-3}$	28
30	$4.5 \cdot 10^{-5}$	$3.5 \cdot 10^{-5}$	23	$4.6 \cdot 10^{-3}$	$3.6 \cdot 10^{-3}$	22
40	$6.2 \cdot 10^{-5}$	$4.8 \cdot 10^{-5}$	22	$6.8 \cdot 10^{-3}$	$4.9 \cdot 10^{-3}$	28
50	$8.8 \cdot 10^{-5}$	$6.9 \cdot 10^{-5}$	22	$1.1 \cdot 10^{-2}$	$8.7 \cdot 10^{-3}$	28

Table 3.4: *Strain rates of magnesiowüstite at 135 GPa and at 3200 K and 3800 K for different applied stresses* σ*. The results obtained by raising the shear modulus* μ *of 10% are also shown, together with the calculated difference with respect to the original ones.* ^{a}*In this case* μ *is equal to 100 and 96 GPa for the cases at 3200 and 3800 K, respectively (cf. Table 3.1), while* ^{b}*the values of* μ *here are raised by 10% (resulting in 110 and 105.6 GPa, respectively).*

in any particular region is dictated, in part, by phase equilibria and the relationship of the assemblage's solidus to the thermal profile, all of which have relatively large uncertainties in the D'' region (*e.g.* Lay, 2008; Zhang and Fei, 2008; Fiquet *et al.*, 2010; Fischer and Campbell, 2010; Andrault *et al.*, 2014; Du and Lee, 2014; Komabayashi, 2014; Nomura *et al.*, 2014; Tateno *et al.*, 2014; Pradhan *et al.*, 2015; Zhang *et al.*, 2016; Deng and Lee, 2017). Combined with previous reports on the sound velocities of magnesiowüstite that implicate its presence in ULVZs (Wicks *et al.*, 2017), the presence of such a low viscosity solid phase in localized patches above the CMB should influence the dynamics of the region.

3.5 Implications

The major result of our DD calculations is the prediction that iron–rich (Mg,Fe)O (magnesiowüstite) has a very low viscosity relatively to iron–poor (Mg,Fe)O (ferropericlase) at CMB conditions (Figure 3.7). Therefore, to assess the influence of low viscosity magnesiowüstite on the dynamics of the lowermost mantle we revisit the proposal that the sound velocities of an assemblage containing magnesiowüstite can explain a suite of seismic observations (Wicks *et al.*, 2010; 2017) and topography (Bower *et al.*, 2011) of

ULVZs[5].

3.5.1 Geodynamic model

The geodynamic model is described in detail by Bower *et al.* (2011). We use CitcomS (Moresi *et al.*, 2014) to solve the equations of mass, momentum, and energy conservation in cylindrical geometry for a small region near the CMB (23 degrees by 488 km). The model includes a chemically–distinct material that has a larger intrinsic density than ambient mantle to model the iron–rich assemblage that forms the ULVZ. The larger intrinsic density is defined by a fraction of magnesiowüstite coexisting with the silicate mantle which can explain seismic wave speed reductions (Wicks *et al.*, 2017). We now account for the contrast between the viscosity of iron–rich versus iron–poor (Mg,Fe)O by reducing the intrinsic viscosity of the chemically–distinct material relative to ambient mantle (*i.e.*, background material). The viscosity formulation therefore includes a compositional prefactor (compare with equation 8 of Bower *et al.*, 2011):

$$\eta(C,T) = \eta_C \exp[-\ln(10^q)T] \tag{3.5}$$

where η is viscosity, η_C a prefactor depending on composition (C) and q the order of magnitude viscosity contrast due to temperature (related to activation energy).

Composition, C, ranges from 0 to 1 and encompasses the two afore–mentioned chemical components. For the ambient mantle ($C = 0$) we select $\eta_C = 1$ and for ULVZ material ($C = 1$) a value of $\eta_C = 0.1$, which ensures a discernible effect of composition versus temperature on the flow pattern and hence the resulting geometry of the ULVZ. Since the ULVZ is not composed exclusively of ($Mg_{0.16}Fe_{0.84}$)O (Wicks *et al.*, 2010; Bower *et al.*, 2011; Wicks *et al.*, 2017), it would be both physically unreasonable and numerically intractable to prescribe the total 10 orders of magnitude of viscosity contrast between magnesiowüstite (component of ULVZ material) and ferropericlase (component of ambient mantle) retrieved here (Figure 3.7). Rather, the compositional prefactor extends the total viscosity range of the model to 4 orders of magnitude since $q = 3$. Other model parameters

---

[5] The geodynamic calculations outlined and presented in this section were performed by D.J. Bower. The discussion on the implications of such results was compiled by D.J. Bower and J.M. Jackson.

are the same as Bower *et al.* (2011) to enable a comparison of results.

Our new set of calculations prescribe an initial chemical layer thickness $d_{ch} = 4$ km at the base of the model, which was previously found to produce ULVZs that have reliefs within the mid–range of seismic predictions (Figures 8C, 9C of Bower *et al.*, 2011). Furthermore, we apply an isothermal and free–slip top boundary condition (referred to as "impermeable cases" in Bower *et al.*, 2011). At any given temperature, a non–dimensional buoyancy number B quantifies the intrinsic density contrast ($\Delta\rho_{ch}/\rho$) of the chemically–distinct (ULVZ) material – *i.e.* material with $C = 1$ – relatively to the ambient mantle. In this study, we choose $B = 0.75$, 1.00, 1.25, 2.00, 4.00, and 6.00 (Table 3.5). According to the formulation of Bower *et al.* (2011), the density contrast $\Delta\rho_{ch}/\rho$ spans from 1.1% ($B = 0.75$) to 9.0% ($B = 6.00$)

			No ULVZ reduction			With ULVZ reduction			Difference (%)		
Case	B	$\Delta\rho_{ch}/\rho$	H	$W_{1/2}$	A	H	$W_{1/2}$	A	H	$W_{1/2}$	A
1	0.75	1.1	39	87	0.45	35	102	0.34	-10	18	-24
2	1.00	1.5	38	100	0.38	31	111	0.28	-20	11	-26
3	1.25	1.9	32	109	0.29	28	122	0.23	-12	12	-21
4	2.00	3.0	28	132	0.21	23	145	0.16	-19	10	-24
5	4.00	6.0	20	179	0.11	18	202	0.09	-9	13	-18
6	6.00	9.0	17	227	0.07	15	260	0.06	-10	15	-14

Table 3.5: *Relief H (km), half–width $W_{1/2}$ (km), and aspect ratio $A = H/W_{1/2}$ for cases with (this study) and without (Bower et al., 2011) an intrinsic viscosity reduction for ULVZ material. Differences (%) are computed for the case with the ULVZ viscosity reduction relative to the case without the reduction. B is buoyancy number and the initial chemical layer thickness for all cases is $d_{ch} = 4$ km. $\Delta\rho_{ch}/\rho$ (%) is the density contrast of the chemically–distinct (ULVZ) material relatively to the ambient mantle.*

3.5.2 Morphology of low viscosity magnesiowüstite in ULVZs

We quantify the morphology of the ULVZ at steady–state by the relief H, defined as the 95% percentile of its height above the CMB, and half–width $W_{1/2}$, defined as half of its maximum (angular) footprint on the CMB. Table 3.5 shows the results for cases computed with (this study) and without (Bower *et al.*, 2011) an intrinsic viscosity reduction for ULVZ material. An intrinsic viscosity reduction produces flatter ULVZs than predicted in models that do not consider the rheology of iron–rich (Mg,Fe)O. In fact, heights decrease by 10–20% and half–widths increase by 10–18%, which results in aspect ratios A decreasing by 14–26% (Table 3.5). This is because the intrinsic reduction in the viscosity further decouples the ULVZ from the exterior flow than induced by the temperature–dependence of viscosity alone (Figure 3.9). The tractions on the boundaries of the ULVZ are reduced, which means the exterior flow is less dominant in supporting the intrinsically dense ULVZ above the CMB. Rather, the ULVZ slumps to a greater extent due to its intrinsic density contrast.

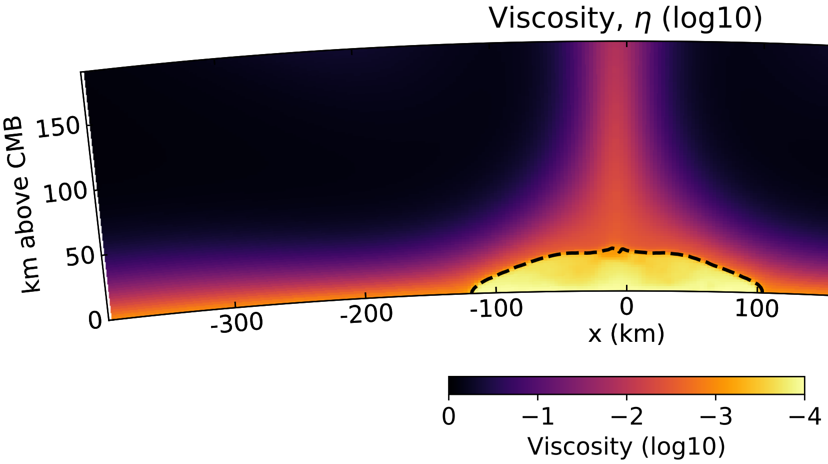

Figure 3.9: *case 2 ($B = 1$) shows that a ULVZ containing iron–rich (Mg,Fe)O has lower intrinsic viscosity than ambient mantle, which influences the morphology of the ULVZ (see Table 3.5 and text). The ULVZ is bounded at the CMB by the black dashed line.*

Hence, an implication of comparatively weak magnesiowüstite is that less iron–rich (Mg,Fe)O should be incorporated into the ULVZ assemblage to account for the relief of a particular ULVZ. This is because both reducing the viscosity of the ULVZ material and increasing its intrinsic density contrast results in a flatter ULVZ that is characterized by both reduced height and greater width. For example, the $B = 1$ scenario ($\Delta\rho_{ch}/\rho = 1.5\%$) would correspond to the inclusion of around 10 to 15 vol% magnesiowüstite into the mantle assemblage at CMB conditions, with the range depending upon the actual phase assemblage and iron partitioning (*e.g.* Bower *et al.*, 2011; Wicks *et al.*, 2017). Alternatively, another class of lowermost mantle seismic features could be explained by the presence of low viscosity magnesiowüstite. Kanamori (1967) and Buchbinder and Poupinet (1973) suggest that a thin core–mantle transition zone (CMTZ) could produce additional waveform complexity rather than a discontinuity, and further seismic studies indicate that a CMTZ of less than 4km thick could be an alternative explanation for some ULVZs (*e.g.* Vidale and Benz, 1992).

3.6 Conclusions

Dislocation dynamics simulations have been used to explore the dislocation creep behavior of (Mg,Fe)O ferropericlase and magnesiowüstite at D'' conditions. Upon retrieving the creep strain rates at different temperatures, pressures and applied stresses, we find that the viscosity of magnesiowüstite is reduced by about 10 orders of magnitude at the core–mantle boundary. By exploring the effects of an estimated viscosity contrast of a magnesiowüstite–bearing layer at the CMB, lower concentrations of magnesiowüstite would be required to explain the topographic relief reported in some ULVZ locations. However, thinner seismic features, such as the core–mantle transition zone, could host magnesiowüstite. In either of these cases, the recent findings that magnesiowüstite may have twice the shear wave anisotropy of postperovskite (Finkelstein *et al.*, 2018) suggests that the presence of only small amounts of magnesiowüstite may significantly alter the characteristics of the core–mantle boundary.

Chapter 4

Rheology of bridgmanite under lower mantle conditions

In this chapter[1] we try to constrain the deformation behavior of bridgmanite at lower mantle PT conditions. Bridgmanite is the main lower mantle constituent and its creep properties have a strong control on the dynamics and viscosity of this Earth's compartment.

The viscosity of the lower mantle, on the other hand, is poorly constrained due to the lack of knowledge on some fundamental variables controlling the deformation mechanisms of its main mineral phases, including bridgmanite.

This study assesses the rheology of bridgmanite by developing an approach based on mineral physics. Following and revising the recent advances in this field, pure climb creep controlled by diffusion is identified as the key mechanism driving deformation in bridgmanite. With respect to the previous chapters, therefore, a different creep mechanism has to be proposed for bridgmanite and its efficiency must be accounted for. This necessity arises from the combination of recent results from both experiments and computations. They converge, in fact, in evidencing that dislocatios moving by glide in bridgmanite encounter an extremely high lattice resistance. The stresses required for this type of motion are not available in the lower mantle and, relatively to this difficult glide mobility, dislocation climb becomes a much more efficient mechanism.

In Chapters 2 and 3 the power law creep of (Mg,Fe)O was characterized by a very

---

[1] The present chapter is based on the following manuscript: Reali, R., Van Orman, J., Pigott, J.S., Jackson, J.M., Boioli, F., Carrez, P., and Cordier, P. Diffusion and rheology of bridgmanite under lower mantle conditions. *Scientific Reports*, 2018 (*submitted*).

efficient dislocation glide, providing the majority of plastic deformation, and a rate–controlling dislocation climb. In the case of bridgmanite, being glide severely hindered, the climb mechanism may be responsible for both plastic shear development and rate–control. Again, climb is intimately bonded to diffusion, therefore this process will be of primary importance for the case of bridgmanite, too.

The strain rates of this phase under lower mantle pressures, temperatures and stresses are thus calculated by constraining diffusion and implementing a creep theoretical model. The viscosity of $MgSiO_3$ bridgmanite is consequently evaluated and compared with the viscosity profiles available from the literature. We show that the inferred variability of viscosity in these profiles can be fully accounted for with the chosen variables of our calculation, *e.g.*, diffusion coefficients, vacancy concentrations and applied stresses. A refinement of these variables is advocated in order to further constrain viscosity and match the observables.

Keywords: lower mantle; rheology; bridgmanite; diffusion; dislocation climb; creep; viscosity

4.1 State of the art

Significant insight into the major features that affect the surface of the Earth (seismicity, volcanism, mountain building) has been gained through the understanding that global convection animates the mantle to dissipate the internal heat of our planet. However, some fundamental aspects of mantle dynamics remain poorly understood, including the rheology.

4.1.1 Evidences from observables

From the observational point of view, the first constraint on the rheology of the mantle was deduced from the analysis of post–glacial uplift (Haskell, 1935), which assessed the viscosity of the upper mantle to be ~10^{22} Pa·s. This estimation has proved to be very robust over the years. However, further studies based on modelling of mantle convection (Bunge *et al.*, 1996; Tackley, 1996), the geoid (Hager and Richards, 1989; King and

Masters, 1992; King, 1995; Bunge and Richards, 1996), tectonic plate velocities (Ricard *et al.*, 1993; Butterworth *et al.*, 2014), true polar wander (Phillips *et al.*, 2009) and length of day variations Sabadini and Yuen (1989) have consistently pointed out a significant increase in viscosity (10^1 – 10^2 times) between the upper and the lower mantle. Most proposed profiles consist of a broad viscosity hill in the middle of the mantle, at a depth roughly between 1200 and 2000 km (Ricard and Wuming, 1991; Forte and Mitrovica, 2001; Mitrovica and Forte, 2004; Morra *et al.*, 2010). Some recent studies, however, suggest a rheology contrast located around 1000 km depth (Ballmer *et al.*, 2015; Rudolph *et al.*, 2015; *cf.* Section 1.1.3, Figure 1.4).

Another strong constraint on deep mantle convection is linked to seismic anisotropy, which can provide clues on the active deformation mechanisms. Very early, dislocation creep was postulated as a potential deformation mechanism in crystalline rocks in the mantle (Orowan, 1965). Besides implying a non–linear rheology, dislocation creep is also very efficient in producing lattice preferred orientation (LPO) and this is a very fruitful line of interpretation of seismic anisotropy in the upper mantle (Mainprice *et al.*, 2000). In a thick layer consisting of elastically anisotropic phases, such as the lower mantle, activation of dislocation creep is expected to generate detectable seismic anisotropy, which is inconsistent with observations (Meade *et al.*, 1995). Although most of the lower mantle is relatively under–sampled in terms of seismicity, the absence of strong evidence for seismic anisotropy between 700 km and 2700 km (Mainprice *et al.*, 2000; Meade *et al.*, 1995; Montagner and Kennett, 1996) provides some constraints.

This lack of anisotropy has led to the common assumption that diffusion creep, which does not lead to LPO, is the dominant deformation mechanism in the lower mantle (Karato and Li, 1992). Unlike dislocation creep, diffusion creep corresponds to a linear viscous behaviour. Most importantly, diffusion creep is strongly grain size–dependent (*cf.* Section 1.3.2, equation 1.12). Since this parameter is extremely poorly constrained in the mantle, the conditions imposed by the mean grain size, the grain size distribution and its possible evolution have attracted attention recently (Rozel *et al.*, 2011; Glišović *et al.*, 2015).

4.1.2 Evidences from experiments

Mineral physics represents another important approach to place constraints on mantle convection. Bridgmanite, *i.e.* (Mg,Fe,Al)(Si,Fe,Al)O_3 with the orthorhombic perovskite structure, is thought to be elastically anisotropic (Wentzcovitch *et al.*, 2004) and is considered to be the main constituent of the bulk lower mantle, along with (Mg,Fe)O ferropericlase and $CaSiO_3$ perovskite (Irifune, 1994). The rheology of this mineral is thus of primary importance to understand and model convection in the mantle and the dynamics of Earth's interior. However, bridgmanite is only stable under lower mantle conditions and measurements of the strength of materials under simultaneous high pressures and high temperatures are extremely difficult.

Multiple studies have been devoted to creep in minerals with the perovskite structure – *e.g.* on $BaTiO_3$ (Beauchesne and Poirier, 1989), $KTaO_3$ and $KNbO_3$ (Beauchesne and Poirier, 1990), $CaTiO_3$ and $NaNbO_3$ (Wright *et al.*, 1992) and $SrTiO_3$ (Wang *et al.*, 1993) – providing evidence for dislocation activity. As for bridgmanite, the first deformation experiments performed at room temperature in the diamond anvil cell (DAC) suggested a high strength with little if any indication of plasticity by dislocation glide (Meade and Jeanloz, 1990; Merkel *et al.*, 2003; Wenk *et al.*, 2004). More recent experiments using laser–heated DAC showed, however, some indication of plastic slip in bridgmanite (Miyagi and Wenk, 2016).

The development of opposed– and multi–anvil devices to allow high pressure and high temperature deformation experiments represents a major breakthrough, since it opens the path for direct investigation of mantle phases (Cordier *et al.*, 2004). Using the recently developed rotational Drickamer apparatus (RDA), the first deformation experiments on a bridgmanite and ferropericlase assemblage at pressures and temperatures of the uppermost lower mantle have been performed (Girard *et al.*, 2015). It was demonstrated that even at a temperature in excess of 2000 K, bridgmanite retains a very high strength (~4 – 5 GPa). Microstructural investigation revealed that bridgmanite deformed under these conditions through activation of dense shear lamellae (Nzogang *et al.*, 2018).

In another study where bridgmanite was deformed at 25 GPa, 1873 K in a deformation–DIA apparatus (Tsujino *et al.*, 2016), a clear development of lattice preferred orientation was linked to the activation of [001](100) slip. No stress was reported in this study. Some studies have, however, demonstrated the possibility for diffusion creep and even superplasticity in $CaTiO_3$, a mechanism which could be compatible with seismic observations (Karato and Li, 1992; Karato *et al.*, 1995; Li *et al.*, 1996).

4.1.3 Evidences from numerical modeling

In parallel, recent theoretical calculations related to the physics of dislocations in $MgSiO_3$ bridgmanite confirm that the lattice friction remains very high, even at high temperature (Kraych *et al.*, 2016b), in excellent agreement with the aforementioned experimental results (Girard *et al.*, 2015). Furthermore, insights into slip systems and plastic anisotropy of $MgSiO_3$ bridgmanite were first gained from modelling dislocation cores and lattice friction at the atomic scale (Carrez *et al.*, 2007; Ferré *et al.*, 2007; Gouriet *et al.*, 2014; Hirel *et al.*, 2014; 2016b).

More recently, high temperature dislocation glide has been characterized from the modelling of thermally activated processes underlying dislocation glide at finite temperature (Kraych *et al.*, 2016b). From these theoretical developments, the velocity of dislocations and the flow stress of the material could be calculated not only at pressures and temperatures relevant to the lower mantle, but also at relevant strain rates, without extrapolation or parameter adjustment.

For $MgSiO_3$ bridgmanite, such calculations demonstrate that lattice friction remains very high, even at high temperatures and mantle strain rates, and that deformation through dislocation glide appears to be extremely unfavourable at mantle conditions (Kraych *et al.*, 2016a).

4.1.4 An alternative mechanism

As a matter of fact, glide is not the only possible mechanism for dislocations to move and produce strain. At high temperature, in fact, dislocations in bridgmanite interact strongly with vacancies and, by absorbing them, can move via climb (Hirel *et al.*, 2016a).

Deformation by climb, without glide, and possibilities for creep involving it, has received little attention, although it had been originally suggested that it might be relevant for rheology in planetary interiors (Nabarro, 1967). Some microstructural evidence for climb has been reported, however, in $KTaO_3$ and $KNbO_3$ perovskite deformed by creep at high temperature (Beauchesne and Poirier, 1990).

Furthermore, it has been demonstrated by dislocation dynamics modelling that dislocations in bridgmanite moving by climb alone could lead to steady state creep with a strain–producing efficiency superior to that of diffusion creep (Boioli *et al.*, 2017). The main implication of this discovery is that the poorly constrained grain size is not a factor controlling the rheology of bridgmanite in the uppermost lower mantle.

Although pure climb creep is mediated by dislocation motion, it is similar to diffusion creep, for which strain is diffusion–controlled. As with diffusion creep, pure climb creep is consistent with the observed isotropy in the bulk of the lower mantle, since materials deforming by this mechanism do not develop rigid body rotations, which are responsible for LPO. Diffusion, therefore, represents the key to the rheology of bridgmanite. In the present chapter, we revisit the available data on diffusion in bridgmanite under lower mantle conditions. The results are incorporated into a pure climb creep model (Nabarro, 1967) to propose constraints on the viscosity of bridgmanite in the lower mantle.

4.2 Diffusion in bridgmanite

The rate of dislocation climb is ultimately limited by self–diffusion of the slowest diffusing atomic species.

Experimental studies of self–diffusion in bridgmanite[2] indicate that oxygen (Dobson, 2003; Dobson *et al.*, 2008) diffuses significantly faster than Mg or Si (Dobson *et al.*, 2008; Yamazaki *et al.*, 2000; Xu *et al.*, 2011). This feature is shared with many other perovskite–structured oxides, in which the energy of oxygen vacancy migration is more favourable compared to the one of cation vacancies, leading to rapid oxygen transport and sluggish cation diffusion (Islam, 2000).

We therefore focus on cation diffusion as the rate–limiting step for dislocation climb in bridgmanite.

---

[2] The critical assessment of experimental results was carried on by J. Van Orman and J.S. Pigott

4.2.1 Overview on the experimental data

Self–diffusion coefficients for Mg and Si (Dobson *et al.*, 2008; Yamazaki *et al.*, 2000; Xu *et al.*, 2011) have been measured at pressures relevant to the top of the lower mantle (~25 GPa) using a multi–anvil press combined with secondary ion mass spectrometry (SIMS) in depth profiling mode. Both polycrystalline (Dobson *et al.*, 2008; Yamazaki *et al.*, 2000) and single crystal (Xu *et al.*, 2011) bridgmanite samples were tested. In the former case, both volume and grain boundary diffusion coefficients were extracted, whereas in the latter the single crystals avoided complications from grain boundary diffusion.

In all cases, however, the characteristic volume diffusion length was <200 nm. The interpretation of such short profiles from high–pressure experiments is uncertain, due to analytical artefacts that arise from surface roughening and various ion beam mixing effects in SIMS depth profiling. To have a high level of confidence in the diffusion coefficient measurements, particularly when the diffusion profiles are so short, it is critical to measure the diffusion coefficient in separate experiments at the same conditions, over a range of time that is sufficient to generate substantially different profile lengths. Ideally, the diffusion anneal times at one set of conditions would extend over at least an order of magnitude, which would generate diffusion profiles that range in length over approximately a factor of 3. None of the experimental self–diffusion studies on bridgmanite have included a convincing time series – the range of times extends only over a factor of ~2, and there is no resolvable change in the length of the profiles with time.

Since we cannot be confident that the cation isotope concentration profiles presented in any of the published studies represent true volume diffusion profiles, we conservatively treat the diffusion coefficients extracted from these profiles as upper bounds on the true diffusion coefficients. We focus below on the single crystal experiments (Xu *et al.*, 2011), because they characterized both silicon and magnesium diffusion, but these data agree within uncertainty with the results obtained with polycrystals (Dobson *et al.*, 2008; Yamazaki *et al.*, 2000).

4.2.2 Numerical modeling approach

Further constraints on cation diffusion coefficients in bridgmanite come from first principles calculations and atomistic simulations. Theoretical calculations of the self–diffusion coefficients (D^{sd}) are based on the following equation (*cf.* Section 1.3.1):

$$D^{sd} = f X_v D_v \tag{4.1}$$

where f, the correlation coefficient, has a value close to unity and is often neglected, X_v is the fraction of vacant sites on the relevant sub–lattice, and the vacancy diffusion coefficient, D_v, is definded similarly to equation 1.2:

$$D_v = \frac{N_j}{6} l_j^2 \nu_j \exp\left(-\frac{\Delta H_{m,Mg}}{k_B T}\right) \tag{4.2}$$

Where N_j is the number of equivalent jumps that a vacancy can make to adjacent sites, l_j is the jump distance, ν_j is the jump attempt frequency and $\Delta H_{m,Mg}$ is the migration enthalpy.

The migration enthalpies, jump distances, and vibration frequencies for Mg and Si have been obtained by density functional theory calculations over the pressure range of the lower mantle (Ammann *et al.*, 2009; 2010b). Within uncertainty, the Mg and Si self–diffusion coefficients derived from experiments are equivalent (Xu *et al.*, 2011). The migration enthalpies calculated from first principles using the local density approximation, are also equivalent for Si (3.6 eV) and Mg (3.4–3.7 eV) at 25 GPa (Ammann *et al.*, 2010b).

We use the values for Mg, because a more extensive set is available (Ammann *et al.*, 2009; 2010b) than for Si (Ammann *et al.*, 2010b), and because Mg diffuses by a simple direct jump process, rather than the complicated six–jump cycle described for the case of Si diffusion. The migration enthalpy for magnesium as a function of pressure is based on simulations of Mg diffusing along the lowest energy pathways ([110]a,b and [001]) via a single jump (Ammann *et al.*, 2009), resulting in $N_j = 6$ possible jumps (two equivalent jumps for each principal direction). The jump distances and frequencies as functions of pressure are retrieved from Ammann *et al.* (2010b).

The self–diffusion coefficients can then be calculated according to equation 4.1, provided that the vacancy concentration is known.

4.2.3 The vacancy concentration

The vacancy concentration X_v can be bounded at the low end by the intrinsic concentration of vacancies, which depends only on the vacancy formation energy (equation 1.1). Atomistic simulations show that the SiO_2 pseudo–Schottky defect is the least favourable defect and therefore that Si is the rate–limiting species in an intrinsic diffusion regime (Watson *et al.*, 2000). Assuming a purely intrinsic defect mechanism, we calculate the Si vacancy concentration as a function of pressure based on the SiO_2 pseudo–Schottky formation enthalpy fit as a function of pressure from Watson *et al.* (2000). This results in an intrinsic Si vacancy concentration spanning between 10^{-20} and 10^{-14} throughout the pressure range of the lower mantle.

At the high end, we can define the upper limits on the diffusion coefficient considering an extrinsic regime as determined by experiments, with an evaluation of a reasonable interval of variability for the vacancy concentration.

It is possible to indirectly estimate an upper limit on X_v from equation 4.1 by combining the D^{sd} coefficients obtained by Xu *et al.* (2011) on magnesium self–diffusion in bridgmanite and the D_v values estimated using the Ammann *et al.* (2010b) approach at the same pressure and temperatures.

In Table 4.1 the numerical values for D^{sd} and D_v from experiments and first principles atomistic simulations, respectively, are provided together with the X_v values, estimated inverting equation 4.1. In accordance with the experimental data of Xu *et al.* (2011), the pressure is here fixed at 25 GPa.

This calculation gives upper limits on the Mg vacancy concentration that are consistently on the order of 10^{-3}. Hence, we treat 10^{-3} as the upper bound on the cation vacancy concentration in bridgmanite in the lower mantle. Although this upper bound estimate was obtained from experiments on nominally pure $MgSiO_3$, we note that the addition of trace or minor elements is unlikely to change the cation vacancy concentration significantly, as long as oxygen vacancies remain the predominant point defect. In general, due to the necessity for maintaining charge balance, minerals do not hold high

T (K)	D^{sd}_{Mg} (m^2/s)^a	$D_{v,Mg}$ (m^2/s)^b	X_v
1670	$2.6 \cdot 10^{-20}$	$2.6 \cdot 10^{-18}$	$1.0 \cdot 10^{-2}$
1770	$1.5 \cdot 10^{-20}$	$1.1 \cdot 10^{-17}$	$1.4 \cdot 10^{-3}$
1870	$2.1 \cdot 10^{-19}$	$4.0 \cdot 10^{-17}$	$5.2 \cdot 10^{-3}$
1870	$1.9 \cdot 10^{-19}$	$4.0 \cdot 10^{-17}$	$4.6 \cdot 10^{-3}$
2070	$1.1 \cdot 10^{-18}$	$3.6 \cdot 10^{-16}$	$2.9 \cdot 10^{-3}$

Table 4.1: *the vacancy concentration X_v is indirectly estimated using equation 4.1. The magnesium self–diffusion coefficients D^{sd}_{Mg} are from Xu et al. (2011)^a and the vacancy diffusion coefficients $D_{v,Mg}$ are calculated from Ammann et al. (2010b)^b. Both D^{sd}_{Mg} and $D_{v,Mg}$ are estimated at 25 GPa.*

concentrations of extrinsic cation and anion vacancies simultaneously. As a lower bound on the extrinsic vacancy concentration, we assume a value of 10^{-6}.

4.2.4 Self–diffusion coefficients

For the present study, the chosen PT conditions for the investigation of bridgmanite rheology are the ones of a given mantle geotherm (Stacey and Davis, 2004).

In Figure 4.1 we show the diffusion coefficients calculated according to equations 4.1 and 4.2 along the considered geotherm.

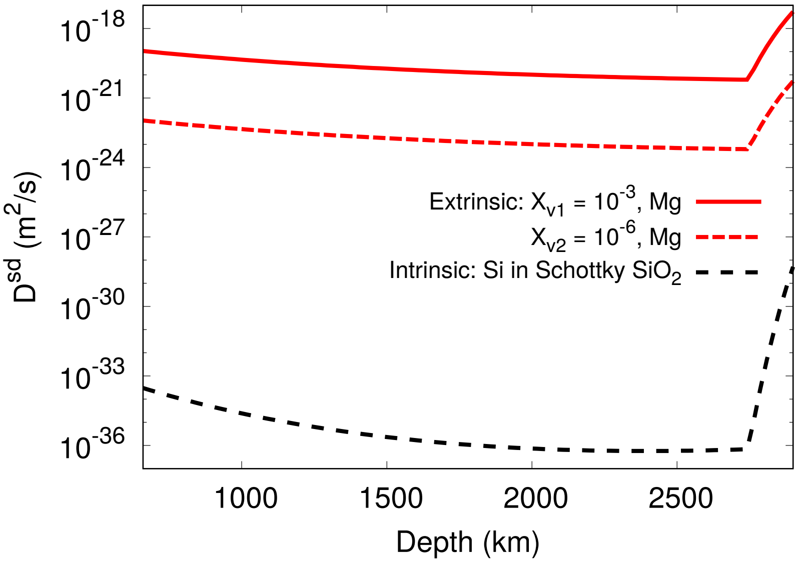

Figure 4.1: *diffusion coefficients D^{sd} along the geotherm. Here are shown the values for intrinsic diffusion obtained from the Si Schottky vacancy formation enthalpy of Watson et al. (2000) (black dashed line) together with the extrinsic values for Mg obtained with the selected vacancies concentrations X_{v1} and X_{v2} (solid and dashed red lines, respectively).*

It is evident that the values calculated considering an intrinsic vacancy concentration for Si are not meaningful with respect to terrestrial timescales of deformation. Hence, the upper and lower bounds for extrinsic cation diffusion will be considered as inputs in the creep model for bridgmanite, which is described in the next paragraph.

In Table 4.2 all the necessary parameters to calculate the magnesium self–diffusion coefficients at different pressures are provided.

P (GPa)	*Depth* (km)	T (K)	ν_j (THz)	l_j (Å)	D^{sd}_{Mg} (m^2/s)	$\Delta H_{m,Mg}$ (eV)
30	809	1992	5.9	2.42	3.8	$7.1 \cdot 10^{-20}$
60	1457	2256	8.9	2.36	4.7	$2.0 \cdot 10^{-20}$
90	2060	2487	12.9	2.31	5.4	$9.6 \cdot 10^{-21}$
120	2617	2689	17.5	2.27	5.9	$6.5 \cdot 10^{-21}$

Table 4.2: *estimate of the parameters necessary to evaluate the self–diffusion coefficients* D^{sd}_{Mg} *at different pressures along the geotherm (Stacey and Davis, 2004) using equations 4.1 and 4.2. The vacancy concentration* X_v *is here set equal to* 10^{-3}.

4.3 Pure climb creep model

In this chapter, following the work of Boioli *et al.* (2017), we investigate the steady state creep behavior of bridgmanite resulting from deformation by pure climb (Nabarro, 1967). This mechanism considers crystals containing a network of dislocations (dislocation density ρ) which move by pure climb (*i.e.* a displacement perpendicular to the glide plane by emission/absorption of point defects).

4.3.1 Formulation

In the original work of Nabarro (1967), the need for climb arose from a large density of jogs on the dislocation lines resulting from the mutual crossing of the dislocations, which drastically reduces the efficiency of glide. In the present case, on the other hand, climb requires attention due to the high lattice friction which inhibits glide in bridgmanite (Kraych *et al.*, 2016a;b).

In pure climb creep, dislocations play the role of sources and sinks of point defects (the same role played by grain boundaries in Nabarro–Herring creep, *cf.* Section 1.3.2). By absorbing or emitting vacancies or ions, dislocations move by climb and produce strain (without producing lattice rotation). The strain rate resulting from this process reads (Nabarro, 1967):

$$\dot{\varepsilon} = \frac{D_{Mg}^{sd}\mu b}{\pi k_B T}\left(\frac{\sigma}{\mu}\right)^3 \bigg/ \ln\left(\frac{4\mu}{\pi\sigma}\right) \tag{1.14}$$

where D_{Mg}^{sd} is the self–diffusion coefficient as discussed above, σ is the applied, deviatoric stress and μ is the shear modulus.

According to the derivation made by Nabarro, pure climb creep results in a non–linear rheology, where the strain rate depends on stress to the power of 3. Indeed, in pure climb creep, the dislocation network is established under the balancing influences of dipole annihilation and multiplication from the operation of Bardeen–Herring sources (Bardeen and Herring, 1952; more insights on this mechanism are provided in the next section).

4.3.2 Comparison with pure climb DD data

Compared to the Boioli *et al.* (2017) simulations, where the initial dislocation density was a simulation parameter, Nabarro's model accounts for steady state conditions by allowing the microstructure to adjust its equilibrium dislocation density with respect to the applied stress. Despite this difference, the results of the dislocation dynamics model of Boioli *et al.* (2017) are in excellent agreement with the theoretical predictions of equation 1.14 from Nabarro (1967).

This is shown in Figure 4.2, where the data from pure climb numerical modeling obtained with DD are compared with the Nabarro (1967) model. The latter (red line) reproduces well the results obtained by 2.5D–DD simulations of pure climb creep from Boioli *et al.* (2017; green and blue dots and relative fit lines). To be consistent with the Boioli *et al.* (2017) study, which addresses creep at the uppermost lower mantle, the PT conditions as well as the vacancy concentration X_v are the same for the current model and the numerical simulations and are specified in the title of the figure.

As stated above, the main difference between these approaches is related to dislocation density. In fact, in the present chapter we implement a creep mode that is formulated accounting for an equilibrium dislocation density that depends on the applied stress and

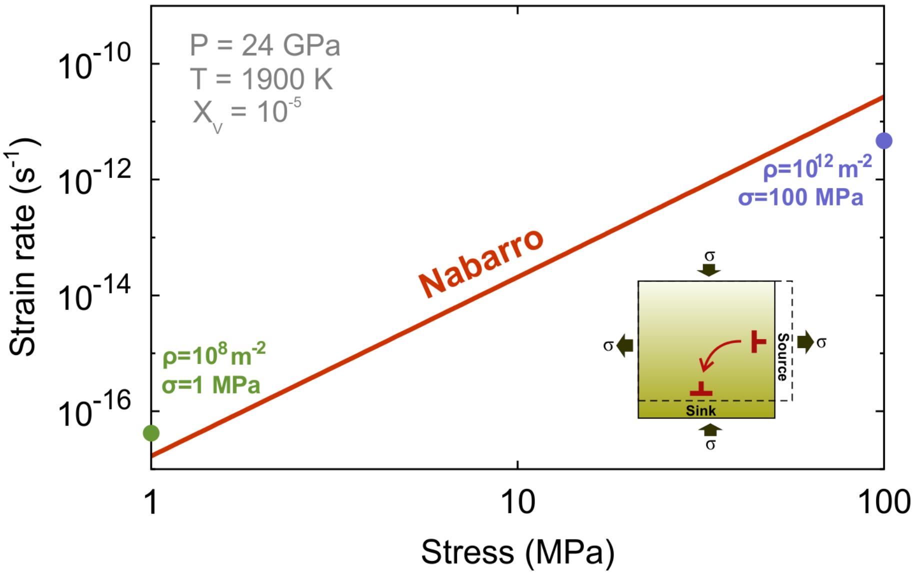

Figure 4.2: *comparison between the strain rates predicted at uppermost lower mantle by the Nabarro (1967) model (red line) and the data from pure climb numerical modeling obtained with 2.5D–DD (Boioli et al., 2017) (green and blue points, depending on the initial dislocation density given as an input parameter). The Nabarro model is here compiled with inputs resembling the same PT conditions (shown in the graph) at which the DD data were obtained.*

leads to a steady–state creep condition (see above). On the other hand, different values of the initial dislocation density have been used as input parameter in the 2.5D–DD model. In particular, the initial dislocation density was set equal to 10^8 and 10^{12} m^{-2} (green and blue curves in Figure 4.2, respectively).

A unification of these results can be achieved by considering the Taylor equation, that scales the dislocation density ρ as function of the applied stress σ, similarly to equation 2.7:

$$\rho = \left(\frac{\sigma}{\alpha b \mu}\right)^2 \tag{4.3}$$

where α is the adimensional Taylor coefficient, b is the Burgers vector and μ the shear modulus. α does not appear in the pure climb creep formulation and is therefore set to be 1, while at these conditions b was estimated equal to 4.65 Å (Kraych *et al.*, 2016a) and μ to 167 GPa (Dziewonski and Anderson, 1981). With equation 4.3 it is easily calculated that, for stresses of 1 and 100 MPa, the relative dislocation density is equal to ~10^8 and 10^{12} m^{-2} respectively. This is in perfect agreement with the 2.5D–DD data, obtained for a fixed dislocation density of 10^8 and 10^{12} m^{-2}. The present model, in fact, reproduces comparable strain rates (*i.e.*, the red line crosses the green and blue lines) at identical dislocation densities and stresses of 1 and 100 MPa.

4.4 Results

The pure climb creep model of Nabarro (1967) allows the calculation of the strain rates of bridgmanite at given pressures and temperatures and as a function of stress. Here we make calculations along a geotherm (Stacey and Davis, 2004) for specific values of the deviatoric stresses σ, to which relevant values of 1 and 10 MPa were attributed (Kaula, 1963; McKenzie, 1966). The shear modulus μ of bridgmanite and its pressure–depth dependence were estimated using values from the Preliminary Reference Earth Model, PREM (Dziewonski and Anderson, 1981).

4.4.1 Pure climb creep vs. diffusion creep

It is possible to compare the efficiency of pure climb creep and diffusion (Nabarro–Herring, *cf.* Section 1.3.2) creep by building deformation maps. In this case, the critical parameter is the grain size.

While the specifics of pure climb creep at lower mantle PT conditions were outlined above, it is useful to recall here the constitutive equation of diffusion creep, which reads:

$$\dot{\varepsilon} = A_{NH} \frac{D\sigma\Omega}{d^2 k_B T} \tag{1.12}$$

where d is the grain size and Ω is the atomic volume, equal to the elementary cell volume divided by the number of formula units per unit cell. The cell volume at the considered PT conditions was estimated from the Mie–Grüneisen–Debye Vinet equation of state for $MgSiO_3$ bridgmanite (Tange *et al.*, 2012). A_{NH} is a numerical factor depending on the shape of the grain and the boundary conditions, and in the impossibility of grain boundary sliding at constant stress is equal to 16/3.

In Figure 4.3, a map describing the strain rate for both mechanisms as a function of the grain size is presented.

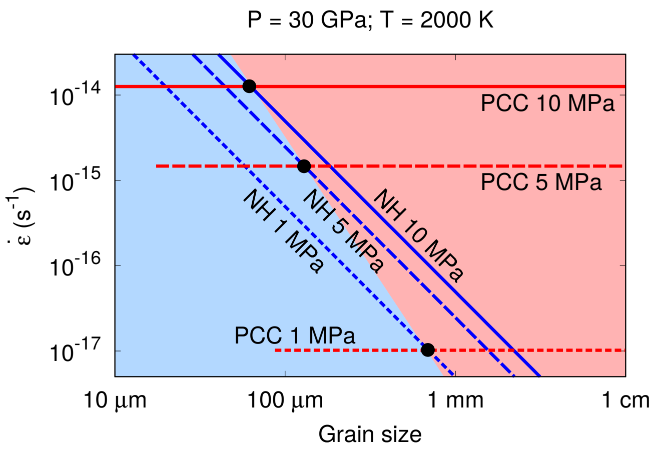

(a)

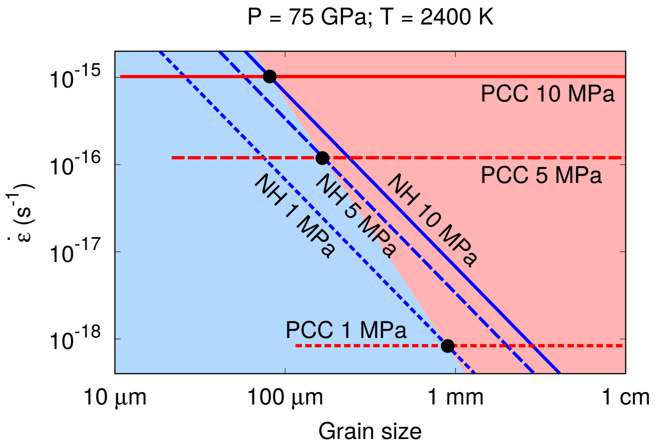

(b)

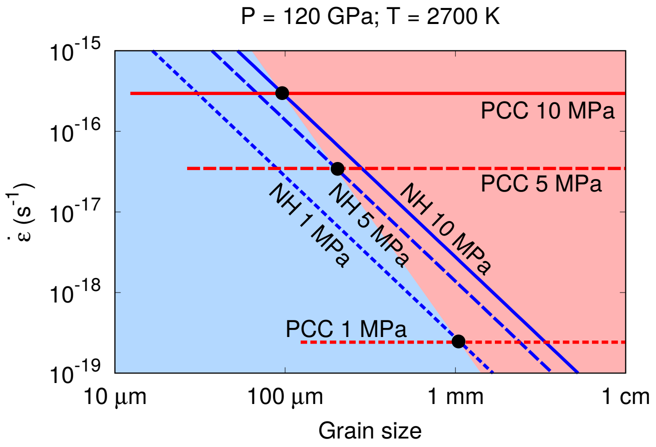

(c)

Figure 4.3: *deformation map (strain rate $\dot{\varepsilon}$ vs. grain size) comparing pure climb creep (PCC) and Nabarro–Herring (NH) mechanisms at 30 GPa and 2000 K (a), 75 GPa and 2400 K (b), 120 GPa and 2700 K (c). PCC dominates in the domain marked in red and NH dominates in the blue region.*

Three stresses (1, 5 and 10 MPa) are considered at given PT conditions along the geotherm (Stacey and Davis, 2004): 30 GPa and 2000 K, corresponding to the upper part of the lower mantle (Figure 4.3a), 75 GPa and 2400 K (Figure 4.3b) and 120 GPa and 2700 K (Figure 4.3c). For each stress, the pure climb creep is represented as a horizontal line since this mechanism is grain–size independent.

The pure climb creep curves of Figure 4.3 exhibit a lower bound because of the existence of a critical stress needed to activate a dislocation source. In climb, dislocation multiplication is made possible by the activation of sources known as Bardeen–Herring sources (Bardeen and Herring, 1952), which are the equivalent for climb as the Frank–Read sources observed in glide. The physics for the opening of both sources, based on the line tension, is equivalent, leading to a critical stress σ_c for opening in the form of:

$$\sigma_c = \frac{\mu b}{l_{c,S}} \tag{4.4}$$

where $l_{c,S}$ is the critical size of the source. Since, for geometrical reasons, $l_{c,S}$ has to be smaller than the grain size, a bound is placed on the pure climb creep regime for the given three values of stress.

The interception of the Nabarro–Herring and pure climb creep curves for the same value of applied stress is marked by a black dot in Figure 4.3. This point identifies the value of grain size for which pure climb creep becomes more efficient than Nabarro–Herring creep, *i.e.*, produces a larger strain rate at the same applied stress. By connecting the different dots marking this transition at different stresses, it is possible to separate the space in different grain size domains where one mechanism is more efficient than the other.

As a result, one can see that above a grain size of 0.1–1 mm, pure climb creep is expected to be the dominant mechanism.

4.4.2 Strain rates and viscosities of bridgmanite

Figure 4.4 shows the strain rates as a function of depth considering extrinsic diffusion of Mg as the rate–limiting factor for climb. The vacancy concentrations X_{v1} and X_{v2}, as discussed above, are set to 10^{-3} and 10^{-6}, respectively.

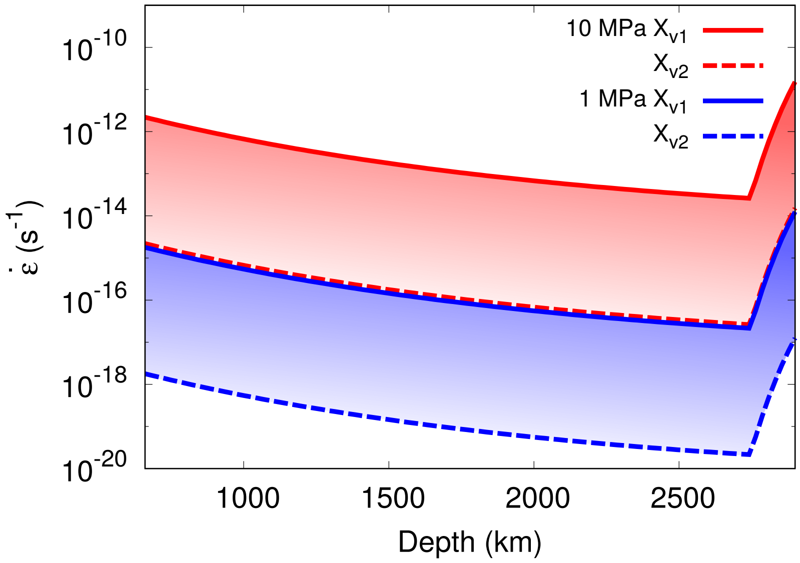

Figure 4.4: *strain rates $\dot{\varepsilon}$ of bridgmanite along the geotherm calculated with the Nabarro (1967) creep model for stresses of 10 (red lines) and 1 (blue lines) MPa and vacancy concentrations of 10^{-3} (solid lines) and 10^{-6} (dashed lines).*

Knowing the strain rates it is possible to calculate the effective viscosity η:

$$\eta = \frac{\sigma}{\dot{\varepsilon}} \tag{3.4}$$

In Figure 4.5 the calculated viscosity is plotted along the geotherm for the same stresses and vacancy concentrations described above.

Figures 4.4 and 4.5 show consistently a steady, monotonic evolution of strain rate and viscosity along the geotherm (Stacey and Davis, 2004) until the marked temperature increase in the boundary layer at the D'' leads to a strong drop (*ca.* 3 log units) of the viscosity of bridgmanite. This simply illustrates the effect of temperature in a thermal boundary layer.

Seismic observations show that this thermal boundary layer is characterized by strong lateral variations, which have been associated with rich thermochemical complexity (Sun and Helmberger, 2008; Cobden *et al.*, 2015) and should be addressed in future studies.

Our focus is on the bulk of the lower mantle, where the conjugate effect of pressure and temperature along the geotherm is relatively modest, leading to an increase of 2 log units from the base of the transition zone to the D'' layer. In comparison, the variability permitted by the range of stresses (1 – 10 MPa) and vacancy concentrations (10^{-6} – 10^{-3}) is much larger: around 5 orders of magnitude.

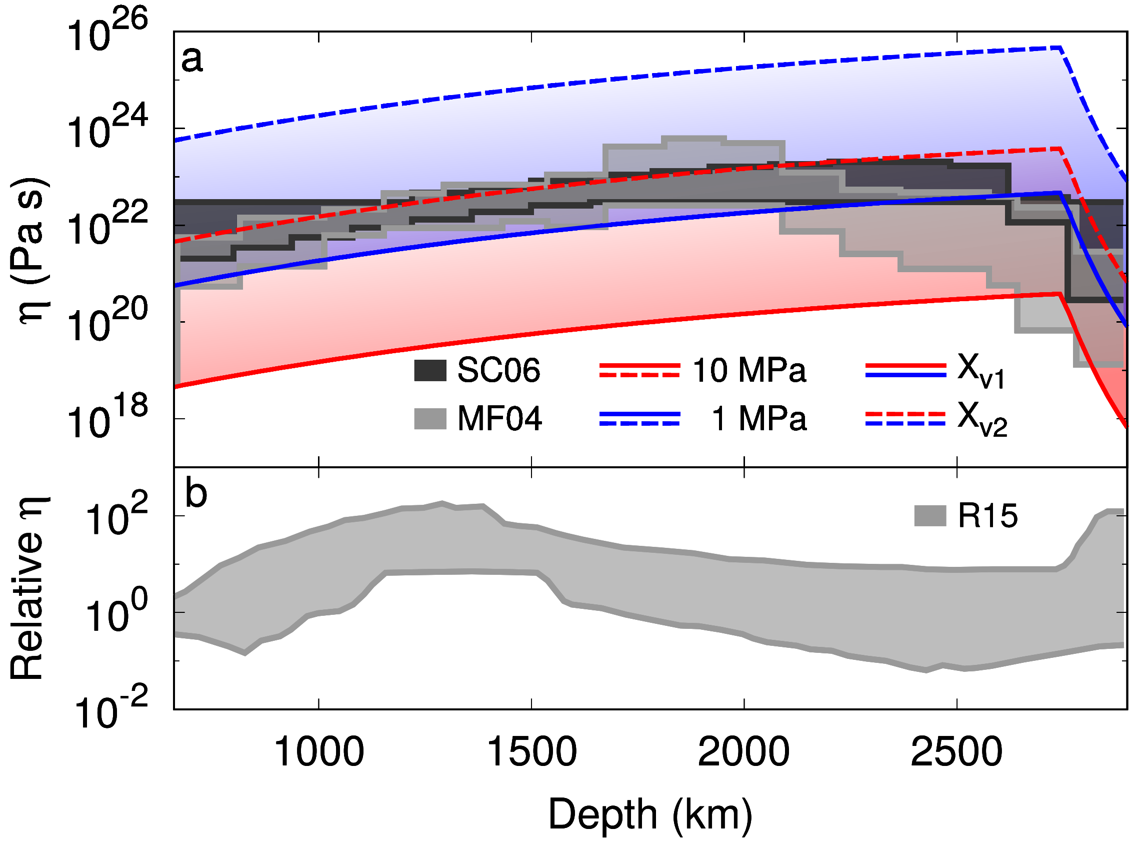

Figure 4.5: *viscosity η of bridgmanite along the geotherm for stresses of 10 MPa (red lines) and 1 MPa (blue lines) and vacancy concentrations of 10^{-3} (solid lines) and 10^{-6} (dashed lines). The obtained absolute values and variability of viscosity are compared with the data of Mitrovica and Forte (2004) (MF04) and Steinberger and Calderwood (2006) (SC06) (a) and with Rudolph et al. (2015) (R15) (b), which are all marked with the gray fillings. The scale on the y axis is the same for the (a) and (b) figures.*

The trend of viscosity across the lower mantle evidenced in Figure 4.5 will be discussed and compared with the available viscosity profiles in the next section. It shall be noted here, however, that this comparison is not meant to explain or approximate the rheology of the entire lower mantle to the one of bridgmanite. On the opposite, it is here attempted to provide a reasonable estimate of bridgmanite viscosity and from it, infer the analogies and differences with the available observables.

Table 4.3 shows the obtained values of strain rate $\dot{\varepsilon}$ and viscosity η at different pressures and temperatures along the geotherm and at the different applied stresses and vacancy concentrations considered for this study.

$X_v = 10^{-3}$, $\sigma = 10$ MPa

P (GPa)	*Depth* (km)	T (K)	$\dot{\varepsilon}$ (s^{-1})	η (Pa·s)
30	809	1992	$1.3 \cdot 10^{-12}$	$7.9 \cdot 10^{18}$
60	1457	2256	$1.9 \cdot 10^{-13}$	$5.1 \cdot 10^{19}$
90	2060	2487	$6.2 \cdot 10^{-14}$	$1.6 \cdot 10^{20}$
120	2617	2689	$3.0 \cdot 10^{-14}$	$3.4 \cdot 10^{20}$

$X_v = 10^{-3}$, $\sigma = 1$ MPa

P (GPa)	*Depth* (km)	T (K)	$\dot{\varepsilon}$ (s^{-1})	η (Pa·s)
30	809	1992	$1.0 \cdot 10^{-15}$	$9.8 \cdot 10^{20}$
60	1457	2256	$1.6 \cdot 10^{-16}$	$6.3 \cdot 10^{21}$
90	2060	2487	$5.1 \cdot 10^{-17}$	$2.0 \cdot 10^{22}$
120	2617	2689	$2.4 \cdot 10^{-17}$	$4.1 \cdot 10^{22}$

$X_v = 10^{-6}$, $\sigma = 10$ MPa

P (GPa)	*Depth* (km)	T (K)	$\dot{\varepsilon}$ (s^{-1})	η (Pa·s)
30	809	1992	$1.3 \cdot 10^{-15}$	$7.9 \cdot 10^{21}$
60	1457	2256	$1.9 \cdot 10^{-16}$	$5.1 \cdot 10^{22}$
90	2060	2487	$6.2 \cdot 10^{-17}$	$1.6 \cdot 10^{22}$
120	2617	2689	$3.0 \cdot 10^{-17}$	$3.4 \cdot 10^{23}$

$X_v = 10^{-6}$, $\sigma = 1$ MPa

P (GPa)	*Depth* (km)	T (K)	$\dot{\varepsilon}$ (s^{-1})	η (Pa·s)
30	809	1992	$1.0 \cdot 10^{-18}$	$9.8 \cdot 10^{23}$
60	1457	2256	$1.6 \cdot 10^{-19}$	$6.3 \cdot 10^{24}$
90	2060	2487	$5.1 \cdot 10^{-20}$	$2.0 \cdot 10^{25}$
120	2617	2689	$2.4 \cdot 10^{-20}$	$4.1 \cdot 10^{25}$

Table 4.3: *Estimate of the strain rates $\dot{\varepsilon}$ and viscosities η at different pressures along the geotherm using the creep model of Nabarro (1967) displayed in equation 1.14. Here the vacancy concentration X_v and the deviatoric stress σ are shown in the titles of each different table.*

4.5 Discussion

It is thus interesting to compare our predictions with some viscosity profiles from the literature.

In Figure 4.5a, a comparison is made with the models of Mitrovica and Forte (2004). It is striking that the monotonic increase of viscosity reported by them mimics very well our prediction down to *ca.* 2000 km depth. The values are also in very good agreement, and it must be noted that despite the wide range of our calculations, they are quite consistent with the viscosity profile of the lower mantle suggested by most geodynamic observables.

In fact, a comparison with the data of Steinberger and Calderwood (2006) confirms this agreement. The depth–dependent viscosity they obtain overlaps with the data of this study over the whole depth range of the lower mantle.

The viscosity decrease reported by Mitrovica and Forte (2004) below 2000 km depth cannot be explained by our model if stress and point defect chemistry (*i.e.* σ and X_v) remain constant. However, this is due to the little constraint that can reasonably be applied to these variables. It is likely that stresses and vacancy concentrations vary continuously throughout the lower mantle and with this in mind, the deviation from the monotonic increase displayed by viscosity profiles can very well be explained through reasonable variations of the parameters considered as constants in this study.

Although they propose a very different view of the viscosity structure of the lower mantle, the results of Rudolph *et al.* (2015) also are consistent with our results (Figure 4.5b). In that case only the variations can be compared since Rudolph *et al.* (2015) propose only relative viscosity profiles. However, one can see on Figure 4.5b that the range of viscosity corresponding to the hill that they propose at 1000 – 1500 km depth can well be described within the variability of our model.

4.6 Perspectives

In a framework where the rheology of the lower mantle is primarily constrained by diffusion, our progress on understanding the viscosity of this region will be controlled by our knowledge of this key parameter. Experimental data on diffusion in bridgmanite are limited, due to the difficulties of performing diffusion experiments at high pressure and also because diffusion appears to be very slow in bridgmanite, making the measurement of diffusion profiles a very challenging task.

Figure 4.5 shows that the viscosity profiles based upon geophysical observations and their variation with depth fall wholly in the range of conditions (stresses, vacancy concentrations) that can be anticipated for the mantle using the present approach.

Furthermore, in the lower mantle, bridgmanite may exhibit radial and lateral variations (at different scales) in chemistry, not captured in PREM (Dziewonski and Anderson, 1981), which may the affect vacancy concentrations, the shear modulus and the diffusivity. In this chapter, we kept the discussion in the very simple framework of a 1D viscosity profile throughout the lower mantle. The lower mantle is, however, expected to present heterogeneities at different scales.

For example, Ballmer *et al.* (2017) have shown that large scale heterogeneities such as the BEAMS (bridgmanite–enriched ancient mantle structures) can survive (and even organize) mantle convection. Such heterogeneities could significantly alter the stress conditions and point defect chemistry of the ambient mantle, and these deviations currently cannot be accounted for in the present formulation. Moreover, Shim *et al.* (2017) suggested that iron partitioning between bridgmanite and ferropericlase could be significantly affected by large changes in the oxidation state of iron in bridgmanite. They proposed a lowering of the total iron content in bridgmanite in the mid–mantle that they relate to viscosity changes through scaling laws such as the homologous temperature relation. Again, a decrease in the total iron content would certainly affect the vacancy concentration, triggering a negative variation of X_v and a consequent increase in viscosity (which is consistent with the conclusions drawn by Shim *et al.*, 2017).

In this context, more detailed predictions could be made by relating chemistry and oxidation state to vacancy concentrations. This would require, among other things, a better understanding of point defect chemistry in bridgmanite. To the best of our knowledge, the only detailed theoretical study of point defect chemistry is the one of Hirsch and Shankland (1991b) for Fe–bearing bridgmanite. It must be recognized that, although much progress has been made on this front, the actual species of iron in bridgmanite (oxidization state, spin state, and associated crystallographic sites) are still not well constrained. Moreover, the study of Hirsch and Shankland (1991b) did not consider the presence of aluminium. Efforts to better understand the point defects that control creep in bridgmanite and their concentrations in the lower mantle should be a priority in the near future.

Chapter 5

Conclusions

5.1 Summary of the obtained results

The present thesis work addresses the creep behavior of bridgmanite and (Mg,Fe)O through different modeling approaches. The strain rates as a function of pressures and temperatures of the lower mantle are retrieved for different applied stresses, compositions and impurity concentrations. An evaluation of viscosity is provided, giving an estimate of this important parameter across the geotherm and at CMB conditions.

Taking place at the end of the ERC–funded RheoMan project, our work benefits from the last developments achieved during the last five years. In particular, the first step of the project consisted in the application of the newly developed 2.5D–DD approach to MgO, in order to reproduce its deformation under different temperature regimes. This technique has been applied to olivine in our group. It gives the unique possibility to take into account simultaneously two deformation mechanisms (dislocation glide and climb) as well as their interplay. At low and intermediate temperatures our results agree with previous numerical (3D–DD) results from Amodeo *et al.* (2014) and experimental evidences, providing a benchmark on the validity of our approach. Having this ground set, it was possible to do a step further and introduce dislocation climb at high temperatures. Results in this regime are in excellent agreement with the available experimental data on high temperature creep of MgO at ambient pressure, confirming that the present numerical tool is capable of reproducing the plastic behavior of this phase under varying conditions and driving mechanisms.

The validated 2.5D–DD approach has then been used to explore the dislocation creep behavior of (Mg,Fe)O ferropericlase and magnesiowüstite at D'' conditions. The implementation of the diffusion coefficients is a critical part of this study. Due to experimental limitations, we lack a direct estimate of these values as a function of temperature, pressure and iron concentration. It was proved that intrinsic oxygen diffusion is the limiting process for diffusion in these compounds and the needed inputs for the code were retrieved through the employment of a homologous temperature relation. This was possible after the estimate of the relevant melting temperatures; since it was proved that this scaling works well for (Mg,Fe)O and other binary oxides.

Upon retrieving the creep strain rates at different temperatures, pressures and applied stresses, we find that the viscosity of magnesiowüstite is reduced by about 10 orders of magnitude at the core–mantle boundary. By exploring the effects of an estimated viscosity contrast of a magnesiowüstite–bearing layer at the CMB, we find that lower concentrations of magnesiowüstite would be required to explain the topographic relief reported in some ULVZ locations.

In the case of bridgmanite, the most recent results (either from numerical modeling or experiments) have demonstrated that dislocation glide is strongly inhibited under mantle pressures, invalidating the possibility of the standard dislocation creep regime observed for (Mg,Fe)O. Alternatively, it has been demonstrated by Francesca Boioli in our group that a pure climb creep mechanism could be a relevant strain–producing mechanism. This was certified by a higher strain–producing efficiency throughout the lower mantle with respect to diffusion creep, if grain sizes greater than 0.1–1 mm were considered. In this thesis, we have further considered the implications of this mechanism on the creep rates of bridgmanite under lower mantle conditions. The strain rates of bridgmanite along a geotherm were evaluated according to the analytical creep model of pure climb originally proposed by F. Nabarro which was shown to be in excellent agreement with the DD simulations. Here, again, the key parameter is represented by diffusion. By anchoring this variable to the available experimental and numerical data it was possible to obtain reasonable estimates of the vacancy concentrations, which were a critical point, given that they were rather unconstrained. The effective viscosities obtained with this approach match the available profiles from the literature.

5.2 Diffusion coefficients: a review

Given the paramount importance of diffusion in creep, our work has led us to make a critical assessment of the literature on this topic. Different diffusion mechanisms have been discussed, such as the fundamental jump process, *i.e.* the vacancy mechanism, the divacancy mechanism or the more complicated jump cycle for Si diffusion in bridgmanite (based on first–principles calculation of the energy barriers). It is not unusual among oxides and silicates to have self–diffusion of major components by an interstitialcy mechanism (*e.g.* in rutile, TiO_2), although a vacancy mechanism seems to be favored in most cases – or at least in the relatively small number of cases where the diffusion mechanism has been clearly established.

Then, there is extrinsic *vs.* intrinsic diffusion, with intrinsic generally referring to the point defects responsible for diffusion (vacancies, in this case) being generated by a purely thermal process, and extrinsic referring to point defect generation by impurities, to maintain charge balance.

5.2.1 (Mg,Fe)O

In (Mg,Fe)O, there is typically a cation deficit due to the presence of Fe^{3+}, Al^{3+}, Cr^{3+}, *etc.* in higher concentrations than Na^{+} (the only major monovalent cation). This leads to extrinsic cation diffusion, and intrinsic oxygen diffusion, as discussed in Chapter 3. Note that it can be the opposite – in synthetic MgO crystals doped with Li, oxygen diffusion is in the extrinsic regime, and is much faster than in nominally pure or X^{3+}–doped MgO. One would expect that cation diffusion takes place in the intrinsic regime in this case, although it hasn't been studied (and might be difficult to measure, since diffusion would be slow, and Li is moderately volatile, meaning that it would be hard to keep Li in the crystals at the temperatures needed to measure cation intrinsic diffusion).

Further complicating the assessment of the oxygen vacancy concentration and oxygen diffusion mechanism is the experimental finding that oxygen diffusion along dislocations (pipe–diffusion) has a similar activation energy (Narayan and Washburn, 1973; Sakaguchi *et al.*, 1992) as mono–vacancy diffusion, as noted by Ammann *et al.* (2010a). This phenomenon has likely been observed by Yang and Flynn (1994; 1996) and maybe also by

Yoo *et al.* (2002) in their low temperature data of oxygen diffusion. At the same time, this might suggest that even the data of Oishi and Kingery (1960) as well as of Shirasaki and Hama (1973) represent pipe–diffusion instead of extrinsic oxygen diffusion.

At high pressures, there is a lack of data on diffusion for this material. Due to this, it is necessary to estimate diffusion coefficients within the mantle using an alternative approach. The homologous relation was proved to be a good proxy for diffusion, but, depending significantly on the melting temperature, there is uncertainty in choosing the liquidus or solidus temperatures, especially if the values have a very large difference. Of second order importance there is also the issue of the accuracy of the phase diagram at high pressures.

On the Fe–rich end of the (Mg,Fe)O solid solution, different melting temperatures were collected in experiments (*cf.* Figure 3.1, where it is shown that the results of Fischer and Campbell (2010) and Kato *et al.* (2016) differ from the finding of Komabayashi (2014)).

There are uncertainties on the MgO melting temperature at high pressures, too (see Fat'yanov and Asimow, 2014; for a recent review). The shapes (functional form) of the liquidus and solidus curves as a function of pressure are also a matter of debate. Knowing better the level of non–ideality of the liquidus–solidus phase loop between MgO and FeO as a function of pressure would permit more reliable estimates on the diffusion coefficients of this solid solution, and thus the viscosity evaluation would gain more constraint.

5.2.2 Bridgmanite

With respect to (Mg,Fe)O, oxygen diffusion in bridgmanite and (Mg,Fe)O occurs by the same mechanism (vacancy) but the minerals tend to incorporate aliovalent cations differently.

For bridgmanite, there are two cationic sites, and it seems that there is likely to be an excess of them on the Si site, leading to an oxygen deficit (rather than a cation deficit, as is the usual case for (Mg,Fe)O). This explains the experimental evidence of faster diffusion for oxygen with respect to cations. It should be possible to reverse this, for example by doping bridgmanite with species like Sc^{3+}, which is too large to occupy the Si site. A major question that remains with bridgmanite, constituting an important unanswered problem, is why cationic diffusion seems to be extrinsic and not intrinsic. We showed in Chapter 4 that the latter does not give rise to vacancy concentrations capable of rendering intrinsic diffusion a viable mechanism for bridgmanite, because the retrieved values were simply not meaningful with respect to the deformation timescale of the Earth. From the data collected in experiments and numerical simulation, on the other hand, the obtained vacancy concentrations mirrored the ones of extrinsic diffusion. Theoretically, based on simple chemical mass action arguments (Hirsch and Shankland, 1991c), it should not be possible to have extrinsic diffusion by a vacancy mechanism on both cation and anion sublattices simultaneously. It should be one or the other. It would be possible in theory to have extrinsic oxygen vacancy diffusion and extrinsic cationic interstitial diffusion. This is because an oxygen deficit promotes both oxygen vacancies and cationic interstitials. However, this doesn't seem viable for bridgmanite, because the cationic interstitial formation energies appear to be too large. It could even be possible that the dislocation core diffusion process mentioned in the previous section may be occurring in bridgmanite, too.

This is an open point which shall promote new studies on the assessment of diffusion in bridgmanite, in order to better comprehend this phenomenon which is majorly important for a better understanding of the creep properties of this mineral.

5.3 Perspectives

The results of this thesis work provide the estimate of viscosity of bridgmanite and (Mg,Fe)O starting for the steady–state creep strain rates at lower mantle PT conditions. In particular, at the lower end of the mantle it is possible to plot together the results for these two phases, providing a compilation of creep laws which reproduce well the behavior of pure climb in the case of bridgmanite and dislocation creep modeled through DD for (Mg,Fe)O.

In Figure 5.1 the obtained creep data are shown at 120 GPa, 2800K and 135 GPa, 3800 K. At conditions close to the geotherm (Figure 5.1a) ferropericlase shows a stiffer rheology than bridgmanite while at the CMB (Figure 5.1b), interestingly, ferropericlase strength matches the one of bridgmanite in the case of low vacancy concentration.

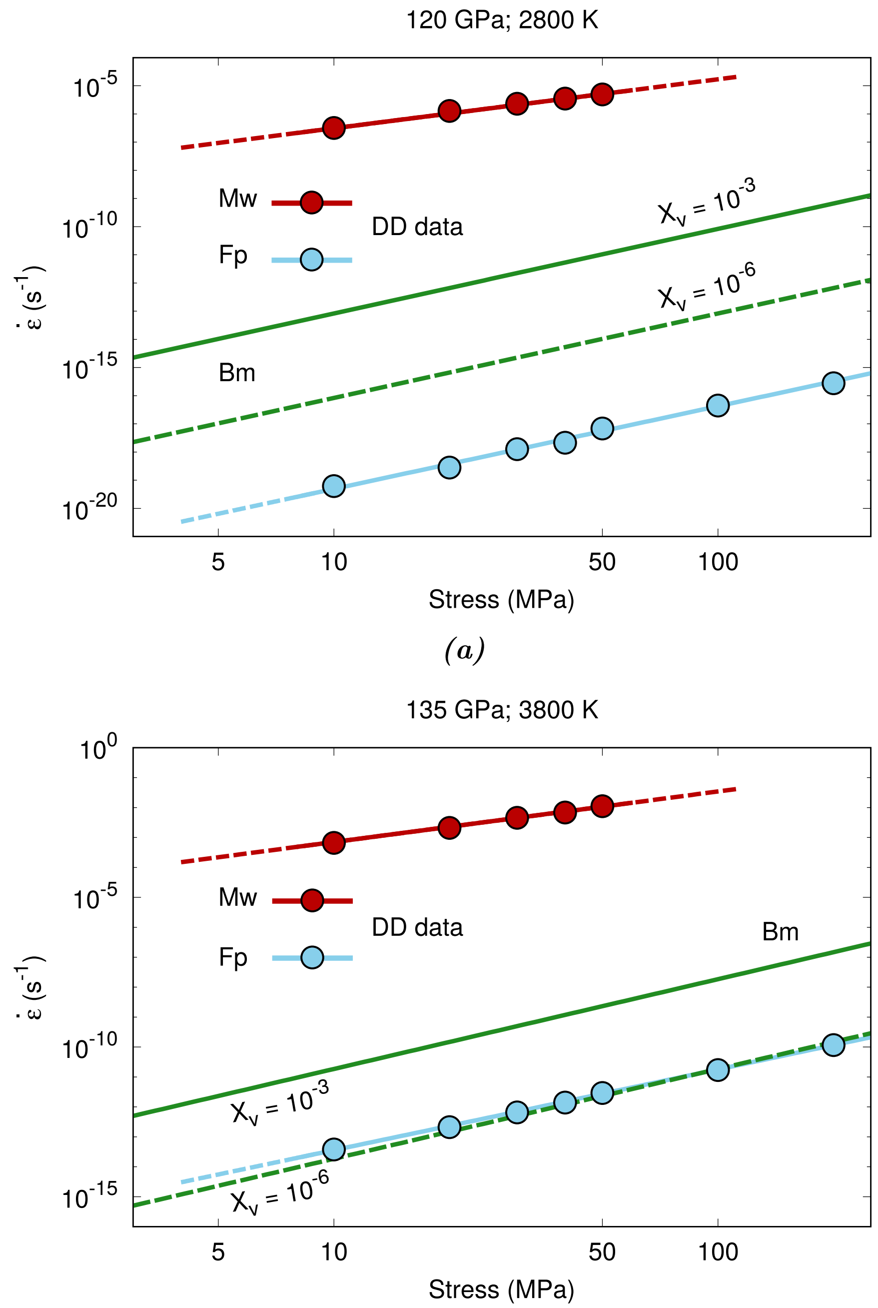

(a)

(b)

Figure 5.1: *(Mg,Fe)O ferropericlase (Fp) and magnesiowüstite (Mw) results from 2.5D–DD simulations and related power law fit equations are compared with the pure climb creep rates of bridgmanite (Bm) at different vacancy concentrations $X_{v1,2}$. The PT conditions resemble the geotherm at 2800 K and 120 GPa (a) and CMB conditions at 3800 K and 135 GPa (b).*

If supported by other evidences, this could be a major implication of the present work. In fact, in principle the general consensus leans towards the opposite case, where ferropericlase is considered the weak phase (Yamazaki and Karato, 2001). This is supported by experimental results (*i.e.* Girard *et al.*, 2015) that, as it is unavoidable, are not run at strain rates relevant for the lower mantle and therefore cannot fully reproduce and capture the set of conditions at which the viscous flow takes place. The present results indicate that ferropericlase is stronger if not equivalent to bridgmanite in terms of strain rate efficiency and this new strength relation would severely affect the viscous deformation of these phases and the related rheology of the aggregate.

Such an inversion in the strength ratio between ferropericlase and bridgmanite is the foremost implication of this work and calls for more investigations in this sense.

As mentioned above, the melting temperature has a key role in the estimate of ferropericlase strain rates. Given that the T/T_m ratio for this phase was low (down to 0.4, *cf.* Table 3.3 of Chapter 3), the uncertainties mentioned for T_m itself and for the liquidus–solidus shape curves are likely to be even more relevant in this case. Again, more refinement from further studies shall be of help in improving the precision of these predictions, for which the validity of the approach was demonstrated accurately.

These results allow for further developments, because, now that a rheology law is provided for each phase and a hierarchy of strength is established, they could serve as inputs in order to assess the properties of aggregates at greater scales. In particular, scale–transition models could provide insights on the behavior of a crystalline aggregate containing different amounts of these minerals, contributing for other, unified power laws characterizing these polycrystals. Also, these power laws could feed finite elements numerical techniques, which have the potentiality of describing the behavior of aggregates having an interconnected or non–interconnected network of (Mg,Fe)O crystals. Being of relevant importance for the rheology of the lower mantle, these different network configurations may provide some more constraints on viscosity, too.

Furthermore, the bridgmanite and (Mg,Fe)O creep models provide a non–linear rheology for these phases, and it shall be of interest to see how this different stress–strain rate relationships affect the output of global geodynamic models. In the case of bridgmanite, an investigation of the influence of lateral variations of temperature within the Earth's mantle may show the importance of thermal anomalies in terms of viscosity contrast and help explaining the non–monotonic viscosity trends displayed by the observable profiles.

Bibliography

Alfe, D. and Gillan, M.J. Schottky defect formation energy in MgO calculated by diffusion Monte Carlo. *Physical Review B*, 71(22):220101, 2005. doi: 10.1103/PhysRevB.71.220101.

Ammann, M.W., Brodholt, J.P., and Dobson, D.P. DFT study of migration enthalpies in $MgSiO_3$ perovskite. *Physics and Chemistry of Minerals*, 36(3):151–158, 2009. doi: 10.1007/s00269-008-0265-z.

Ammann, M.W., Brodholt, J.P., and Dobson, D.P. Simulating diffusion. *Reviews in Mineralogy and Geochemistry*, 71(1):201–224, 2010a. doi: 10.2138/rmg.2010.71.10.

Ammann, M.W., Brodholt, J.P., Wookey, J., and Dobson, D.P. First–principles constraints on diffusion in lower–mantle minerals and a weak D'' layer. *Nature*, 465(7297):462–465, 2010b. doi: 10.1038/nature09052.

Amodeo, J., Carrez, P., Devincre, B., and Cordier, P. Multiscale modelling of MgO plasticity. *Acta Materialia*, 59(6):2291–2301, 2011. doi: 10.1016/j.actamat.2010.12.020.

Amodeo, J., Carrez, P., and Cordier, P. Modelling the effect of pressure on the critical shear stress of MgO single crystals. *Philosophical Magazine*, 92(12):1523–1541, 2012. doi: 10.1080/14786435.2011.652689.

Amodeo, J., Devincre, B., Carrez, P., and Cordier, P. Dislocation reactions, plastic anisotropy and forest strengthening in MgO at high temperature. *Mechanics of Materials*, 71:62–73, 2014. doi: 10.1016/j.mechmat.2014.01.001.

Amodeo, J., Dancette, S., and Delannay, L. Atomistically–informed crystal plasticity in MgO polycrystals under pressure. *International Journal of Plasticity*, 82:177–191, 2016. doi: 10.1016/j.ijplas.2016.03.004.

Ando, K., Kurokawa, Y., and Oishi, Y. Oxygen self–diffusion in Fe-doped MgO single crystals. *The Journal of chemical physics*, 78(11):6890–6892, 1983. doi: 10.1063/1.444635.

Andrade, E.N. Da C. On the viscous flow in metals, and allied phenomena. *Proceedings of the Royal Society of London A*, 84(567):1–12, 1910. doi: 10.1098/rspa.1910.0050.

Andrault, D., Pesce, G., Bouhifd, M.A., Bolfan-Casanova, N., Hénot, J.-M., and Mezouar, M. Melting of subducted basalt at the core–mantle boundary. *Science*, 344(6186):892–895, 2014. doi: 10.1126/science.1250466.

Appel, F. and Wielke, B. Low temperature deformation of impure MgO single crystals. *Materials science and engineering*, 73:97–103, 1985. doi: 10.1016/0025-5416(85)90299-X.

Arsenlis, A., Cai, W., Tang, M., Rhee, M., Oppelstrup, T., Hommes, G., Pierce, T.G., and Bulatov, V.V. Enabling strain hardening simulations with dislocation dynamics. *Modelling and Simulation in Materials Science and Engineering*, 15(6):553, 2007. doi: 10.1088/0965-0393/15/6/001.

Atkins, A.G. and Tabor, D. Mutual Indentation Hardness of Single–Crystal Magnesium Oxide at High Temperatures. *Journal of the American Ceramic Society*, 50(4):195–198, 1967. doi: 10.1111/j.1151-2916.1967.tb15079.x.

Badro, J., Fiquet, G., Guyot, F., Rueff, J.-P., Struzhkin, V.V., Vankó, G., and Monaco, G. Iron partitioning in Earth's mantle: toward a deep lower mantle discontinuity. *Science*, 300(5620):789–791, 2003. doi: 10.1126/science.1081311.

Ballmer, M.D., Schmerr, N.C., Nakagawa, T., and Ritsema, J. Compositional mantle layering revealed by slab stagnation at ˜1000–km depth. *Science advances*, 1(11):e1500815, 2015. doi: 10.1126/sciadv.1500815.

Ballmer, M.D., Houser, C., Hernlund, J.W., Wentzcovitch, R.M., and Hirose, K. Persistence of strong silica–enriched domains in the Earth's lower mantle. *Nature Geoscience*, 10(3):236, 2017. doi: 10.1038/ngeo2898.

Bardeen, J. and Herring, C. *Imperfections in nearly perfect crystals*, chapter Diffusion in alloys and the Kirkendall effect, page 261. Weiley, New York, 1952.

Barr, L.W., Morrison, J.A., and Schroeder, P.A. Anion Diffusion in Crystals of NaCl. *Journal of Applied Physics*, 36(2):624–631, 1965. doi: 10.1063/1.1714040.

Barthel, C. *Plastiche anisotropie von Bleisulfid und magnesiumoxid*. PhD thesis, University of Gottingen, 1984.

Basinski, S.J. and Basinski, Z.S. Plastic deformation and work hardening. *Dislocations in solids*, 4:261–362, 1980.

Beauchesne, S. and Poirier, J.P. Creep of barium titanate perovskite: a contribution to a systematic approach to the viscosity of the lower mantle. *Physics of the earth and planetary interiors*, 55(1-2):187–199, 1989. doi: 10.1016/0031-9201(89)90242-2.

Beauchesne, S. and Poirier, J.P. In search of a systematics for the viscosity of perovskites: creep of potassium tantalate and niobate. *Physics of the earth and planetary interiors*, 61(3-4):182–198, 1990. doi: 10.1016/0031-9201(90)90105-7.

Benzerga, A.A., Bréchet, Y., Needleman, A., and Van der Giessen, E. Incorporating three–dimensional mechanisms into two–dimensional dislocation dynamics. *Modelling and Simulation in Materials Science and Engineering*, 12(1):159, 2003. doi: 10.1088/0965-0393/12/3/C01.

Bilde-Sörensen, J.B. Dislocation Structures in Creep–Deformed Polycrystalline MgO. *Journal of the American Ceramic Society*, 55(12):606–610, 1972. doi: 10.1111/j.1151-2916.1972.tb13453.x.

Boioli, F., Carrez, P., Cordier, P., Devincre, B., and Marquille, M. Modeling the creep properties of olivine by 2.5–dimensional dislocation dynamics simulations. *Physical Review B*, 92(1):014115, 2015a. doi: 10.1103/PhysRevB.92.014115.

Boioli, F., Tommasi, A., Cordier, P., Demouchy, S., and Mussi, A. Low steady–state stresses in the cold lithospheric mantle inferred from dislocation dynamics models of dislocation creep in olivine. *Earth and Planetary Science Letters*, 432:232–242, 2015b. doi: 10.1016/j.epsl.2015.10.012.

Boioli, F., Carrez, P., Cordier, P., Devincre, B., Gouriet, K., Hirel, P., Kraych, A., and Ritterbex, S.A.W. Pure climb creep mechanism drives flow in Earth's lower mantle. *Science advances*, 3(3):e1601958, 2017. doi: 10.1126/sciadv.1601958.

Bower, D.J., Wicks, J.K., Gurnis, M., and Jackson, J.M. A geodynamic and mineral physics model of a solid–state ultralow–velocity zone. *Earth and Planetary Science Letters*, 303(3-4):193–202, 2011. doi: 10.1016/j.epsl.2010.12.035.

Brown, J.M. and Shankland, T.J. Thermodynamic parameters in the Earth as determined from seismic profiles. *Geophysical Journal International*, 66(3):579–596, 1981. doi: 10.1111/j.1365-246X.1981.tb04891.x.

Buchbinder, G.G.R. and Poupinet, G. Problems related to *PcP* and the core–mantle boundary illustrated by two nuclear events. *Bulletin of the Seismological Society of America*, 63(6-1):2047–2070, 1973. URL `https://pubs.geoscienceworld.org/ssa/bssa/article-abstract/63/6-1/2047/117286`.

Bullen, K.E. An earth model based on a compressibility–pressure hypothesis. *Geophysical Journal International*, 6:50–59, 1950. doi: 10.1111/j.1365-246X.1950.tb02973.x.

Bunge, H.-P., Richards, M.A., and Baumgardner, J.R. Effect of depth–dependent viscosity on the planform of mantle convection. *Nature*, 379(6564):436, 1996. doi: 10.1038/379436a0.

Bunge, H.P. and Richards, M.A. The origin of large scale structure in mantle convection: Effects of plate motions and viscosity stratification. *Geophysical Research Letters*, 23 (21):2987–2990, 1996. doi: 10.1029/96GL02522.

Burgers, J.M. Some considerations on the fields of stress connected with dislocations in a regular crystal lattice. I. In *Selected Papers of J.M. Burgers*, pages 335–389. Springer, 1939.

Butterworth, N.P., Müller, R.D., Quevedo, L., O'Connor, J.M., Hoernle, K., and Morra, G. Pacific plate slab pull and intraplate deformation in the early Cenozoic. *Solid Earth*, 5(2):757–777, 2014. doi: 10.5194/se-5-757-2014.

Caillard, D. and Martin, J. *Thermally activated mechanisms in crystal plasticity*, volume 8. Elsevier, 2003.

Carrez, P., Cordier, P., Devincre, B., and Kubin, L.P. Dislocation reactions and junctions in MgO. *Materials Science and Engineering: A*, 400:325–328, 2005. doi: 10.1016/j.msea.2005.03.071.

Carrez, P., Ferré, D., and Cordier, P. Implications for plastic flow in the deep mantle from modelling dislocations in $MgSiO_3$ minerals. *Nature*, 446(7131):68–70, 2007. doi: 10.1038/nature05593.

Chen, W.K. and Jackson, R.A. Oxygen self–diffusion in undoped and doped cobaltous oxide. *Journal of Physics and Chemistry of Solids*, 30(6):1309–1314, 1969. ISSN 0022-3697. doi: https://doi.org/10.1016/0022-3697(69)90192-9.

Clauer, A.H. and Wilcox, B.A. High temperature tensile creep of magnesium oxide single crystals. *Journal of the American Ceramic Society*, 59(3-4):89–96, 1976. doi: 10.1111/j.1151-2916.1976.tb09438.x.

Cobden, L. and Thomas, C. The origin of D'' reflections: a systematic study of seismic array data sets. *Geophysical Journal International*, 194(2):1091–1118, 2013. doi: 10.1093/gji/ggt152.

Cobden, L., Thomas, C., and Trampert, J. Seismic detection of post-perovskite inside the earth. In Khan, A. and Deschamps, F., editors, *The Earth's Heterogeneous Mantle*, pages 391–440. Springer, 2015. doi: 10.1007/978-3-319-15627-9_13.

Coble, R.L. A Model for Boundary Diffusion Controlled Creep in Polycrystalline Materials. *Journal of Applied Physics*, 34(6):1679–1682, 1963. doi: 10.1063/1.1702656.

Cohen, R.E. and Weitz, J.S. The melting curve and premelting of MgO. *Geophysical Monograph Series*, 101:185–196, 1998. doi: 10.1029/GM101p0185.

Cordier, P., Ungár, T., Zsoldos, L., and Tichy, G. Dislocation creep in $MgSiO_3$ perovskite at conditions of the Earth's uppermost lower mantle. *Nature*, 428(6985):837–840, 2004. doi: 10.1038/nature02472.

Cordier, P., Amodeo, J., and Carrez, P. Modelling the rheology of MgO under Earth's mantle pressure, temperature and strain rates. *Nature*, 481(7380):177–180, 2012. doi: 10.1038/nature10687.

Cummerow, R.L. High–Temperature Steady–State Creep Rate in Single–Crystal MgO. *Journal of Applied Physics*, 34(6):1724–1729, 1963. doi: 10.1063/1.1702668.

Davies, D.R., Goes, S., and Sambridge, M. On the relationship between volcanic hotspot locations, the reconstructed eruption sites of large igneous provinces and deep mantle seismic structure. *Earth and Planetary Science Letters*, 411:121–130, 2015. doi: 10.1016/j.epsl.2014.11.052.

Davoudi, K.M., Nicola, L., and Vlassak, J.J. Dislocation climb in two–dimensional discrete dislocation dynamics. *Journal of Applied Physics*, 111(10):103522, 2012. doi: 10.1063/1.4718432.

Deng, J. and Lee, K.K.M. Viscosity jump in the lower mantle inferred from melting curves of ferropericlase. *Nature communications*, 8(1):1997, 2017. doi: 10.1038/s41467-017-02263-z.

Deschamps, F., Li, Y., and Tackley, P.J. Large–Scale Thermo–chemical Structure of the Deep Mantle: Observations and Models. In Khan, A. and Deschamps, F., editors, *The Earth's Heterogeneous Mantle*, pages 479–515. Springer Geophysics, 2015. doi: 10.1007/978-3-319-15627-9_15.

Devincre, B., Kubin, L.P., and Hoc, T. Physical analyses of crystal plasticity by DD simulations. *Scripta Materialia*, 54(5):741–746, 2006. doi: 10.2138/am.2007.2512.

Devincre, B., Madec, R., Monnet, G., Queyreau, S., Gatti, R., and Kubin, L.P. *Mechanics of Nano-objects*. Ecole des Mines de Paris, 2011.

Dobson, D. Oxygen ionic conduction in $MgSiO_3$ perovskite. *Physics of the Earth and Planetary Interiors*, 139(1-2):55–64, 2003. doi: 10.1016/S0031-9201(03)00144-4.

Dobson, D.P., Dohmen, R., and Wiedenbeck, M. Self–diffusion of oxygen and silicon in $MgSiO_3$ perovskite. *Earth and Planetary Science Letters*, 270(1-2):125–129, 2008. doi: 10.1016/j.epsl.2008.03.029.

Dorfman, S.M. and Duffy, T.S. Effect of Fe–enrichment on seismic properties of perovskite and post–perovskite in the deep lower mantle. *Geophysical Journal International*, 197 (2):910–919, 2014. doi: 10.1093/gji/ggu045.

Dorn, J.E. Some fundamental experiments on high temperature creep. *Journal of the Mechanics and Physics of Solids*, 3(2):85–116, 1955. doi: 10.1016/0022-5096(55)90054-5.

Du, Z. and Lee, K.K.M. High–pressure melting of MgO from (Mg,Fe)O solid solutions. *Geophysical Research Letters*, 41(22):8061–8066, 2014. doi: 10.1002/2014GL061954.

Durinck, J., Devincre, B., Kubin, L.P., and Cordier, P. Modeling the plastic deformation of olivine by dislocation dynamics simulations. *American Mineralogist*, 92(8–9):1346–1357, 2007. doi: 10.2138/am.2007.2512.

Dziewonski, A.M. and Anderson, D.L. Preliminary reference Earth model. *Physics of the Earth and Planetary Interiors*, 25(4):297–356, 1981. doi: 10.1016/0031-9201(81)90046-7.

Fat'yanov, O.V. and Asimow, P.D. MgO melting curve constraints from shock temperature and rarefaction overtake measurements in samples preheated to 2300 K. *Journal of Physics: Conference Series*, 500(6):062003, 2014. doi: 10.1088/1742-6596/500/6/062003.

Ferré, D., Carrez, P., and Cordier, P. First principles determination of dislocations properties of $MgSiO_3$ perovskite at 30 GPa based on the Peierls–Nabarro model. *Physics of the Earth and Planetary Interiors*, 163(1-4):283–291, 2007. doi: 10.1016/j.pepi.2007.05.011.

Finkelstein, G.J., Jackson, J.M., Said, A., Alatas, A., Leu, B.M., Sturhahn, W., and Toellner, T.S. Strongly Anisotropic Magnesiowüstite in Earth's Lower Mantle. *Journal of Geophysical Research: Solid Earth*, 2018. doi: 10.1029/2017JB015349.

Fiquet, G., Andrault, D., Dewaele, A., Charpin, T., Kunz, M., and Haüsermann, D. P–V–T equation of state of $MgSiO_3$ perovskite. *Physics of the Earth and Planetary Interiors*, 105(1):21–31, 1998. doi: 10.1016/S0031-9201(97)00077-0.

Fiquet, G., Dewaele, A., Andrault, D., Kunz, M., and Le Bihan, T. Thermoelastic properties and crystal structure of $MgSiO_3$ perovskite at lower mantle pressure and temperature conditions. *Geophysical Research Letters*, 27(1):21–24, 2000. doi: 10.1029/1999GL008397.

Fiquet, G., Auzende, A.L., Siebert, J., Corgne, A., Bureau, H., Ozawa, H., and Garbarino, G. Melting of peridotite to 140 gigapascals. *Science*, 329(5998):1516–1518, 2010. doi: 10.1126/science.1192448.

Fischer, R.A. and Campbell, A.J. High–pressure melting of wustite. *American Mineralogist*, 95(10):1473–1477, 2010. doi: 10.2138/am.2010.3463.

Fischer, R.A., Campbell, A.J., Shofner, G.A., Lord, O.T., Dera, P., and Prakapenka, V.B. Equation of state and phase diagram of FeO. *Earth and Planetary Science Letters*, 304 (3-4):496–502, 2011. doi: 10.1016/j.epsl.2011.02.025.

Foitzik, A., Skrotzki, W., and Haasen, P. Correlation between microstructure, dislocation dissociation and plastic anisotropy in ionic crystals. *Materials Science and Engineering: A*, 113:399–407, 1989. doi: 10.1016/0921-5093(89)90326-2.

Forte, A.M. and Mitrovica, J.X. New inferences of mantle viscosity from joint inversion of long–wavelength mantle convection and post–glacial rebound data. *Geophysical Research Letters*, 23(10):1147–1150, 1996. doi: 10.1029/96GL00964.

Forte, A.M. and Mitrovica, J.X. Deep–mantle high–viscosity flow and thermochemical structure inferred from seismic and geodynamic data. *Nature*, 410(6832):1049, 2001. doi: 10.1038/35074000.

Frost, D.A., Garnero, E.J., and Rost, S. Dynamical links between small–and large–scale mantle heterogeneity: Seismological evidence. *Earth and Planetary Science Letters*, 482:135–146, 2018. doi: 10.1016/j.epsl.2017.10.058.

Fuller, R.G. Diffusion of the Chlorine Ion in Potassium Chloride. *Physical Review*, 142: 524–529, 1966. doi: 10.1103/PhysRev.142.524.

Garnero, E.J. and Helmberger, D.V. A very slow basal layer underlying large–scale low–velocity anomalies in the lower mantle beneath the Pacific: evidence from core phases. *Physics of the Earth and Planetary Interiors*, 91(1):161–176, 1995. doi: 10.1016/0031-9201(95)03039-Y.

Gassner, A., Thomas, C., Krüger, F., and Weber, M. Probing the core–mantle boundary beneath Europe and Western Eurasia: A detailed study using PcP. *Physics of the Earth and Planetary Interiors*, 246:9–24, 2015. doi: 10.1016/j.pepi.2015.06.007.

Girard, J., Amulele, G., Farla, R., Mohiuddin, A., and Karato, S.-i. Shear deformation of bridgmanite and magnesiowüstite aggregates at lower mantle conditions. *Science*, 351 (6269):144–147, 2015. doi: 10.1126/science.aad3113.

Glišović, P., Forte, A.M., and Ammann, M.W. Variations in grain size and viscosity based on vacancy diffusion in minerals, seismic tomography, and geodynamically inferred mantle rheology. *Geophysical Research Letters*, 42(15):6278–6286, 2015. doi: 10.1002/2015GL065142.

Gómez-García, D., Devincre, B., and Kubin, L.P. Forest hardening and boundary conditions in 2–d simulations of dislocations dynamics. *MRS Proceedings*, 578:131, 1999. doi: 10.1557/PROC-578-131.

Gómez-García, D., Devincre, B., and Kubin, L.P. Dislocation patterns and the similitude principle: 2.5 D mesoscale simulations. *Physical review letters*, 96(12):125503, 2006. doi: 10.1103/PhysRevLett.96.125503.

Goryaeva, A.M. *Modeling defects and plasticity in* $MgSiO_3$ *post–perovskite at the atomic scale*. PhD thesis, Université de Lille, 2016.

Gouriet, K., Carrez, P., and Cordier, P. Modelling [100] and [010] screw dislocations in $MgSiO_3$ perovskite based on the Peierls–Nabarro–Galerkin model. *Modelling and Simulation in Materials Science and Engineering*, 22(2):025020, 2014. doi: 10.1088/0965-0393/22/2/025020.

Gutenberg, B. Ueber erdbebenwellen. vii a. beobachtungen an registrierungen von fernbeben in göttingen und folgerung über die konstitution des erdkörpers (mit tafel). *Nachrichten von der Gesellschaft der Wissenschaften zu Göttingen, Mathematisch-Physikalische Klasse*, 1914:125–176, 1914.

Haasen, P., Barthel, C., and Suzuki, T. *Choice of slip system and Peierls stresses in the NaCl structure*, pages 455–462. University of Tokyo Press, 1985.

Hager, B.H. and Richards, M.A. Long–wavelength variations in Earth's geoid: physical models and dynamical implications. *Philosophical Transactions of the Royal Society of London A*, 328(1599):309–327, 1989. doi: 10.1098/rsta.1989.0038.

Harper, J. and Dorn, J.E. Viscous creep of aluminum near its melting temperature. *Acta Metallurgica*, 5(11):654–665, 1957. doi: 10.1016/0001-6160(57)90112-8.

Haskell, N.A. The motion of a viscous fluid under a surface load. *Physics*, 6(8):265–269, 1935. doi: 10.1063/1.1745329.

Heidelbach, F., Stretton, I., Langenhorst, F., and Mackwell, S. Fabric evolution during high shear strain deformation of magnesiowüstite $(Mg_{0.8}Fe_{0.2})O$. *Journal of Geophysical Research: Solid Earth*, 108(B3):2154, 2003. doi: 10.1029/2001JB001632.

Hensler, J.H. and Cullen, G.V. Stress, temperature, and strain rate in creep of magnesium oxide. *Journal of the American Ceramic Society*, 51(10):557–559, 1968. doi: 10.1111/j.1151-2916.1968.tb13321.x.

Hernlund, J.W. and Jellinek, A.M. Dynamics and structure of a stirred partially molten ultralow–velocity zone. *Earth and Planetary Science Letters*, 296(1-2):1–8, 2010. doi: 10.1016/j.epsl.2010.04.027.

Hernlund, J.W. and Tackley, P.J. Some dynamical consequences of partial melting in Earth's deep mantle. *Physics of the Earth and Planetary Interiors*, 162(1-2):149–163, 2007. doi: 10.1016/j.pepi.2007.04.005.

Herring, C. Diffusional Viscosity of a Polycrystalline Solid. *Journal of Applied Physics*, 21(5):437–445, 1950. doi: 10.1063/1.1699681.

Herring, C. Surface tension as a motivation for sintering. *The physics of powder metallurgy*, 27(2):143–179, 1951.

Hirel, P., Kraych, A., Carrez, P., and Cordier, P. Atomic core structure and mobility of [100](010) and [010](100) dislocations in $MgSiO_3$ perovskite. *Acta Materialia*, 79: 117–125, 2014. doi: 10.1016/j.actamat.2014.07.001.

Hirel, P., Carrez, P., Clouet, E., and Cordier, P. The electric charge and climb of edge dislocations in perovskite oxides: The case of high–pressure $MgSiO_3$ bridgmanite. *Acta Materialia*, 106:313–321, 2016a. doi: 10.1016/j.actamat.2016.01.019.

Hirel, P., Carrez, P., and Cordier, P. From glissile to sessile: Effect of temperature on $\langle 110\rangle$ dislocations in perovskite materials. *Scripta Materialia*, 120:67–70, 2016b. doi: 10.1016/j.scriptamat.2016.04.001.

Hirsch, L.M. and Shankland, T.J. Equilibrium point defect concentrations in MgO: Understanding the mechanisms of conduction and diffusion and the role of Fe impurities. *Journal of Geophysical Research: Solid Earth*, 96(B1):385–403, 1991a. doi: 10.1029/90JB02175.

Hirsch, L.M. and Shankland, T.J. Point defects in $(Mg,Fe)SiO_3$ perovskite. *Geophysical Research Letters*, 18(7):1305–1308, 1991b. doi: 10.1029/91GL01582.

Hirsch, L.M. and Shankland, T.J. Determination of defect equilibria in minerals. *Journal of Geophysical Research: Solid Earth*, 96(B1):377–384, 1991c. doi: 10.1029/90JB02176.

Hirth, J.P. and Lothe, J. *Theory of dislocations.* John Wiley\& Sons, 1982.

Hull, D. and Bacon, D.J. *Introduction to dislocations.* Butterworth–Heinemann, 2001.

Hulse, C.O. and Pask, J.A. Mechanical Properties of Magnesia Single Crystals in Compression. *Journal of American Ceramic Society*, 43:373–378, 1960. doi: 10.1177/058310248001200917.

Hutko, A.R., Lay, T., and Revenaugh, J. Localized double–array stacking analysis of PcP: D'' and ULVZ structure beneath the Cocos plate, Mexico, central Pacific, and north Pacific. *Physics of the Earth and Planetary Interiors*, 173(1):60–74, 2009. doi: 10.1016/j.pepi.2008.11.003.

Immoor, J., Marquardt, H., Miyagi, L., Lin, F., Speziale, S., Merkel, S., Buchen, J., Kurnosov, A., and Liermann, H.-P. Evidence for {100}<011> slip in ferropericlase in Earth's lower mantle from high–pressure/high–temperature experiments. *Earth and Planetary Science Letters*, 489(489):251–257, 2018. doi: https://doi.org/10.1016/j.epsl.2018.02.045.

Irifune, T. Absence of an aluminous phase in the upper part of the Earth's lower mantle. *Nature*, 370(6485):131–133, 1994. doi: 10.1038/370131a0.

Islam, M.S. Ionic transport in ABO_3 perovskite oxides: a computer modelling tour. *Journal of Materials chemistry*, 10(4):1027–1038, 2000. doi: 10.1039/A908425H.

Ita, J. and Cohen, R.E. Effects of pressure on diffusion and vacancy formation in MgO from nonempirical free–energy integrations. *Physical Review Letters*, 79(17):3198, 1997. doi: 10.1103/PhysRevLett.79.3198.

Kanamori, H. Spectrum of P and PcP in relation to the mantle–core boundary and attenuation in the mantle. *Journal of Geophysical Research*, 72(2):559–571, 1967. doi: 10.1029/JZ072i002p00559.

Karato, S.-i. and Li, P. Diffusion Creep in Perovskite: Implications for the Rheology of the Lower Mantle. *Science*, 255(5049):1238–1240, 1992. doi: 10.1126/science.255.5049.1238.

Karato, S.-i., Zhang, S., and Wenk, H.-R. Superplasticity in Earth's lower mantle: evidence from seismic anisotropy and rock physics. *Science*, 270(5235):458–461, 1995. doi: 10.1126/science.270.5235.458.

Karki, B.B., Wentzcovitch, R.M., De Gironcoli, S., and Baroni, S. High–pressure lattice dynamics and thermoelasticity of MgO. *Physical Review B*, 61(13):8793–8800, 2000. doi: 10.1103/PhysRevB.61.8793.

Kato, C.e, Hirose, K., Nomura, R., Ballmer, M.D., Miyake, A., and Ohishi, Y. Melting in the FeO–SiO_2 system to deep lower–mantle pressures: Implications for subducted Banded Iron Formations. *Earth and Planetary Science Letters*, 440:56–61, 2016. doi: 10.1016/j.epsl.2016.02.011.

Kaula, W.M. Elastic models of the mantle corresponding to variations in the external gravity field. *Journal of Geophysical Research*, 68(17):4967–4978, 1963. doi: 10.1029/JZ068i017p04967.

Keralavarma, S.M., Cagin, T., Arsenlis, A., and Benzerga, A.A. Power–law creep from discrete dislocation dynamics. *Physical Review Letters*, 109(26):265504, 2012. doi: 10.1103/PhysRevLett.109.265504.

King, S.D. Radial models of mantle viscosity: results from a genetic algorithm. *Geophysical Journal International*, 122(3):725–734, 1995. doi: 10.1111/j.1365-246X.1995.tb06831.x.

King, S.D. and Masters, G. An inversion for radial viscosity structure using seismic tomography. *Geophysical Research Letters*, 19(15):1551–1554, 1992. doi: 10.1029/92GL01700.

Knittle, E. and Jeanloz, R. High–pressure metallization of FeO and implications for the Earth's core. *Geophysical Research Letters*, 13(13):1541–1544, 1986. doi: 10.1029/GL013i013p01541.

Knittle, E. and Jeanloz, R. Earth's core–mantle boundary: results of experiments at high pressures and temperatures. *Science*, 251(5000):1438–1443, 1991. doi: 10.1126/science.251.5000.1438.

Kocks, U., Argon, A., Ashby, M., Chalmers, B., Christian, J., and Massalsk, T. *Progress in Material Science*. Pergamon, 1975.

Komabayashi, T. Thermodynamics of melting relations in the system Fe–FeO at high pressure: Implications for oxygen in the Earth's core. *Journal of Geophysical Research: Solid Earth*, 119(5):4164–4177, 2014. doi: 10.1002/2014JB010980.

Kraych, A., Carrez, P., and Cordier, P. On dislocation glide in $MgSiO_3$ bridgmanite at high–pressure and high–temperature. *Earth and Planetary Science Letters*, 452:60–68, 2016a. doi: 10.1016/j.epsl.2016.07.035.

Kraych, A., Carrez, P., Hirel, P., Clouet, E., and Cordier, P. Peierls potential and kink–pair mechanism in high–pressure $MgSiO_3$ perovskite: An atomic scale study. *Physical Review B*, 93(1):014103, 2016b. doi: 10.1103/PhysRevB.93.014103.

Kubin, L.P. *Dislocations, mesoscale simulations and plastic flow*, volume 5. Oxford University Press, 2013.

Kubin, L.P., Canova, G., Condat, M., Devincre, B., Pontikis, V., and Bréchet, Y. Dislocation microstructures and plastic flow: a 3D simulation. *Solid State Phenomena*, 23:455–472, 1992. doi: 10.4028/www.scientific.net/SSP.23-24.455.

Labrosse, S., Hernlund, J.W., and Coltice, N. A crystallizing dense magma ocean at the base of the Earth's mantle. *Nature*, 450(7171):866–869, 2007. doi: 10.1038/nature06355.

Langdon, T.G. and Pask, J.A. The mechanism of creep in polycrystalline magnesium oxide. *Acta Metallurgica*, 18(5):505–510, 1970. doi: 10.1016/0001-6160(70)90137-9.

Lawrence, J.F. and Wysession, M.E. Qlm9: A new radial quality factor (Q_μ) model for the lower mantle. *Earth and Planetary Science Letters*, 241(3):962–971, 2006. doi: 10.1016/j.epsl.2005.10.030.

Lay, T. Sharpness of the D'' discontinuity beneath the Cocos Plate: Implications for the perovskite to post–perovskite phase transition. *Geophysical Research Letters*, 35(3):L03304, 2008. doi: 10.1029/2007GL032465.

Li, L., Weidner, D.J., Chen, J., Vaughan, M.T., Davis, M., and Durham, W.B. X–ray strain analysis at high pressure: Effect of plastic deformation in MgO. *Journal of Applied Physics*, 95(12):8357–8365, 2004. doi: 10.1063/1.1738532.

Li, M., McNamara, A.K., Garnero, E.J., and Yu, S. Compositionally–distinct ultra–low velocity zones on Earth's core–mantle boundary. *Nature communications*, 8(1):177, 2017. doi: 10.1038/s41467-017-00219-x.

Li, P., Karato, S.-i., and Wang, Z. High–temperature creep in fine–grained polycrystalline $CaTiO_3$, an analogue material of $(Mg,Fe)SiO_3$ perovskite. *Physics of the Earth and Planetary Interiors*, 95(1-2):19–36, 1996. doi: 10.1016/0031-9201(95)03107-3.

Lin, J.-F., Wenk, H.-R., Voltolini, M., Speziale, S., Shu, J., and Duffy, T.S. Deformation of lower–mantle ferropericlase (Mg,Fe)O across the electronic spin transition. *Physics and Chemistry of Minerals*, 36(10):585, 2009. doi: 10.1007/s00269-009-0303-5.

Liu, J., Hu, Q., Kim, D.Y., Wu, Z., Wang, W., Xiao, Y., Chow, P., Meng, Y., Prakapenka, V.B., Mao, H.-K., and Mao, W.L. Hydrogen–bearing iron peroxide and the origin of ultralow–velocity zones. *Nature*, 551(7681):494–497, 2017. doi: 10.1038/nature24461.

Long, M.D. Complex anisotropy in D'' beneath the eastern Pacific from SKS–SKKS splitting discrepancies. *Earth and Planetary Science Letters*, 283(1):181–189, 2009. doi: 10.1016/j.epsl.2009.04.019.

Madec, R., Devincre, B., and Kubin, L.P. From dislocation junctions to forest hardening. *Physical Review Letters*, 89(25):255508, 2002. doi: 10.1103/PhysRevLett.89.255508.

Mainprice, D., Barruol, G., and IsmaïL, W.B. *The Seismic Anisotropy of the Earth's Mantle: from Single Crystal to Polycrystal*, pages 237–264. Wiley online library, 2000. doi: 10.1029/GM117p0237.

Mao, W.L., Shen, G., Prakapenka, V.B., Meng, Y., Campbell, A.J., Heinz, D.L., Shu, J., Hemley, R.J., and Mao, H.-k. Ferromagnesian postperovskite silicates in the D'' layer of the Earth. *Proceedings of the National Academy of Sciences of the United States of America*, 101(45):15867–15869, 2004a. doi: 10.1073/pnas.0407135101.

Mao, W.L., Sturhahn, W., Heinz, D.L., Mao, H.-K., Shu, J., and Hemley, R.J. Nuclear resonant X–ray scattering of iron hydride at high pressure. *Geophysical Research Letters*, 31(15):L15618, 2004b. doi: 10.1029/2004GL020541.

Marquardt, H. and Miyagi, L. Slab stagnation in the shallow lower mantle linked to an increase in mantle viscosity. *Nature Geoscience*, 8(4):311–314, 2015. doi: 10.1038/ngeo2393.

McKenzie, D.P. The viscosity of the lower mantle. *Journal of Geophysical Research*, 71 (16):3995–4010, 1966. doi: 10.1029/JZ071i016p03995.

McNamara, A.K., van Keken, P.E., and Karato, S.-i. Development of finite strain in the convecting lower mantle and its implications for seismic anisotropy. *Journal of Geophysical Research: Solid Earth*, 108(B5):2230, 2003. doi: 10.1029/2002JB001970.

McWilliams, R.S., Spaulding, D.K., Eggert, J.H., Celliers, P.M., Hicks, D.G., Smith, R.F., Collins, G.W., and Jeanloz, R. Phase Transformations and Metallization of Magnesium Oxide at High Pressure and Temperature. *Science*, 338(6112):1330–1333, 2012. doi: 10.1126/science.1229450.

Meade, C. and Jeanloz, R. The strength of mantle silicates at high pressures and room temperature: implications for the viscosity of the mantle. *Nature*, 348(6301):533–535, 1990. doi: 10.1038/348533a0.

Meade, C., Silver, P.G., and Kaneshima, S. Laboratory and seismological observations of lower mantle isotropy. *Geophysical Research Letters*, 22(10):1293–1296, 1995. doi: 10.1029/95GL01091.

Merkel, S., Wenk, H.R., Shu, J., Shen, G., Gillet, P., Mao, H.-K., and Hemley, R.J. Deformation of polycrystalline MgO at pressures of the lower mantle. *Journal of Geophysical Research: Solid Earth*, 107(B11):2271, 2002. doi: 10.1029/2001JB000920.

Merkel, S., Wenk, H.R., Badro, J., Montagnac, G., Gillet, P., Mao, H.-k., and Hemley, R.J. Deformation of ($Mg_{0.9}$,$fe_{0.1}$)SiO_3 perovskite aggregates up to 32 GPa. *Earth and Planetary Science Letters*, 209(3-4):351–360, 2003. doi: 10.1016/S0012-821X(03)00098-0.

Mitrovica, J.X. and Forte, A.M. A new inference of mantle viscosity based upon joint inversion of convection and glacial isostatic adjustment data. *Earth and Planetary Science Letters*, 225(1):177–189, 2004. doi: 10.1016/j.epsl.2004.06.005.

Miyagi, L. and Wenk, H.-R. Texture development and slip systems in bridgmanite and bridgmanite + ferropericlase aggregates. *Physics and Chemistry of Minerals*, 43(8): 597–613, 2016. doi: 10.1007/s00269-016-0820-y.

Miyajima, N., Yagi, T., and Ichihara, M. Dislocation microstructures of $MgSiO_3$ perovskite at a high pressure and temperature condition. *Physics of the Earth and Planetary Interiors*, 174(1):153–158, 2009. doi: 10.1016/j.pepi.2008.04.004.

Montagner, J.-P. and Kennett, B.L.N. How to reconcile body–wave and normal–mode reference Earth models. *Geophysical Journal International*, 125(1):229–248, 1996. doi: 10.1111/j.1365-246X.1996.tb06548.x.

Moresi, L., Zhong, S., Han, L., Conrad, C., Gurnis, M., Choi, E., Thoutireddy, P., Manea, V., McNamara, A., Becker, T., Leng, W., and Armendariz, L. Citcoms v3.3.1 [software], Computational Infrastructure for Geodynamics, 2014. URL `https://geodynamics.org/cig/software/citcoms/`.

Morra, G., Yuen, D.A., Boschi, L., Chatelain, P., Koumoutsakos, P., and Tackley, P.J. The fate of the slabs interacting with a density/viscosity hill in the mid–mantle. *Physics of the Earth and Planetary Interiors*, 180(3):271–282, 2010. doi: 10.1016/j.pepi.2010.04.001.

Muir, J.M.R. and Brodholt, J.P. Elastic properties of ferropericlase at lower mantle conditions and its relevance to ULVZs. *Earth and Planetary Science Letters*, 417:40–48, 2015. doi: 10.1016/j.epsl.2015.02.023.

Nabarro, F.R.N. Deformation of crystals by the motion of single ions. In *Report of a Conference on Strength of Solids*, pages 75–90. The Physical Soe, 1948.

Nabarro, F.R.N. Steady–state diffusional creep. *Philosophical Magazine*, 16(140):231–237, 1967. doi: 10.1080/14786436708229736.

Narayan, J. and Washburn, J. Self diffusion in magnesium oxide. *Acta Metallurgica*, 21 (5):533–538, 1973. doi: 10.1016/0001-6160(73)90060-6.

Nomura, R., Hirose, K., Uesugi, K., Ohishi, Y., Tsuchiyama, A., Miyake, A., and Ueno, Y. Low core–mantle boundary temperature inferred from the solidus of pyrolite. *Science*, 343(6170):522–525, 2014. doi: 10.1126/science.1248186.

Nzogang, B.C., Bouquerel, J., Cordier, P., Mussi, A., Girard, J., and Karato, S.i. Characterization by scanning precession electron diffraction of an aggregate of bridgmanite and ferropericlase deformed at hp-ht. *Geochemistry, Geophysics, Geosystems*, 19(3): 582–594, 2018. doi: 10.1002/2017GC007244.

Oishi, Y. and Kingery, W.D. Oxygen diffusion in periclase crystals. *The Journal of Chemical Physics*, 33(3):905–906, 1960. doi: 10.1063/1.1731286.

Oishi, Y., Ando, K., Kurokawa, H., and Hirsco, Y. Oxygen Self–Diffusion in MgO Single Crystals. *Journal of the American Ceramic Society*, 66(4):C-60–C-62, 1983. doi: 10.1111/j.1151-2916.1983.tb15695.x.

Orowan, E. Mechanical strength properties and real structure of crystals. *Zeitschrift für Kristallographie*, 89(3/4):327–343, 1934.

Orowan, E. Convection in a non–Newtonian mantle, continental drift, and mountain building. *Philosophical Transactions for the Royal Society of London A*, 258(1088): 284–313, 1965.

Ozawa, H., Hirose, K., Ohta, K., Ishii, H., Hiraoka, N., Ohishi, Y., and Seto, Y. Spin crossover, structural change, and metallization in NiAs–type FeO at high pressure. *Physical Review B*, 84:134417, 2011. doi: 10.1103/PhysRevB.84.134417.

Phillips, B.R., Bunge, H.-P., and Schaber, K. True polar wander in mantle convection models with multiple, mobile continents. *Gondwana Research*, 15(3):288–296, 2009. doi: 10.1016/j.gr.2008.11.007.

Poirier, J.-P. *Creep of crystals: high–temperature deformation processes in metals, ceramics and minerals.* Cambridge University Press, 1985.

Polanyi, M. Lattice distortion which originates plastic flow. *Zeitschrift für Kristallographie*, 89(9/10):660–662, 1934.

Pradhan, G.K., Fiquet, G., Siebert, J., Auzende, A.-L., Morard, G., Antonangeli, D., and Garbarino, G. Melting of MORB at core–mantle boundary. *Earth and Planetary Science Letters*, 431:247–255, 2015. doi: 10.1016/j.epsl.2015.09.034.

Ramesh, K.S., Yasuda, E., and Kimura, S. Negative creep and recovery during high–temperature creep of mgo single crystals at low stresses. *Journal of materials science*, 21(9):3147–3152, 1986. doi: 10.1007/BF00553350.

Reali, R., Boioli, F., Gouriet, K., Carrez, P., Devincre, B., and Cordier, P. Modeling plasticity of MgO by 2.5D dislocation dynamics simulations. *Materials Science and Engineering: A*, 690:52–61, 2017. doi: 10.1016/j.msea.2017.02.092.

Reaman, D.M., Colijn, H.O., Yang, F., Hauser, A.J., and Panero, W.R. Interdiffusion of Earth's core materials to 65 GPa and 2200 K. *Earth and Planetary Science Letters*, 349:8–14, 2012. doi: 10.1016/j.epsl.2012.06.053.

Revenaugh, J. and Meyer, R. Seismic evidence of partial melt within a possibly ubiquitous low–velocity layer at the base of the mantle. *Science*, 277(5326):670–673, 1997. doi: 10.1126/science.277.5326.670.

Ricard, Y. and Wuming, B. Inferring the viscosity and the 3–D density structure of the mantle from geoid, topography and plate velocities. *Geophysical Journal International*, 105(3):561–571, 1991. doi: 10.1111/j.1365-246X.1991.tb00796.x.

Ricard, Y., Richards, M., Lithgow-Bertelloni, C., and Le Stunff, Y. A geodynamic model of mantle density heterogeneity. *Journal of Geophysical Research: Solid Earth*, 98(B12): 21895–21909, 1993. doi: 10.1029/93JB02216.

Ringwood, A.E. The chemical composition and origin of the Earth. In *Advances in earth science*, volume 65, page 287, 1966.

Ringwood, A.E. *Composition and Petrology of the Earth's Mantle.* MacGraw–Hill, 1975.

Ritterbex, S.A.W., Carrez, P., Gouriet, K., and Cordier, P. Modeling dislocation glide in Mg_2SiO_4 ringwoodite: Towards rheology under transition zone conditions. *Physics of the Earth and Planetary Interiors*, 248:20–29, 2015. doi: 10.1016/j.pepi.2015.09.001.

Rost, S. Deep Earth: core–mantle boundary landscapes. *Nature Geoscience*, 6(2):89–90, 2013. doi: 10.1038/ngeo1715.

Rost, S., Garnero, E.J., and Williams, Q. Fine–scale ultralow–velocity zone structure from high–frequency seismic array data. *Journal of Geophysical Research: Solid Earth*, 111(B9):B09310, 2006. doi: 10.1029/2005JB004088.

Rothwell, W.S. and Neiman, A.S. Creep in vacuum of MgO single crystals and the electric field effect. *Journal of Applied Physics*, 36(7):2309–2316, 1965. doi: 10.1063/1.1714469.

Routbort, J.L. Work hardening and creep of MgO. *Acta Metallurgica*, 27(4):649–661, 1979. doi: 10.1016/0001-6160(79)90016-6.

Rozel, A., Ricard, Y., and Bercovici, D. A thermodynamically self–consistent damage equation for grain size evolution during dynamic recrystallization. *Geophysical Journal International*, 184(2):719–728, 2011. doi: 10.1111/j.1365-246X.2010.04875.x.

Rudolph, M.L., Lekić, V., and Lithgow-Bertelloni, C. Viscosity jump in Earth's mid–mantle. *Science*, 350(6266):1349–1352, 2015. doi: 10.1126/science.aad1929.

Sabadini, R. and Yuen, D.A. Mantle stratification and long–term polar wander. *Nature*, 339(6223):373–375, 1989. doi: 10.1038/339373a0.

Sakaguchi, I., Yurimoto, H., and Sueno, S. Self–diffusion along dislocations in single–crystals MgO. *Solid state communications*, 84(9):889–893, 1992. doi: 10.1016/0038-1098(92)90453-G.

Sakai, T., Ohtani, E., Terasaki, H., Miyahara, M., Nishijima, M., Hirao, N., Ohishi, Y., and Sata, N. Fe–Mg partitioning between post–perovskite and ferropericlase in the lowermost mantle. *Physics and Chemistry of Minerals*, 37(7):487–496, 2010. doi: 10.1007/s00269-009-0349-4.

Sato, F. and Sumino, K. The yield strength and dynamic behaviour of dislocations in MgO crystals at high temperatures. *Journal of Materials Science*, 15(7):1625–1634, 1980. doi: 10.1007/BF00550578.

Shim, S.-H., Grocholski, B., Ye, Y., Alp, E.E., Xu, S., Morgan, D., Meng, Y., and Prakapenka, V.B. Stability of ferrous–iron–rich bridgmanite under reducing midmantle conditions. *Proceedings of the National Academy of Sciences*, 114(25):6468–6473, 2017. doi: 10.1073/pnas.1614036114.

Shin, C.-S., Fivel, M.C., Verdier, M., and Kwon, S.C. Numerical methods to improve the computing efficiency of discrete dislocation dynamics simulations. *Journal of Computational Physics*, 215(2):417–429, 2006. doi: 10.1016/j.jcp.2005.10.025.

Shirasaki, S. and Hama, M. Oxygen–diffusion characteristics of loosely–sintered polycrystalline MgO. *Chemical Physics Letters*, 20(4):361–365, 1973. doi: 10.1016/0009-2614(73)80066-1.

Singh, R.P., Singh, M.P., and Singh, R.K. Acoustical dissipation due to phonon–phonon interaction, thermoelastic loss and dislocation damping in MnO and CoO. In *Proceedings of Meetings on Acoustics 155*, volume 4, page 045006. ASA, 2008. doi: 10.1121/1.2991172.

Solomatova, N.V., Jackson, J.M., Sturhahn, W., Wicks, J.K., Zhao, J., Toellner, T.S., Kalkan, B., and Steinhardt, W.M. Equation of state and spin crossover of (Mg,Fe)O at high pressure, with implications for explaining topographic relief at the core–mantle boundary. *American Mineralogist*, 101(5):1084–1093, 2016. doi: 10.2138/am-2016-5510.

Speziale, S., Milner, A., Lee, V.E., Clark, S.M., Pasternak, M.P., and Jeanloz, R. Iron spin transition in Earth's mantle. *Proceedings of the National Academy of Sciences of the United States of America*, 102(50):17918–17922, 2005. doi: 10.1073/pnas.0508919102.

Srinivasan, M. and Stoebe, T.G. Temperature dependence of yielding and work–hardening rates in magnesium oxide single crystals. *Journal of Materials Science*, 9(1):121–128, 1974. doi: 10.1007/BF00554762.

Stacey, F.D. and Davis, P.M. High pressure equations of state with applications to the lower mantle and core. *Physics of the Earth and Planetary Interiors*, 142(3-4):137–184, 2004. doi: 10.1016/j.pepi.2004.02.003.

Steinberger, B. and Calderwood, A.R. Models of large–scale viscous flow in the Earth's mantle with constraints from mineral physics and surface observations. *Geophysical Journal International*, 167(3):1461–1481, 2006. doi: 10.1111/j.1365-246X.2006.03131.x.

Steinberger, B.M. and Calderwood, A.R. Mineral physics constraints on viscous flow models of mantle flow. In *J. Conf. Abs*, volume 6, pages 423–424, 2001.

Sturhahn, W., Jackson, J.M., and Lin, J.-F. The spin state of iron in minerals of Earth's lower mantle. *Geophysical Research Letters*, 32(12):L12307, 2005. doi: 10.1029/2005GL022802.

Sun, D. and Helmberger, D. Lower mantle tomography and phase change mapping. *Journal of Geophysical Research: Solid Earth*, 113(B10):B10305, 2008. doi: 10.1029/2007JB005289.

Sun, D., Helmberger, D.V., Jackson, J.M., Clayton, R.W., and Bower, D.J. Rolling hills on the core–mantle boundary. *Earth and Planetary Science Letters*, 361:333–342, 2013. doi: 10.1016/j.epsl.2012.10.027.

Tackley, P.J. On the ability of phase transitions and viscosity layering to induce long wavelength heterogeneity in the mantle. *Geophysical Research Letters*, 23(15):1985–1988, 1996. doi: 10.1029/96GL01980.

Tange, Y., Kuwayama, Y., Irifune, T., Funakoshi, K.-i., and Ohishi, Y. P–V–T equation of state of $MgSiO_3$ perovskite based on the MgO pressure scale: A comprehensive reference for mineralogy of the lower mantle. *Journal of Geophysical Research: Solid Earth*, 117(B6):B06201, 2012. doi: 10.1029/2011JB008988.

Tateno, S., Hirose, K., and Ohishi, Y. Melting experiments on peridotite to lowermost mantle conditions. *Journal of Geophysical Research: Solid Earth*, 119(6):4684–4694, 2014. doi: 10.1002/2013JB010616.

Taylor, G.I. The mechanism of plastic deformation of crystals. Part I–Theoretical. *Proceedings of the Royal Society of London A: Mathematical, Physical and Engineering Sciences*, 145(855):362–387, 1934. doi: 10.1098/rspa.1934.0106.

Thomas, C., E.J., Garnero, and Lay, T. High–resolution imaging of lowermost mantle structure under the Cocos plate. *Journal of Geophysical Research: Solid Earth*, 109 (B8):B08037, 2004. doi: 10.1029/2004JB003013.

Thorne, M.S, Garnero, E.J., Jahnke, G., Igel, H., and McNamara, A.K. Mega ultra low velocity zone and mantle flow. *Earth and Planetary Science Letters*, 364:59–67, 2013. doi: 10.1016/j.epsl.2012.12.034.

Tomioka, N. and Fujino, K. Natural (Mg,Fe)SiO_3-Ilmenite and -Perovskite in the Tenham Meteorite. *Science*, 277(5329):1084–1086, 1997. doi: 10.1126/science.277.5329.1084.

Tschauner, O., Ma, C., Beckett, J.R., Prescher, C., Prakapenka, V.B., and Rossman, G.R. Discovery of bridgmanite, the most abundant mineral in Earth, in a shocked meteorite. *Science*, 346(6213):1100–1102, 2014. doi: 10.1126/science.1259369.

Tsuchiya, T., Wentzcovitch, R.M., da Silva, C.R.S., and de Gironcoli, S. Spin Transition in Magnesiowüstite in Earth's Lower Mantle. *Physical Review Letters*, 96:198501, 2006. doi: 10.1103/PhysRevLett.96.198501.

Tsujino, N., Nishihara, Y., Yamazaki, D., Seto, Y., Higo, Y., and Takahashi, E. Mantle dynamics inferred from the crystallographic preferred orientation of bridgmanite. *Nature*, 539(7627):81–84, 2016. doi: 10.1038/nature19777.

Van Orman, J.A. and Crispin, K.L. Diffusion in oxides. *Reviews in Mineralogy and Geochemistry*, 72(1):757–825, 2010. doi: 10.2109/jcersj1950.74.851_215.

Van Orman, J.A., Fei, Y., Hauri, E.H., and Wang, J. Diffusion in MgO at high pressures: Constraints on deformation mechanisms and chemical transport at the core–mantle boundary. *Geophysical Research Letters*, 30(2):28–1–28–4, 2003. doi: 10.1029/2002GL016343.

Vidale, J.E. and Benz, H.M. A sharp and flat section of the core–mantle boundary. *Nature*, 359(6396):627–629, 1992. doi: 10.1038/359627a0.

Volterra, V. Sur l'équilibre des corps élastiques multiplement connexes. In *Annales scientifiques de l'École normale supérieure*, volume 24, pages 401–517, 1907.

Wang, Z., Karato, S.-i., and Fujino, K. High temperature creep of single crystal strontium titanate ($SrTiO_3$): a contribution to creep systematics in perovskites. *Physics of the earth and planetary interiors*, 79(3-4):299–312, 1993. doi: 10.1016/0031-9201(93)90111-L.

Watson, G.W., Wall, A., and Parker, S.C. Atomistic simulation of the effect of temperature and pressure on point defect formation in $MgSiO_3$ perovskite and the stability of $CaSiO_3$ perovskite. *Journal of Physics: Condensed Matter*, 12(39):8427, 2000. doi: 10.1088/0953-8984/12/39/306/.

Weertman, J. Theory of steady–state creep based on dislocation climb. *Journal of Applied Physics*, 26(10):1213–1217, 1955. doi: 10.1063/1.1721875.

Weertman, J. Dislocation climb theory of steady–state creep. *Trans. Amer. Soc. Metal.*, 61:681–694, 1968.

Wenk, H.-R., Lonardeli, I., Pehl, J., Devine, J., Prakapenka, V., Shen, G., and Mao, H.-K. In situ observation of texture development in olivine, ringwoodite, magnesiowüstite and silicate perovskite at high pressure. *Earth and Planetary Science Letters*, 226(3): 507–519, 2004. doi: 10.1016/j.epsl.2004.07.033.

Wentzcovitch, R.M., Karki, B.B., Cococcioni, M., and De Gironcoli, S. Thermoelastic Properties of $MgSiO_3$–Perovskite: Insights on the Nature of the Earth's Lower Mantle. *Physical Review Letters*, 92(1):018501, 2004. doi: 10.1103/PhysRevLett.92.018501.

Wicks, J.K., Jackson, J.M., and Sturhahn, W. Very low sound velocities in iron–rich (Mg,Fe)O: Implications for the core–mantle boundary region. *Geophysical Research Letters*, 37(15):L15304, 2010. doi: 10.1029/2010GL043689.

Wicks, J.K., Jackson, J.M., Sturhahn, W., Zhuravlev, K.K., Tkachev, S.N., and Prakapenka, V.B. Thermal equation of state and stability of $(Mg_{0.06}Fe_{0.94})O$. *Physics of the Earth and Planetary Interiors*, 249:28–42, 2015. doi: 10.1016/j.pepi.2015.09.003.

Wicks, J.K., Jackson, J.M., Sturhahn, W., and Zhang, D. Sound velocity and density of magnesiowüstites: Implications for ultralow–velocity zone topography. *Geophysical Research Letters*, 44(5):2148–2158, 2017. doi: 10.1002/2016GL071225.

Williams, Q. and Garnero, E.J. Seismic evidence for partial melt at the base of Earth's mantle. *Science*, 273(5281):1528–1530, 1996. doi: 10.1126/science.273.5281.1528.

Wolfenstine, J. and Kohlstedt, D.L. Creep of (Mg,Fe)O single crystals. *Journal of materials science*, 23(10):3550–3557, 1988. doi: 10.1007/BF00540494.

Wood, B.J. Phase transformations and partitioning relations in peridotite under lower mantle conditions. *Earth and Planetary Science Letters*, 174(3):341–354, 2000. doi: 10.1016/S0012-821X(99)00273-3.

Wright, K., Price, G.D., and Poirier, J.P. High–temperature creep of the perovskites $CaTiO_3$ and $NaNbO_3$. *Physics of the earth and planetary interiors*, 74(1-2):9–22, 1992. doi: 10.1016/0031-9201(92)90064-3.

Wu, P., Eriksson, G., and Pelton, A.D. Critical evaluation and optimization of the thermodynamic properties and phase diagrams of the CaO–FeO, CaO–MgO, CaO–MnO, FeO–MgO, FeO–MnO, and MgO–MnO systems. *Journal of the American Ceramic Society*, 76(8):2065–2075, 1993. doi: 10.1111/j.1151-2916.1993.tb08334.x.

Wu, Z. and Wentzcovitch, R.M. Spin crossover in ferropericlase and velocity heterogeneities in the lower mantle. *Proceedings of the National Academy of Sciences*, 111 (29):10468–10472, 2014. doi: 10.1073/pnas.1322427111.

Xu, J., Yamazaki, D., Katsura, T., Wu, X., Remmert, P., Yurimoto, H., and Chakraborty, S. Silicon and magnesium diffusion in a single crystal of $MgSiO_3$ perovskite. *Journal of Geophysical Research: Solid Earth*, 116(B12):B12205, 2011. doi: 10.1029/2011JB008444.

Yamaguchi, S. and Someno, M. The Tracer Diffusivity of Oxygen in Wüstite and Cobaltous Oxide. *Transactions of the Japan Institute of Metals*, 23(5):259–266, 1982. doi: 10.2320/matertrans1960.23.259.

Yamazaki, D. and Karato, S.-i. Some mineral physics constraints on the rheology and geothermal structure of Earth's lower mantle. *American Mineralogist*, 86(4):385–391, 2001. doi: 10.2138/am-2001-0401.

Yamazaki, D. and Karato, S.-i. Fabric development in (Mg,Fe)O during large strain, shear deformation: implications for seismic anisotropy in Earth's lower mantle. *Physics of the Earth and Planetary Interiors*, 131(3):251–267, 2002. doi: 10.1016/S0031-9201(02)00037-7.

Yamazaki, D., Kato, T., Yurimoto, H., Ohtani, E., and Toriumi, M. Silicon self–diffusion in $MgSiO_3$ perovskite at 25 GPa. *Physics of the Earth and Planetary Interiors*, 119(3-4):299–309, 2000. doi: 10.1016/S0031-9201(00)00135-7.

Yang, M.H. and Flynn, C.P. Intrinsic diffusion properties of an oxide: MgO. *Physical Review Letters*, 73(13):1809, 1994. doi: 10.1103/PhysRevLett.73.1809.

Yang, M.H. and Flynn, C.P. Ca^{2+} and $^{18}O^{2-}$ diffusion in ultrapure MgO. *Journal of Physics: Condensed Matter*, 8(18):L279–L283, 1996. doi: 10.1088/0953-8984/8/18/001.

Yavari, P., Miller, D.A., and Langdon, T.G. An investigation of Harper–Dorn creep – I. Mechanical and microstructural characteristics. *Acta Metallurgica*, 30(4):871–879, 1982. doi: 10.1016/0001-6160(82)90085-2.

Yoo, H.-I., Wuensch, B.J., and Petuskey, W.T. Oxygen self–diffusion in single–crystal MgO: secondary–ion mass spectrometric analysis with comparison of results from gas–solid and solid–solid exchange. *Solid state ionics*, 150(3–4):207–221, 2002. doi: 10.1016/S0167-2738(02)00537-4.

Yu, S. and Garnero, E.J. Ultralow velocity zone locations: A global assessment. *Geochemistry, Geophysics, Geosystems*, 19(2):396–414, 2018. doi: 10.1002/2017GC007281.

Zerr, A. and Boehler, R. Constraints on the melting temperature of the lower mantle from high–pressure experiments on MgO and magnesiowüstite. *Nature*, 371(6497):506–508, 1994. doi: 10.1038/371506a0.

Zhang, B., Ni, S., Sun, D., Shen, Z., Jackson, J.M., and Wu, W. Constraints on small–scale heterogeneity in the lowermost mantle from observations of near podal PcP precursors. *Earth and Planetary Science Letters*, 489:267–276, 2018. doi: 10.1016/j.epsl.2018.01.033.

Zhang, D., Jackson, J.M., Zhao, J., Sturhahn, W., Alp, E.E., Hu, M.Y., Toellner, T.S., Murphy, C.A., and Prakapenka, V.B. Temperature of Earth's core constrained from melting of Fe and $Fe_{0.9}Ni_{0.1}$ at high pressures. *Earth and Planetary Science Letters*, 447:72–83, 2016. doi: 10.1016/j.epsl.2016.04.026.

Zhang, L. and Fei, Y. Melting behavior of (Mg,Fe)O solid solutions at high pressure. *Geophysical Research Letters*, 35(13):L13302, 2008. doi: 10.1029/2008GL034585.

A connecting principle
linked to the invisible.
Almost imperceptible
something inexpressible.
Science insusceptible
logic so inflexible.
Causally connectible
yet nothing is invincible.

The Police, Synchronicity

Curses, curses and clues
A feast, a feast for fools

The Black Crowes, Descending

If there's pensive fear,
a wasted year
a man must learn to cope.
If his obsession's real,
suppression that he feels
must turn to hope.
Life is no more assuring than love,
it's time to take the time.
There are no answers from voices above,
it's time to take the time.
You're fighting the weight of the world,
and no one can save you this time.
Close your eyes,
you can find all you need in your mind

Dream Theater, Take the time

And I'm not the kind that likes to tell you
just what you want me to.
You're not the kind that needs to tell me
about the birds and the bees.

New Order, Age of consent

Certo son stato cattivo,
chiedo scusa ho sbagliato
la mancanza di rispetto
dovrebbe essere un reato.
Come anche l'idiozia
e questa malinconia
che mi sale dentro al cuore
quando entro a casa mia.
Non generalizzare
e nemmeno devi urlare
che non è comunicare
ed è pure antisociale.
Guccini lo sa bene:
non ho voglia di far niente
e anche se mai mi venisse
a fermarmi c'è la gente.
Il mio voto vale quanto
quello di quest'imbecille
e allora cosa me ne frega
delle vostre 5 stelle
e di tutte le parole
che vi sento blaterare
sopra il bene comune,
l'amore universale.

Non provo vergogna
se mi date del pezzente
certo io non ho il cash
ma di essere attraente
circondato da idioti
non me ne frega niente.

Di cosa ridete? E di cosa urlate?
Perché festeggiate ancora l'estate?
Di cosa ballate? Di cosa vi fate?
Tutti viva qualcosa
Sempre viva qualcosa.

The Zen Circus, Viva